Technical Report Documentation Page

1. Report No.	2. Government Accession No.	3. Recipient's Catalog No.
FHWA/TX-05/0-1700-6		

4. Title and Subtitle	5. Report Date
MOISTURE-RELATED CRACKING EFFECTS ON HYDRATING CONCRETE PAVEMENT	September 2006 Published: October 2006
	6. Performing Organization Code
7. Author(s)	8. Performing Organization Report No.
Anal K. Mukhopadhyay, Dan Ye, and Dan G. Zollinger	Report 0-1700-6
9. Performing Organization Name and Address	10. Work Unit No. (TRAIS)
Texas Transportation Institute The Texas A&M University System College Station, Texas 77843-3135	11. Contract or Grant No. Project 0-1700
12. Sponsoring Agency Name and Address	13. Type of Report and Period Covered
Texas Department of Transportation Research and Technology Implementation Office P. O. Box 5080 Austin, Texas 78763-5080	Technical Report: September 2000-March 2004
	14. Sponsoring Agency Code

15. Supplementary Notes

Project performed in cooperation with the Texas Department of Transportation and the Federal Highway Administration.
Project Title: Improving Portland Cement Concrete Pavement Performance
URL:http://tti.tamu.edu/documents/0-1700-6.pdf

16. Abstract

Hydrating concrete pavement is typically subjected to both moisture and temperature-induced stresses that drive cracking mechanisms at early concrete ages. Undesirable cracking resulting from these mechanisms plays a key role in both short- and long-term performance of most concrete pavement systems. Short-term performance is heavily dependent upon curing quality and construction weather while curling and warping behavior can have both short- and long-term consequences. The focus of this report is primarily on the short-term perspective and how moisture profile and curing quality effects are involved in warping behavior and ultimately delamination cracking and spalling distress.

Based on this perspective, mathematical models were developed for the calculation of moisture and temperature profiles to help investigate the effect of different combinations of climate, construction, and materials on the development of the moisture and temperature profiles and their subsequent effects on early-aged cracking. These models appear as nonlinear time-dependent partial differential equations and are solved by the finite element method simultaneously that involves both backward and forward calculation. Using measured test data, moisture diffusivity and thermal conductivity were back-calculated to facilitate accurate modeling of moisture and temperature flows in hardening concrete. On the whole, the calculated moisture and temperature profiles using the moisture diffusivity and thermal conductivity models corresponded to the measured data.

Spalling typically occurs at random cracks and occasionally at joints subjected to high delamination stresses during and shortly after construction. The incidence of this distress type is strongly correlated to pre-existing horizontal delaminations that occur within 25 mm of the pavement surface and can later grow into a spall due to a variety of causes. The cause of the shallow, horizontal delaminations that occur within the top 25 mm of the pavement surface is primarily from early-age nonlinear shrinkage strains in addition to temperature variations through slab depth. Thus, the factors of the most importance are those related to the effectiveness of the curing medium in minimizing moisture loss during the hydration of the concrete and the bond strength between the aggregate and the paste. By increasing the effectiveness of the curing system, moisture gradients near the surface are substantially reduced and delamination stress minimized.

17. Key Words	18. Distribution Statement
Coefficient of Thermal Expansion, Concrete, Aggregate, Bond Strength, Thermal Expansion, Mineral, Dilatometer, Aggregate Gradation	No Restrictions. This document is available to the public through NTIS: National Technical Information Service Springfield, Virginia 22161 http://www.ntis.gov

19. Security Classif.(of this report)	20. Security Classif.(of this page)	21. No. of Pages	22. Price
Unclassified	Unclassified	172	

Form DOT F 1700.7 (8-72) **Reproduction of completed page authorized**

MOISTURE-RELATED CRACKING EFFECTS ON HYDRATING CONCRETE PAVEMENT

by

Anal K. Mukhopadhyay
Associate Research Scientist
Texas Transportation Institute

Dan Ye
Graduate Assistant Research
Texas Transportation Institute

and

Dan G. Zollinger
Associate Research Engineer
Texas Transportation Institute

Report 0-1700-6
Project 0-1700
Project Title: Improving Portland Cement Concrete Pavement Performance

Performed in cooperation with the
Texas Department of Transportation
and the
Federal Highway Administration

September 2006
Published: October 2006

TEXAS TRANSPORTATION INSTITUTE
The Texas A&M University System
College Station, Texas 77843-3135

DISCLAIMER

The contents of this report reflect the views of the authors, who are responsible for the facts and the accuracy of the data presented herein. The contents do not necessarily reflect the official view or policies of the Texas Department of Transportation and/or the Federal Highway Administration. This report does not constitute a standard, specification, or regulation. The engineer in charge of the project was Dan G. Zollinger, Texas P.E. #67129.

ACKNOWLEDGMENTS

The authors wish to express their appreciation to the Texas Department of Transportation personnel for their support throughout this project, as well as the project director Mr. David Head and the members of the project monitoring committee.

TABLE OF CONTENTS

Page

TABLE OF CONTENTS

Page

LIST OF FIGURES

Figure **Page**

LIST OF FIGURES (Continued)

LIST OF FIGURES (Continued)

Figure **Page**

LIST OF FIGURES (Continued)

Figure **Page**

LIST OF FIGURES (Continued)

Figure **Page**

LIST OF FIGURES (Continued)

Figure **Page**

LIST OF TABLES

Table **Page**

CHAPTER 1

ROLE OF MOISTURE IN HYDRATING CONCRETE

INTRODUCTION

The nature of moisture and its vertical distribution in concrete while it is hardening particularly near the evaporative surface has become the subject of great interest due to its apparent long-term impact on pavement performance. Previous research has shown that an understanding of the distribution and history of moisture at an early age is important when assessing the effect of the quality of curing on concrete behavior. Its prediction, elaborated in Chapter 2, is an inevitable task that must be achieved for a realistic estimation of drying shrinkage, thermal expansion, strength, maturity, and curing efficiency. Although some experimental data have been assembled over many years of research, little data at early ages of drying concrete are presently available.

Moisture in concrete materials is comprised of two parts: one referred to as structural or water chemically bound within the cement paste hydration products (w_n) and the other as water contained within the pore structure of the calcium silicate hydrate (CSH) (w_g) hydration product. The sum of these portions equals the total water content (w) in the paste. One aspect of the effect of moisture in concrete pavement can be reflected in drying shrinkage and creep behavior. These behavioral characteristics are of concern with respect to early-age concrete slab deflections and formation of early-aged cracks or development of delamination in bonded concrete overlay systems. Material-related moisture properties (permeability, diffusivity, slope of the moisture isotherm, etc.) of concrete play a key role in the mathematical modeling and representation of stress and strain due to drying shrinkage and creep under varying humidity conditions. Material tests are necessary to determine these pertinent material properties. Moisture flow models that represent the variation of moisture with time use these properties. In terms of engineering applications, prediction of humidity and water diffusion is very important in consideration of spalling, warping, and other moisture-related stresses, strains, and deformations induced in concrete pavements.

Hardening concrete in the early stages may not have sufficient tensile strength to resist tensile stress caused by volumetric contraction at its surface due to evaporation. Thus, cracking may develop at the surface of the pavement because of water loss due to evaporation. Uno (1998) indicated factors influencing shrinkage cracking:

- Concrete strength (related to the total cement or binder content)
- Slab thickness (related to the bleeding capacity)
- Fines content (related to water demand)
- Admixtures (primarily retarders)
- Subbase preparation (primarily subbase membranes)
- Surface sprays (primarily aliphatic alcohols)

Early-aged warping behavior is the main concern, and it is the probable cause of relatively high shear stresses that cause delamination in the vicinity of the slab corner or along slab edges. These delaminations are typically shallow and often develop into spalls (Figure 1-1).

Figure 1-1 Spalled Joint.

Spalling refers to the breakdown or dislodging of concrete segments along a joint or crack in a concrete slab within 0.6 m (2 ft) of a joint or crack (Wang and Zollinger, 2000) that can affect the structural slab integrity (Figure 1-2). Horizontal shear stresses primarily develop from large moisture gradients causing a shearing action due to the gradient effect. The development of the gradient is due to evaporation as a function of the ambient temperature and curing conditions during and after placement of the concrete (Figure 1-2). Typically, the delamination is relatively shallow and occurs at an early concrete age when stresses caused by the moisture variation surpass the concrete shear strength. Significant spalling is unlikely to occur where the delaminations are not formed or are greater than 3 inches deep. In the event that they are formed, their extension into spalling appears to be by fatigue due

to wheel loads and to some extent temperature fluctuations. Equations for delamination stress are presented later in this document.

Conditions necessary for formation of the delaminations include low interfacial strength between the coarse aggregate and mortar and sufficient evaporation of pore water from the hydrating concrete resulting in differential drying shrinkage near the pavement surface. Temperature variation may be a factor in the development of the delamination shear fracture, but it is presumed not to be as large as the shrinkage contribution. Once delaminations have formed, they may extend later into spalls as a result of incompressibles, freeze-thaw cycles, traffic loading, and other effects of this sort.

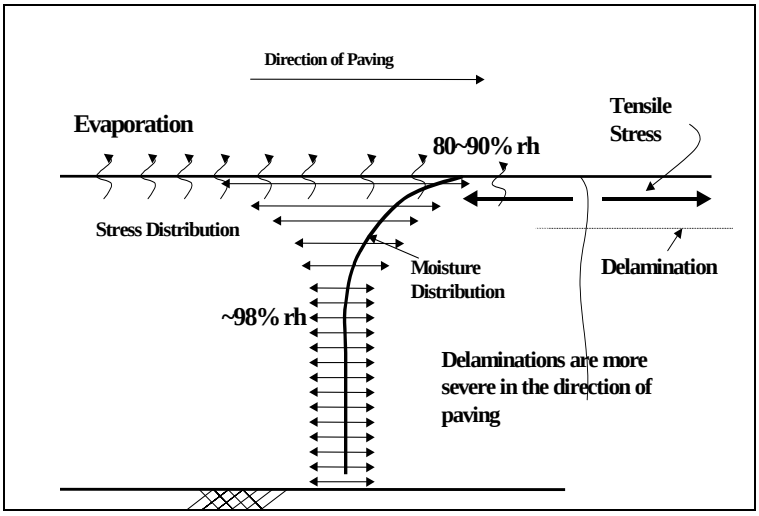

Figure 1-2 Formation of Horizontal Delamination (Wang and Zollinger, 2000).

As background to comprehending the effect of moisture in concrete curing quality relative to the development of spalling and related concrete behavior, key aspects of the part that moisture plays in concrete are elaborated in this chapter. Those aspects are hydration, porosity, drying shrinkage, and moisture effects on the thermal expansion characteristics of concrete.

THE ROLE OF WATER IN CEMENT HYDRATION

The setting and hardening of cement are the result of chemical and physical reactions that take place between cement and water (H), that is, hydration. The chemical reactions describing the hydration of cement are complex. Consequently, a simplification is to study the hydration of individual compounds separately. This, however, assumes that each compound hydrates independent of the others that are present in Portland cement. This assumption is not fully valid, because interactions between hydrating compounds can

have important consequences. However, for the silicate phases, it is at least a reasonable approximation.

Hydration of Calcium Silicates

The hydration reactions of the two calcium silicates (C_3S and C_2S) are stoichiometrically very similar, differing only in the amount of calcium hydroxide formed. The measured heats of hydration are also considerably different:

$$2C_3S + 7H > C_3S_2H_4\ (CSH) + 3CH \quad -114\ KJ/mole$$

$$2C_2S + 5H > C_3S_2H_4 + CH \quad -34\ KJ/mole$$

The principal hydration product is a CSH. The formula $C_3S_2H_4$ is only an approximate one. CSH is a poorly crystalline material, which forms extremely small particles in the size range of colloidal matter (< 1 urn). In contrast, CH is a crystalline product with a fixed composition. The reaction sequence of C_3S is best described by the calorimetric curve shown in Figure 1-3, which measures the rate of heat evolution as a function of time. The heat flow from the sample is proportional to the rate of reaction, and it is easily measurable in the case of C_3S. To be noted is the fact that C_3S is the compound of major interest, since it comprises 40 to 70 percent by weight of cement.

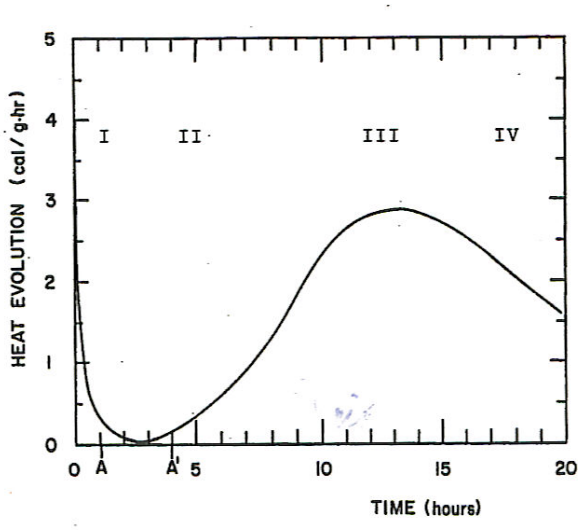

Figure 1-3 Depiction of C_3S Hydration.

When first mixed with water, a period of rapid heat evolution occurs (Stage I), which ceases within about 15 minutes. This is followed by a period of relative inactivity, the induction or dormant period (Stage II), which explains why Portland cement concrete remains in the plastic state for some time. Initial set occurs in 1 to 3 hours, about the time C_3S has begun to react again with renewed vigor at the end of the dormant period. The silicate continues to hydrate rapidly, reaching a maximum at the end of the acceleration period (Stage III), which corresponds to the maximum rate of heat evolution. By this time (2 to 8 hours), final set has occurred and

early hardening has begun. Thereafter, the rate of reaction again slows down (Stage IV) until it reaches a steady rate within 12 to 24 hours.

On first contact with water, Ca and OH ions are rapidly released from the surface of C_3S grains; the pH rises to over 12 within a few minutes, which indicates a very alkaline solution. This hydrolysis slows down quickly, but continues throughout the induction period. When the Ca and OH ions reach a critical value, CH starts to crystallize from the solution with the concomitant formation of CSH, and the reaction of C_3S again proceeds rapidly. The induction period is caused by the need to achieve a certain concentration in solution. As CH crystallizes from solution, CSH develops at the surface of C_3S, and it forms a coating covering the grain. As hydration continues, the thickness of this hydrate layer increases to form a barrier through which water must flow to reach the unhydrated C_3S, and through which ions must diffuse to reach the growing crystals. Eventually, the movement through the CSH layer determines the rate of reaction. At this stage, hydration also becomes diffusion-controlled. Such reactions are quite slow, and they become slower as the thickness of the diffusion barrier increases. C_2S hydrates in a similar manner, but much more slowly, because it is a less reactive compound than C_3S. Additionally, the heat of hydration of C_2S is less than C_3S.

Hydration, like other chemical reactions, is sensitive to temperature. The rate of reaction increases with temperature, but hydration is more sensitive to temperature through Stage III when the reaction is chemically controlled. Once hydration becomes completely diffusion-controlled in Stage IV and beyond, it is much less temperature-sensitive.

Hydration of Tricalcium Aluminate

The primary reaction of C_3A with water in the presence of a plentiful supply of gypsum is:

$$C_3A + 3\ \text{Gypsum} + 26\ H \rightarrow \text{Ettringite (calcium aluminosulfo hydrate)}$$

Ettringite (also known as AFt) is a stable hydration product only while there is an ample supply of sulfate available. If the concentration of sulfate in solution drops, then AFt becomes unstable and converts to calcium monosulfate, which is another form of calcium aluminosulfo hydrate:

$$2\ C_3A + \text{Ettringite} + 4\ \text{Water} \rightarrow \text{Monosulfate (AFm)}$$

The hydration of C_3A is slowed down as AFt creates a diffusion barrier around C_3A, which is analogous to the behavior of C_3S during its hydration. This barrier breaks down during the conversion to AFm, and it allows C_3A to react rapidly again. The calorimeter curve for hydrating C_3A qualitatively looks much like the curve for C_3S, although the underlying reactants are quite different, and the amount of heat evolved is much greater (-62 KJ/mole). The first heat evolution peak is completed in 10 to 15 minutes. It is primarily due to the formation of ettringite. The onset of the second peak coincides with the beginning of the conversion of AFt to AFm, and it depends on the amount of sulfate available. The more gypsum there is in the system, the longer the AFt will remain stable. Conversion to AFm will occur in most cements within 12 to 36 hours, after all the gypsum has been used up to form AFt. Thus, the formation of AFm occurs because of a deficiency of sulfate ions to form AFt. When AFm is brought into contact with a new source of sulfate ions, then AFt can form once again. Gypsum is added to portland cement clinker to curb the vigorous initial reaction of C_3A with water, which can lead to flash set due to the rapid formation of calcium aluminate hydrates, such as follows:

$$C_3A + 21\ H \rightarrow C_4AH_{13} + C_2AH_8 \qquad -340\ KJ/mole$$

These hydrates are not stable and convert readily to yet another hydrate, C_3AH_6. The high heat evolution means that the temperature of hydrating C_3A pastes can easily rise several tens of degrees Celsius. Above 30 C, conversion of C_4AH_{13} and C_2AH_8 to C_3AH_6 is very rapid. Formation of aluminohydrates around the grains further retards the hydration of C_3A, but their conversion to C_3A_6H destroys this layer to allow rapid hydration. The rate of conversion depends on temperature.

Hydration of Ferrite

C_4AF forms the same sequence of hydration products as does C_3A in the presence of gypsum, but the reactions are slower and evolve less heat. C_4AF seldom hydrates rapidly enough to cause flash set, and gypsum retards C_4AF hydration even more drastically than it does C_3A. Changes in the composition of ferrite phase, which is a solid solution, only affects the rate of hydration. For example, as the iron content is raised, hydration becomes slower. In the absence of sulfate ions, sulfate-free AFm phases are formed. The

thermodynamically stable phase is $C_4(A.F)_8$, which is analogous to C_3AH_8 in the iron-free system.

As far as reaction kinetics, the rate of hydration during the first few days is of the approximate order:

$$C_3A > C_3S > C_4AF > C_2S$$

Reactivity is influenced by particle size and particle size distributions, determined by the extent and nature of grinding and fineness, and the rate of cooling of the clinker. There are several additional factors, such as the reactivity of the clinker compounds is affected by the presence of impurities, which probably explains the fact that alite and belite (impure C_3S and C_2S as they occur in clinker) hydrate faster than pure C_3S and C_2S. The hydration of C_3A and C_4AF phases also will be affected by these factors.

Development of Porosity

Hydrating concrete generally is assumed to consist of (a) unreacted cement, (b) hydration product, and (c) capillary pores. The hydration product is collectively referred to as the 'cement gel' although it does consist of hydrated lime (CH), which is generally considered to be crystalline in nature and contains no porosity. Therefore, during the hardening process, porosity in the CSH, referred to as 'gel' space (above a water-cementitious ratio (w/cm) of 0.38), also consists of 'capillary' space (Taylor, 1990). The water present in the paste is also generally divided between evaporable and non-evaporable water. Evaporable water resides in both the capillaries and the gel where the water in the gel is referred to as 'gel' water. It is interesting to note that cement paste absorbs additional water (0.06 lb per pound of cement) during 'wet' curing, which causes the total w/cm to exceed the initial w/cm (Figure 1-4). As hydration proceeds, the volume of capillary pores decreases and the volume of gel pores increases. Ultimately, the volume of the hydration products exceeds the original volume of the cement (V_c). The ratio of the volume of hydration products to that of the cement from which it is formed $1+\frac{0.38}{D_cV_c}=2.20$ where D_c = 1000 m^3/kg (Taylor, 1990; Powers,1962). The volume of the hydration product is

$= \left(V_c + \frac{0.38}{D_c} \right) \alpha$ where α is the degree of hydration. Figure 1-4 indicates a defined break at a w/c of 0.38 (Taylor, 1990; Powers, 1962). Above this value:

$$\frac{w_e}{c} = \frac{w_t}{c} - 0.227$$

and below:

$$\frac{w_e}{c} = 0.482 \frac{w_t}{c}$$

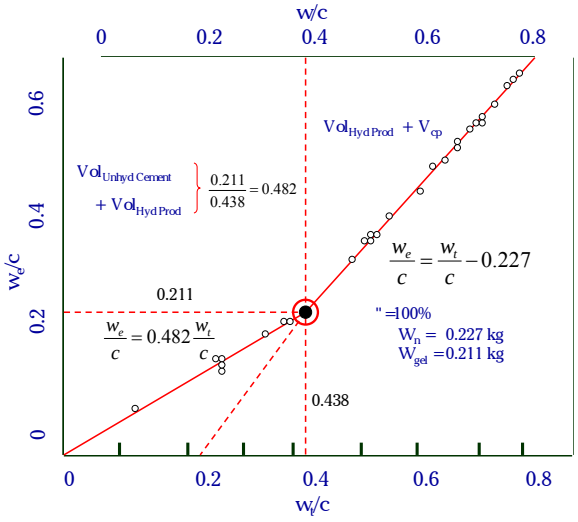

Figure 1-4 Relationship between Initial (w/c), Evaporable (w_e/c), and Total (w_t/c) Water-Cement Ratios for Mature, Saturated Cement Pastes. (Taylor, 1990; Powers, 1962).

It is important to point out curing cement pastes at a w/c < 0.38 does not provide sufficient water to fill the gel pores, leaving the capillary pores empty. It is believed if the relative humidity of the concrete drops below 80 percent, hydration will come to a stop. Water removed from the 'gel' and partial emptying of the capillary water for hydration leads to self-desiccation, which may retard hydration and reduce the final strength. It is important to provide adequate protection against evaporation during the hardening process.

Figure 1-5 illustrates volumetric relationships among the different types of porosities that exist in concrete. Key volumetric qualities are (Taylor, 1990; Powers, 1962):

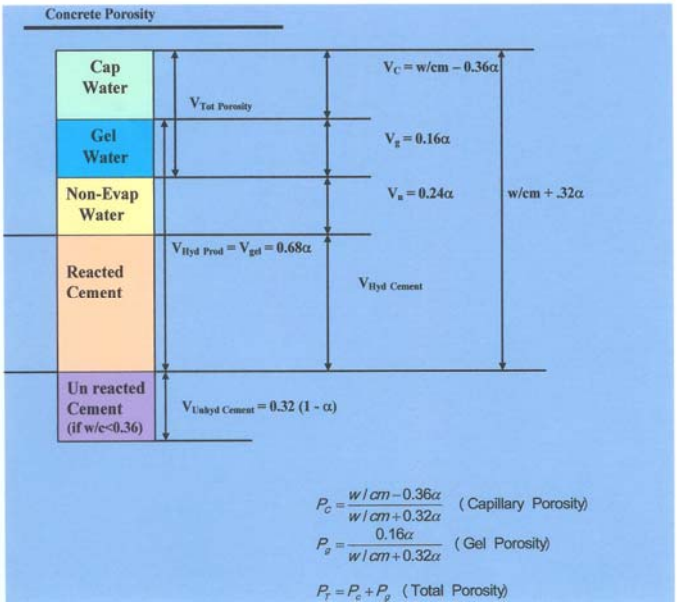

Figure 1-5 Depiction of Porosity in a Cement Paste (Powers, 1962).

Volume of unreacted cement = $V_c(1-\alpha)$

$$\text{Specific volume of non-evaporable water} = \frac{\frac{0.38}{D_c} - V_g m_g}{m_n} = \frac{\frac{0.38}{D_c} - 0.21}{0.23}$$

where V_g is the specific volume of the non-evaporable water; m_g is the mass of gel water per unit mass of cement and is typically about 0.21; m_n is the mass of non-evaporable water per unit mass of cement and is typically about 0.23 (Taylor, 1990; Powers, 1962). The relationships for capillary, gel, and total porosity are shown in Figure 1-5.

DRYING SHRINKAGE

Soon after placement, the concrete may exhibit plastic shrinkage as a result of loss of water by evaporation from the surface of the concrete. The plastic shrinkage induces tensile stress at the surface and may result in surface cracking that is, in general, closely spaced, very tight, and penetrating only up to a couple of inches from the surface. In the construction of a concrete pavement, the occurrence of plastic shrinkage cracking is not common because of good construction practices and relatively stiff concrete mixtures.

As the concrete hydrates, some shrinkage takes place in absence of additional water as hydration takes up some free water. This shrinkage is referred to as autogenous shrinkage and is typically about 50 to 100 micro-strains. When water is supplied continuously, concrete will expand due to absorption of water by the cement gel. However, this process is known as swelling and is a rare occurrence in concrete pavement construction.

Loss of water from hardening concrete is referred to as drying shrinkage. Concrete exposed to ambient conditions undergoes drying shrinkage where some of it is not reversible. Drying shrinkage is influenced by the ambient humidity, aggregate content, concrete to exposed surface ratio, and water to cement ratio of the concrete mix. For concrete exposed to ambient conditions, about 20 to 30 percent of the ultimate shrinkage takes place within the first 2 weeks and about 80 percent within 1 year. Loss of moisture is a characteristic of concrete that is related to the environmental conditions at the time of construction and the porosity of the concrete matrix. Drying shrinkage depends to a great extent on the amount of moisture loss, the quality of curing, the water-cement ratio used to

place the concrete pavement, and the volume of aggregate in the concrete. The amount of drying shrinkage typically ranges from 400 to 600 μ, but may be greater, particularly under hot weather paving conditions. Drying shrinkage is the primary contributor to the development of cracking and must be controlled such that it is not too high or reduced to where it is too small. Loss of moisture can also affect concrete strength.

A study was conducted by the Bureau of Public Roads (Hart, 1926) to evaluate the effects of variations in moisture on the behavior of concrete slabs. However, a major handicap in most of the early studies and even now has been the lack of reliable techniques to measure the moisture state within a concrete slab. Another handicap has been the lack of procedures to measure drying shrinkage induced strain in the field. Nonetheless, it generally is accepted that warping is intensified during summer months and is somewhat less in magnitude during winter months.

A portion of drying shrinkage that occurs in concrete is not reversible. Recent research indicates that drying takes place mainly at the slab surface and that the moisture content of the concrete is practically constant through the thickness. Janssen (1987) concluded from the results of field tests, laboratory tests, and computer modeling that significant drying in concrete pavement usually occurs only at a rather shallow depth. This ingenuity causes nonlinear drying shrinkage throughout the slab thickness, which acts in a manner similar to what the nonlinear temperature distribution does.

Although the amount of drying shrinkage that concrete will ultimately develop is difficult to predict, if evaporation rates are too low for continuous reinforced concrete (CRC) pavement construction then a potential for long crack patterns exists. If the evaporation is too high, then short crack patterns and reduced concrete strengths can result. It is evident that the minimum and maximum shrinkage limits need to be established for optimum crack development and performance of CRC pavement systems.

Process of Drying Shrinkage in Hardening Concrete

As noted above, drying shrinkage occurs as a result of evaporation of pore water to the surrounding environment, and it is probably the most widely recognized cause of volume change in concrete. When concrete is in a dry condition, the evaporation removes free water from the surface of the concrete and larger pores. However, initial loss of free

water causes very little or no shrinkage. As drying develops in the concrete, water in the small pores moves through the larger pores as it migrates toward the drying surface. It is known that the loss of adsorbed water that is physically bound in small capillary pores and gel pores is most responsible for drying shrinkage (Powers, 1959). Several mechanisms for drying shrinkage have been proposed: capillary tension, surface free energy, and disjoining pressure (Powers, 1968; Wittman, 1968; Bažant, 1970; Mindess and Young, 1981). These theories explain the mechanism in a physically meaningful way by the thermodynamic considerations within the microstructure of hydrated cement paste. Among them, disjoining pressure is known to dominate the drying shrinkage of concrete when pore relative humidity is above 40 percent (Wittmann, 1982).

A similar mechanism of drying shrinkage applies to the autogenous shrinkage. The difference is that the capillary and gel pore water is driven to move by the external evaporation in drying shrinkage, while it is consumed internally by the hydration in autogenous shrinkage. Contributions of each phenomenon to the total volume change will vary with time, concrete mix compositions, and environmental condition. Figure 1-6 represents schematically the relationship between the components of moisture-related volume changes in hardening concrete. The total shrinkage, counted from the time of casting, would consist of plastic deformation, autogenous shrinkage, and drying shrinkage. As discussed, however, the plastic deformation can be regarded as stress-free movement even in restrained conditions. Therefore, for the purpose of stress analysis, the origin of Figure 1-6 should move to point *A*. The total shrinkage with the new origin A is termed '*apparent total shrinkage*', which is in fact a parallel reduction of total shrinkage by the amount of plastic deformation at the time of initial setting (t_0). The relationship between the hygral shrinkage components can be represented as:

$$\varepsilon_{TOT} = \varepsilon_{AS} + \varepsilon_{DS} + \varepsilon_{PD} = \hat{\varepsilon}_{TOT} + \varepsilon_{PD}$$

$$\hat{\varepsilon}_{TOT} = \varepsilon_{AS} + \varepsilon_{DS}$$

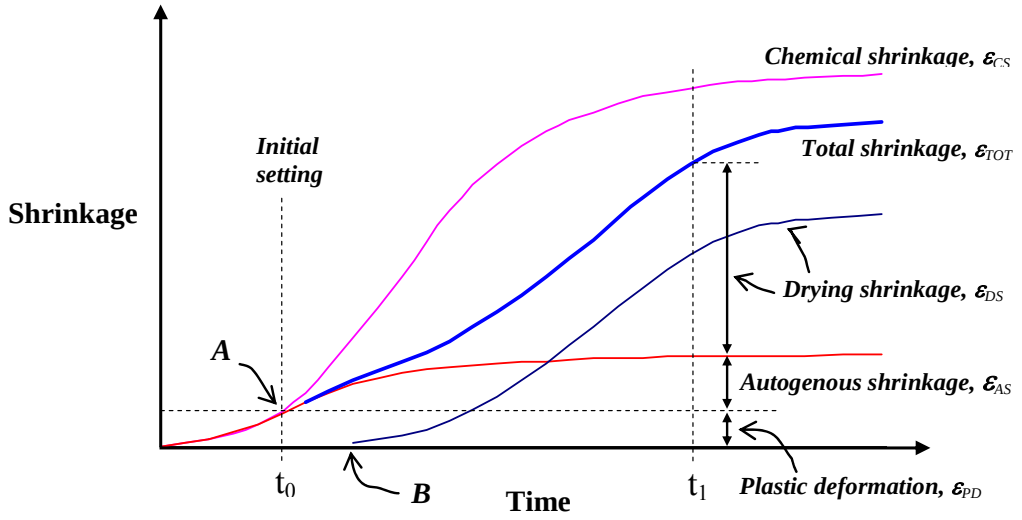

Figure 1-6 Components of Hygral Shrinkage in Early Age Concrete (Lim, 2002).

where ε_{TOT} = total shrinkage since the time of casting

$\hat{\varepsilon}_{TOT}$ = apparent total shrinkage since the time of setting

ε_{PD} = plastic deformation counted from casting to setting

ε_{AS} = autogenous shrinkage

ε_{DS} = drying shrinkage

It is noteworthy that a lag exists between the initiation of autogenous shrinkage and drying shrinkage. Because the cause of autogenous shrinkage is internal consumption that takes place within small capillary and gel pores, the drying tip coincides with the origin of volume change. Therefore, autogenous shrinkage immediately follows the self-desiccation that initiates with initial setting. For the case of drying shrinkage, however, volume change is not an immediate consequence of drying, especially at its initial stage. At the initial stage of drying, evaporation takes place with free water first, and a certain amount of time is required for the drying to reach to the origin of volume change, which is known to be loss of adsorbed water in small capillary or gel pores. Therefore, the initiation of drying shrinkage is likely to occur later than autogenous shrinkage.

Creep is mentioned briefly since it often accompanies shrinkage. Creep can be defined as the increase in strain under a sustained stress and, because this increase can be several times as large as the strain on loading, creep is of considerable importance. The creep of concrete, *c*, the volumetric content of aggregate, *g*, and the volumetric content of unhydrated cement, *u*, are related by (Neville, 1996):

$$\log\left(\frac{c_p}{c}\right) = \alpha \log\left(\frac{1}{1-g-u}\right)$$

where c_p is the creep of neat cement paste of the same quality as used in concrete, and

$$\alpha = 3\frac{1-\mu}{1+\mu+2(1-2\mu_a)\frac{E}{E_a}}$$

where

μ_a = Poisson's ratio of aggregate

μ = Poisson's ratio of the concrete

E_a = modulus of elasticity of aggregate

E = modulus of elasticity of concrete

The modulus, grading, maximum size, and shape of the aggregate are factors that affect creep in concrete with modulus being the most significant. The higher the modulus of the aggregate, the lower the creep. Lightweight aggregates exhibit a high degree of creep due to their low modulus values. The size and grading has indirect influence on the magnitude of shrinkage. The larger aggregate permits the use of a leaner mixture, which results in lower shrinkage. The elastic properties of aggregate also have an effect on the shrinkage of cement paste. Lightweight aggregate usually leads to higher shrinkage, for the same reason noted above, and it offers less resistance to potential shrinkage of the cement paste. Larger void content in concrete also leads to higher shrinkage.

MOISTURE EFFECT ON CoTE

The concrete porosity becomes filled with hydration products with curing time due to hydration reaction between cement and water. The concrete Coefficient of Thermal Expansion (CoTE) is affected by the porosity and moisture availability to the gel-sized pores from the capillary-sized pores. Interestingly enough, the hygral state of concrete has an effect on the CoTE of the concrete in addition to the concrete mixture constituents. The

hydral effect has been noted by past researchers (Neville, 1996; Meyers, 1951) to be related to swelling pressure in the capillary pores resulting from a decrease in surface tension of the port water due to an increase in temperature. Figure 1-7 illustrates key research findings regarding the effect of moisture on CoTE. No effect on the concrete CoTE has been found when the cement paste is dry (relatively speaking) or when the cement paste is saturated. It also is noted that the free exchange of water between the gel and the concrete capillaries occurs only at saturated conditions.

When the concrete temperature is increased, the water moves from the gel to the capillaries and then back upon a temperature decrease. Volumetrically, this exchange of water is neutral due to the offsetting effects of expansion and contraction in either the capillaries or the gel depending on the direction of the water movement. This mechanism of free exchange of water does not occur in the partially saturated conditions. When the cement paste is dry (i.e., w/cm <0.38) – the capillaries are unable to provide water to the gel when swelling occurs under an increase in temperature. When the concrete is in a saturated state, no menisci are present, and consequently, no change in surface tension under a change in temperature will occur. Therefore, at these limits, measured CoTE values are lower. At moisture contents between limits, there is sufficient water to form a meniscus and, thus, surface tension is present in the water yielding a change in volume as the temperature changes.

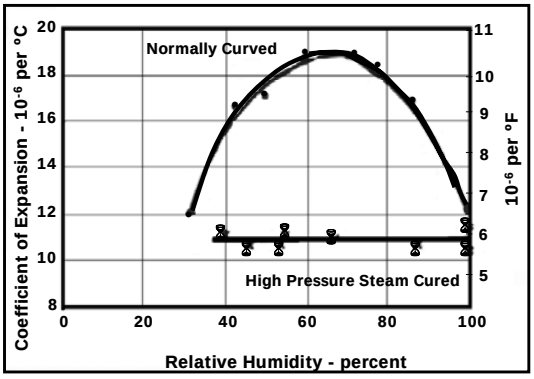

Figure 1-7 Moisture Effect on CoTE (Meyers, 1951).

Laboratory Test Program

The research team carried out a laboratory test program to investigate age and moisture effects on the CoTE of concrete. A cylinder mold with both inside diameter and height of 30.5 cm (12 inch) was prepared. The mold consisted of 1.3 cm (0.5 inch) thick PVC wall and an end plate. The mold was not removed until the end of the test so that the

concrete was allowed to dry only through the top surface. Before placing concrete, vibrating wire strain gauges were instrumented inside the mold 2.5, 7.6, and 17.8 cm (1, 3, and 7 inch) from the top as shown in Figure 1-8. Brass casings were threaded into the wall of the mold at the same depths.

Concrete was placed in the mold and was compacted according to ASTM C 192. Table 1-1 presents the mix proportions of the specimen. A water-cement ratio of 0.32 was used, and the unit weight of concrete was determined by ASTM C 29 and was found to be 2349 kg/m^3 (146 lb/ft^3). Immediately after the placement, the specimen was moved to an environmental chamber with 60 ^{o}C and 15 percent of temperature and relative humidity, respectively. Three and a half hours after the placement, three temperature and moisture monitoring systems manufactured by ATEK were placed 2.5, 7.6, and 17.8 cm (1, 3, and 7 inch) from the top surface to measure temperature and relative humidity of the concrete.

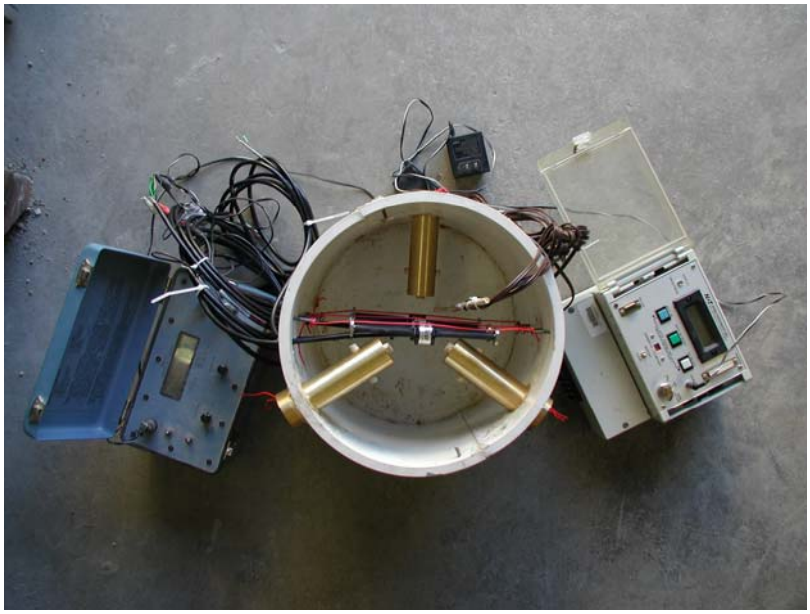

Figure 1-8 Instrumented 30.5 × 30.5 cm PVC Cylinder Mold.

Initial Temperature and Moisture of Concrete

Temperature, relative humidity, and strain of the cylinder specimen at each depth were investigated for 20 weeks. Initial 21 days of temperature

Table 1-1 Mix Proportions in 1 m^3 (35.3 ft^3) of Cylinder Specimen Concrete.

Materials	Proportions
Coarse Aggregate (Sandstone)	1,076 kg (2,372 lb)
Fine Aggregate (Fordyce)	869 kg (1,916 lb)
Cement (Type I)	281 kg (618 lb)
Fly Ash (Type C)	120 (264 lb)
w/c Ratio	0.32
Superplasticizer (Reobilt 1000)	2,745 ml (92.7 oz)

and relative humidity results are presented in Figure 1-9 because there were little changes in the data after 21 days from placement. The concrete temperature at the time of placement was 23 ^{o}C, and the maximum temperature was 62 ^{o}C approximately 10.5 hours after placement as shown in Figure 1-9 (a). Subsequently, the temperature of the specimen stabilized near 60 ^{o}C throughout its depth.

Initial relative humidity was much below 100 percent and then increased steadily until approximately 15 to 20 hours after placement as shown in Figure 1-9 (b) though the concrete was expected to be saturated at the time of placement. The initially measured low relative humidity of concrete is due to the effect of bleeding and subsequent significantly high values of moisture diffusivity in the hardening concrete (Jeong and Zollinger, 2003). Low vapor pressure of the concrete due to high moisture diffusivity results in low initial relative humidity. Moisture in the concrete exists in the form of free water at this stage. As the hydration takes place, capillary pores are generated, and the pore vapor pressure becomes higher. Because of low curing relative humidity in the environmental

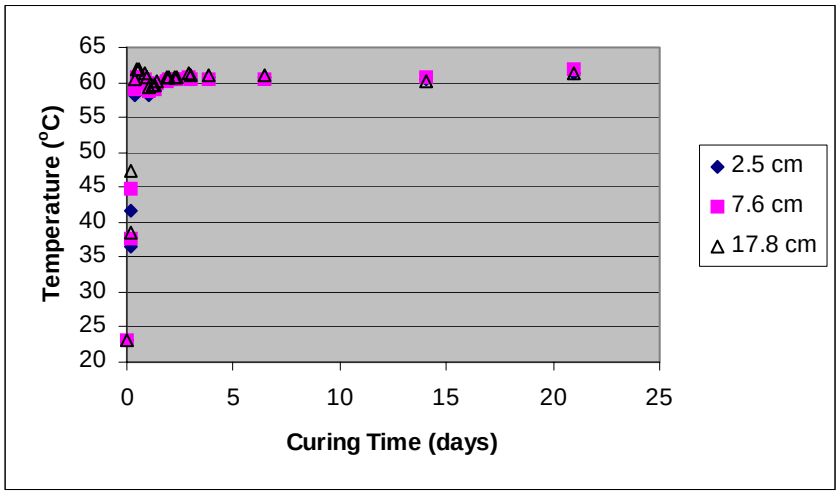

(a) Temperature

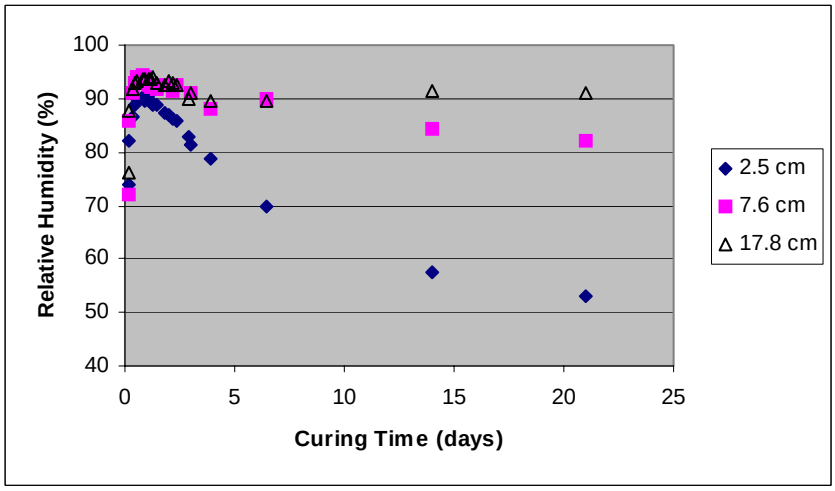

(b) Moisture

Figure 1-9 Temperature and Moisture Histories at Different Depths of Specimen.

chamber, the relative humidity near the top surface of the specimen decreased substantially for 21 days of measurement due to the high level of evaporation. The relative humidity reached to 53, 82, and 91 percent at 2.5, 7.6, and 17.8 cm (1, 3, and 7 inch) depths, respectively, at 21 days after placement.

Moisture Effects on CoTE of Concrete

Concrete strain was tensile until 10.5 hours (maximum temperature) of curing time because of the temperature increase. During that period, the concrete strain consisted of shrinkage and thermal strains. Consequently, the concrete experienced compressive strain although the concrete temperature was already stabilized and maintained at the same level. Concrete strain was the same as the shrinkage strain during the period because thermal strain did not exist. Higher relative humidity and smaller shrinkage strain at 17.8 cm (7 inch) depth than other shallower depths shown in Figures 1-9 (b) and 1-10 indicate that drying hardly occurred at deeper positions of the specimen. Thus, most of the concrete strains measured at 17.8 cm (7 inch) depth from 10.5 hours to 7 days of curing time was expected as autogenous shrinkage (AS) because self-desiccation occurs at all positions of the specimen during its hydration process. Autogenous shrinkage of the specimen was calculated based on a model developed by Hedlund and Westman (1999).

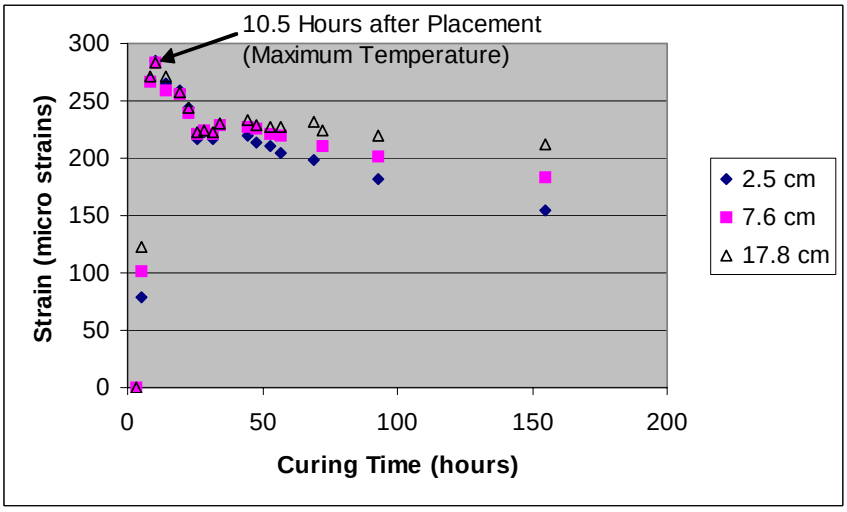

Figure 1-10 Concrete Strain at Different Depths of Specimen.

$$\varepsilon_{AS} = \left(-0.6 + 1.2\frac{w}{b}\right) \times 10^{-3}$$

where

ε_{AS} = autogenous shrinkage

w = water content

b = binder (cement and fly ash) content

Figure 1-11 verifies the fact that a major portion of the measured shrinkage strain is autogenous in nature at a depth of 17.8 cm for the initial 7 days. Thermal strain at 17.8 cm (7 inch) depth of the specimen was calculated by subtracting the calculated autogenous shrinkage from the measured concrete strain. The CoTE of the specimen was determined by changes in the thermal strain and temperature of concrete. A higher CoTE value could be calculated by subtracting the autogenous shrinkage from the measured concrete strain as shown in Figure 1-12. Initial high CoTE stabilized to a value between 11 and 12 micro strains/^{o}C around 10 hours after placement. The CoTE of 11.2

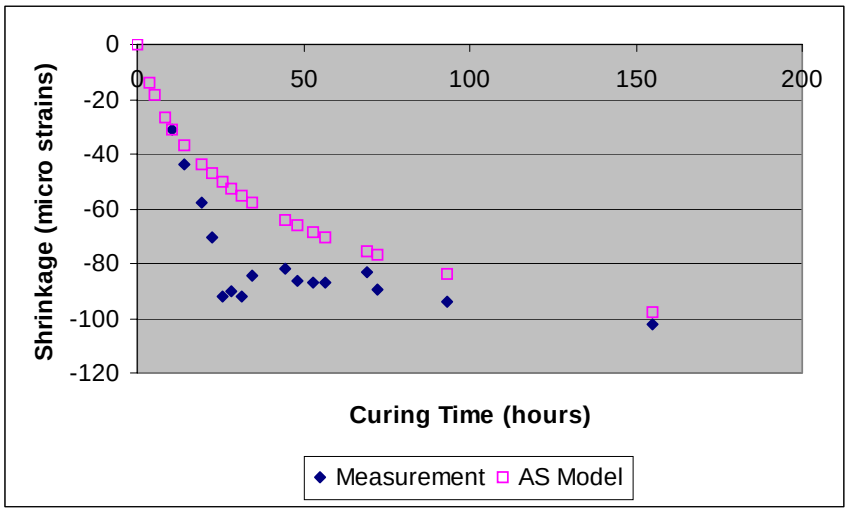

Figure 1-11 Comparison between Measured Total Shrinkage and Calculated Autogenous Shrinkage at 17.8 cm Depth.

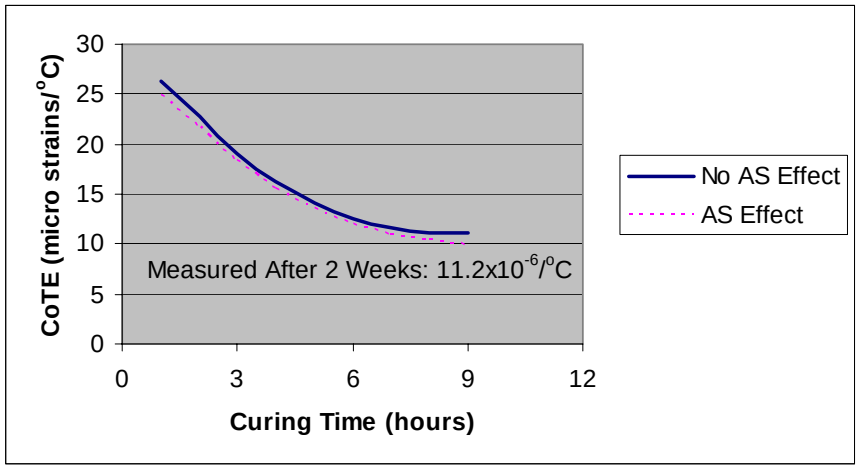

Figure 1-12 Age Effect on Concrete CoTE.

micro-strains/^{o}C measured 2 weeks after placement indicates the CoTE at 10 hours already had stabilized, and concrete age affects concrete CoTE at its very early age.

The cylinder specimen was cured in the environmental chamber for 6 months. During the period, the specimen was moved from a 60 ^{o}C chamber to a 10 ^{o}C chamber periodically to cause the changes in concrete temperature and strain at different curing times. At each test, the specimen returned to the 60 ^{o}C chamber immediately after the concrete temperature stabilized to 10 ^{o}C. CoTE and relative humidity were measured at the same time, while the concrete temperature changed in both chambers. While the specimen was chilled in the 10 ^{o}C chamber, the concrete relative humidity increased because of the volume contraction of the specimen due to the temperature decrease effected on the moisture condition in the pores. The increased relative humidity returned to its original level when the concrete temperature returned to 60 ^{o}C. The relative humidity of the specimen steadily decreased during the test period causing the drying shrinkage. The maximum peak of CoTE was made around 85 percent relative humidity as shown in Figure 1-13. Minimum CoTE could be found near 100 percent and below 50 percent relative humidity. This moisture effect is due to the availability of water to the gel-sized pores from the capillary-sized pores. Therefore, based on the studies of age and moisture effects on CoTE, concrete with low porosity would not be as susceptible to the moisture effect as normal concrete with typical porosities. Analysis of the data trends in Figure 1-8 and Figure 1-13 suggests that a correction factor should be applied to the CoTE of concrete determined at a saturated condition. The range of this correction is approximately from 1.0 to 1.54. The data trends also suggest that a Weibull type probability density function could be used to fit the distribution of the

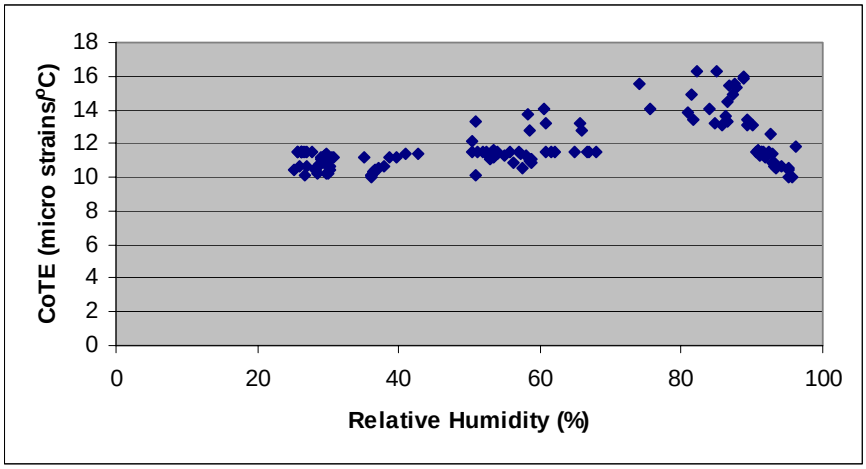

Figure 1-13 Moisture Effect on Concrete CoTE.

correction with relative humidity since it is clear that the distribution of the correction (referred to as a correction factor [CF]) is a function of the relative humidity. The form of an expression for the CF is:

$$CF = 1.542 \cdot \frac{\gamma}{\alpha}\left(\frac{rh - v}{\alpha}\right)^{\gamma-1} e^{-\left(\frac{rh-v}{\alpha}\right)^{\gamma}}$$

where v = 0.35, γ = -1.55, and α = 0.525. This correction is applicable in the range of 70 to 100 percent relative humidity and is particularly useful for concrete located within 7.6 cm (3 inch) of an evaporable surface, since this is where the majority of moisture change occurs.

CHAPTER 2
MOISTURE TRANSPORT IN CONCRETE PAVEMENT CONSTRUCTION

INTRODUCTION

The nature of the moisture profile in hardening concrete particularly near the evaporative surface has become the subject of great interest due to its apparent long-term impact on pavement performance. Again, as previously noted, the distribution and history of moisture at an early age plays a key role in this impact. Its prediction is the focus of this chapter and provides the means to assess the effect of moisture and the method of curing on drying shrinkage, thermal expansion, strength, maturity, and curing efficiency. Although some experimental data have been assembled over many years of research, little data at early ages of drying concrete are presently available.

Aspects of the effect of moisture in concrete pavement can be reflected in concrete strength, drying shrinkage, and creep development in the early stages of hydration. These behavioral characteristics are of concern with respect to early-age concrete slab deflections that subsequently affect the formation of early-aged cracking and delamination shear stress. Material-related moisture properties (permeability, diffusivity, slope of the moisture isotherm, etc.) of concrete play a key role in the mathematical modeling and representation of stress and strain due to drying shrinkage and creep under varying humidity conditions. Material tests are necessary to determine these pertinent material properties. Moisture flow models that represent the variation of moisture with time use these properties. In terms of engineering applications, prediction of humidity and water diffusion is very important in consideration of spalling, warping, and other moisture-related stresses, strains, and deformations induced in concrete pavements.

Based on this perspective, the research team developed mathematical models for the calculation of moisture and temperature profiles to help understand the effect of different combinations of climate, construction, and materials on the development of the moisture and temperature profiles and their subsequent effects on early shrinkage, cracking, and delamination. These models appear as nonlinear time-dependent partial

differential equations and are solved by finite element and other similar numerical methods simultaneously that involve both backward and forward calculation. Using measured test data, moisture diffusivity and thermal conductivity can be back-calculated to facilitate accurate modeling of moisture and temperature flows in hardening concrete. As will be shown, the calculated moisture and temperature profiles using the moisture diffusivity and thermal conductivity models corresponded well to measured data. Field data collected under this study are presented in Appendixes A, B, and C. Calibration efforts beyond those reported in this chapter are described in Appendix C.

THE NATURE OF MOISTURE MOVEMENT

Drying shrinkage and creep strains are related to the amount of movement and distribution of moisture in a concrete slab. These moisture-related strains are of concern with respect to the warping-related deformation of the slab and possible formation of early-aged cracks or development of shallow delaminations just below the pavement surface. The prediction of movement and distribution of moisture is important for estimation of warping behavior and other moisture-related stresses, strains, and deformations of the slab. In the past, a method used to determine the moisture in concrete was by actual measurement of weight loss of small laboratory samples. Recently, quantities of moisture have been directly measured using moisture sensors with the recent development of instrument and measurement techniques. Moisture flow and diffusion in concrete have been a significant topic in the research of concrete pavement materials (Bažant and Najjar, 1972; Parrott, 1988; Parrott, 1991; Xin et al., 1995; Buch and Zollinger, 1993).

Moisture movement in concrete has substantially high initial moisture diffusion rates followed by gradually lower moisture diffusion rates 10 to 12 hours after placement. This drying characteristic is inherently related to a material property referred to as the moisture diffusivity (D), which has been generally accepted to be dependent upon the pore water content within the cement paste. It has been observed that the value of the moisture diffusivity may change significantly with variations in the moisture content or the relative humidity (from 100 to 70 percent) of the concrete (Pihlajavaara, 1964; Kasi and Pihlajavaara, 1969; Bažant, 1970; Bažant and Najjar, 1972). At a constant water

content (w), moisture diffusivity changes little with time in mature concrete though it changes greatly during the first 24 hours after placement of fresh concrete. This research has shown that diffusivity in early-aged concrete has been found to be a function of not only humidity but also age of concrete and porosity of cement paste. The moisture diffusivity is important in modeling moisture flow in hardening concrete.

The rate of moisture flow through concrete can be expressed by the velocity of flow (J) representing the mass of evaporable water passing through a unit area perpendicular to the direction of flow per unit time. The velocity of flow by Darcy's law is derived from energy gradients (Bažant and Najjar, 1972):

$$J = -C \cdot grad\ \mu \tag{2-1}$$

where μ is Gibb's free energy (GFE) per unit mass of evaporable water and the coefficient C characterizes the permeability of the pores of concrete. Equation (2-1) is restricted to small energy gradients and laminar flow conditions. Assuming water vapor behaves as an ideal gas, Gibb's free energy is (Bažant and Najjar, 1972):

$$\mu = \left(\frac{RT}{MV_w}\right) \cdot \ln H + \mu_{sat}(T) \tag{2-2}$$

where

R = universal gas constant (8.3143 J/mol/^{o}K)

T = absolute temperature (^{o}K)

M = molecular weight of water (18.015 g/mol)

V_w = specific volume of water (1 cm^3/g)

H = humidity of concrete $\left(= \frac{RH}{100}\right)$

RH = relative humidity of concrete (%)

μ_{SAT} = Gibbs Energy at Saturation

Equation (2-1) can be rewritten in terms of temperature (T) and humidity (H) of concrete as (Bažant and Najjar, 1972):

$$J = -c \cdot grad\ H \tag{2-3}$$

where the coefficient c is permeability as a function of temperature and humidity of concrete as below (Bažant and Najjar, 1972).

$$c = \left(\frac{RT}{MV_w}\right) \times \left(\frac{C}{H}\right) \tag{2-4}$$

The relationship between humidity and water content within concrete at a constant temperature and the degree of hydration is described by desorption or sorption isotherms (Bažant and Najjar, 1972). It is evident that the relationship between the moisture and the measured humidity of concrete will vary as a function of the age. The dependence of the evaporable water content on humidity (as a function of temperature) is a function of the porosity of the pore structure within the cement paste and is represented empirically in the form of desorption or sorption isotherms that are illustrated in Figure 2-1. It should be noted that the isotherm for sorption is different from the isotherm for desorption. This characteristic may be due to the various states of equilibrium of the pore

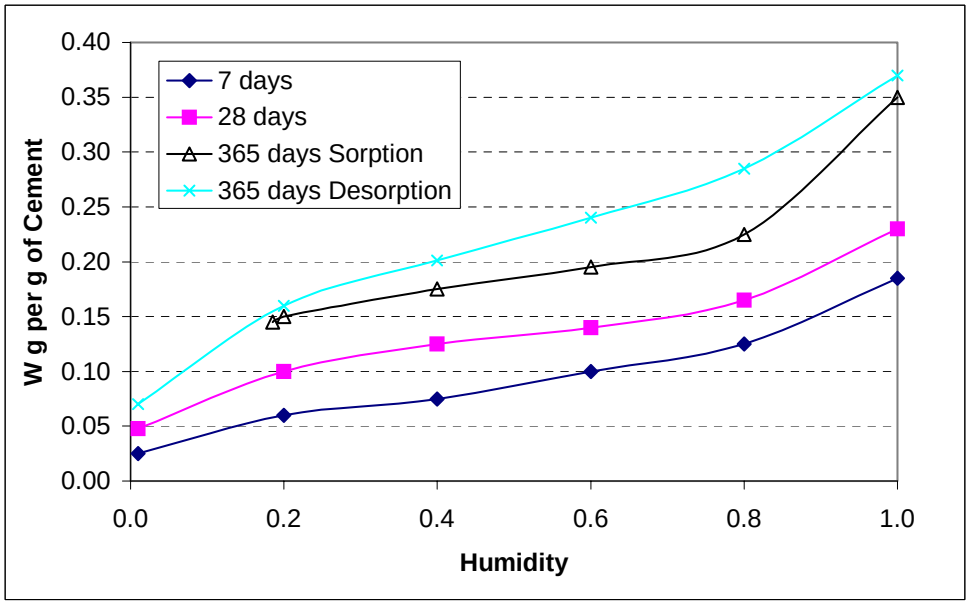

Figure 2-1 Desorption-Isotherms (Bažant, 1970).

water. An investigation by Parrott (1988) implied the significance of porosity with respect to the position of the desorption or sorption isotherm within concrete. The results indicated that a greater amount of moisture loss in drying concrete would occur in regions nearest to exposed drying surfaces, which may be also regions of greater porosity. This observation was proven in the relationship between weight loss and relative humidity of concrete indicated in Figure 2-2. Therefore, it can be explained that there is a greater

volume of coarse pores at positions nearer to an exposed concrete surface and, consequently, the relationship between weight loss and relative humidity of concrete will

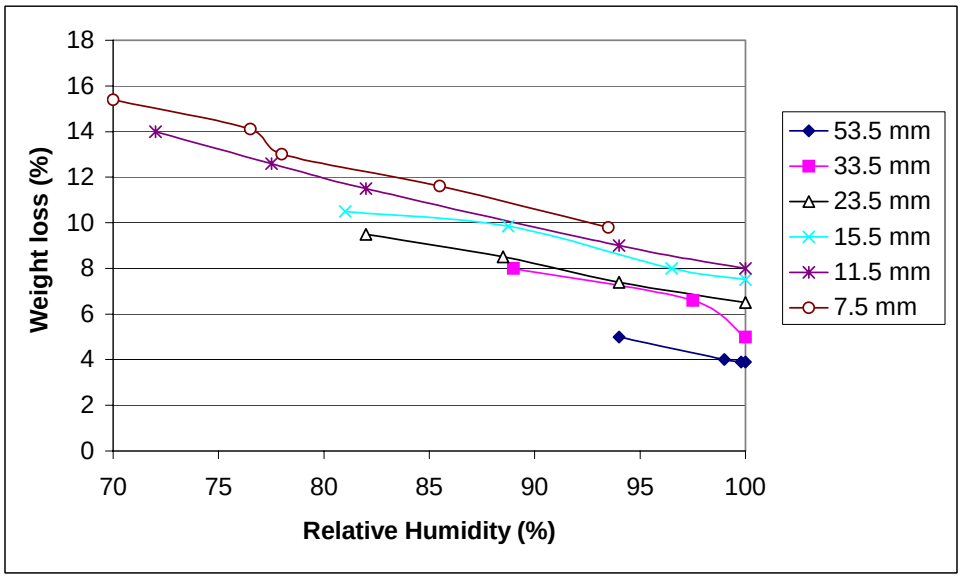

Figure 2-2 Weight Loss versus Relative Humidity of Drying Concrete at Various Vertical Distances from the Exposed Surface (Parrott, 1988).

vary with distance from the exposed surface. In this respect, the performance and behavior of a concrete pavement may be affected by the porosity of the surface. It also should be noted that the resulting desorption isotherm at any time during hydration of hardening slab concrete must be interpreted not only as a function of the degree of hydration, but also as a function of porosity. At a given porosity, the desorption isotherm may be expressed in the differential form as (Bažant and Najjar, 1972):

$$dH = kdw \tag{2-5}$$

$$k = \left(\frac{\partial H}{\partial w} \right) \tag{2-6}$$

where the parameter k represents the slope of the moisture isotherm where the mass of water (w) is described as a function of humidity (H). Moisture movement in an unsaturated porous medium is effected by temperature profiles of the medium (Huang, 1979; Suh et al., 1988; Somasundaram et al., 1989). Thus, the calculation of humidity in hydrating concrete requires additional terms under variable temperature conditions as (Bažant and Najjar, 1972):

$$dH = kdw + KdT + dH_s \tag{2-7}$$

where

K = hygrothermic coefficient $= \left(\frac{\partial H}{\partial T}\right)$

dH_s = change in humidity (H) due to hydration at a constant water content (w) and time (t)

The hygrothermic coefficient represents the change in humidity due to one degree of change in temperature at a constant water content and a given level of hydration. It should be noted that the pore water content (w) includes both the evaporable or capillary water (w_c) and the non-evaporable water (w_n) per unit volume of materials.

The rate of moisture flow in unit volume of concrete is determined from (Bažant and Najjar, 1972):

$$\frac{\partial w}{\partial t} = -divJ \tag{2-8}$$

Substituting equation (2-3) into equation (2-8) and subsequently substituting equation (2-8) into equation (2-7) leads to (Bažant and Najjar, 1972):

$$\frac{\partial H}{\partial t} = k \cdot div(c \cdot gradH) + \frac{\partial H_s}{\partial t} + K\frac{\partial T}{\partial t} \tag{2-9}$$

which is the diffusion equation for the drying concrete under variable temperature conditions. Equation (2-9) is further developed to be equation (2-34).

$$\frac{\partial H}{\partial t} = kc\frac{\partial^2 H}{\partial x^2} + k\frac{\partial c}{\partial x}\frac{\partial H}{\partial x} + \frac{\partial H_s}{\partial t} + K\frac{\partial T}{\partial t} \tag{2-10}$$

Permeability (c) is also a function of the porosity and indirectly a function of position x. Because permeability change with position x is assumed to be very small, the second term in equation (2-10) is considered to be negligible and is consequently dropped from the diffusion equation as:

$$\frac{\partial H}{\partial t} = D\frac{\partial^2 H}{\partial x^2} + \frac{\partial H_s}{\partial t} + K\frac{\partial T}{\partial t} \tag{2-11}$$

where D (= $k \cdot c$) is moisture diffusivity (L^2/t).

HEAT TRANSFER

From the above discussion, temperature plays a clear role in the movement of moisture in concrete. Consequently, it is useful to document the nature and theory of heat transfer relative to its effect on temperature of hydrating concrete. The control volume in heat transfer theory is a region of space bounded by a control surface through which energy and matter may pass. If the inflow and generation of energy exceeds the outflow, there will be an increase in the amount of energy stored in the control volume, whereas there will be a decrease in energy stored in the case that the outflow of energy exceeds the inflow and generation of energy. If the inflow and generation of energy equal the outflow, a steady-state condition must prevail in which there will be no change in the amount of energy stored in the control volume.

At any point in time, the energy terms include the rate at which thermal and mechanical energy enter and leave through the control surface, $_{in}$ and $_{out}$. Also, thermal energy is created within the control volume due to conversion from other sources of energy. This process is referred to as energy generation, and the rate at which it occurs is designated as $_{g}$. The rate of change in energy stored within the control volume is designated as $_{st}$. A general form of energy conservation is expressed on a rate basis (Incropera and DeWitt, 1996).

$$\dot{E}_{in} + \dot{E}_{g} - \dot{E}_{out} = \frac{dE_{st}}{dt} = \dot{E}_{st} \tag{2-12}$$

Equation (2-12) may be applied at any instant of time. The alternative form for a time interval Δt is obtained by integrating equation (2-12) over time (Incropera and DeWitt, 1996):

$$E_{in} + E_{g} - E_{out} = \Delta E_{st} \tag{2-13}$$

Equations (2-12) and (2-13) imply that the amounts of energy inflow and generation act to increase the amount of energy stored within the control volume, whereas outflow acts to decrease the stored energy.

The inflow and outflow of energy that occurs at the control surface is proportional to the surface area. Additionally, heat transfer that occurs due to conduction, convection, and radiation is involved in the energy inflow and outflow at the control surface. The energy generation term is associated with conversion from other forms of energy such as

the concrete heat of hydration. As concrete hydrates, a chemical reaction takes place generating thermal energy, which is dependent upon the amount and fineness of the cement used in the concrete.

Energy storage changes within the control volume due to changes in the internal, kinetic, and potential energies. Hence, for a time interval, Δt, the energy storage term of equation (2-5), ΔE_{st}, can be equated to $\Delta U + \Delta KE + \Delta PE$ where kinetic and potential energy effects are neglected in heat transfer analysis. The internal energy, ΔU, consists of a sensible or thermal component, which accounts for the translational, rotational, and/or vibrational motion of the atoms/molecules comprising the matter in the control volume; a latent component, which relates to intermolecular forces influencing phase change between solid, liquid, and vapor states; a chemical component, which accounts for energy stored in the chemical bonds between atoms; and a nuclear component, which accounts for binding forces in the nucleus. Accordingly, the rate of change in energy storage in equation (2-12) due to the temperature change in the control volume can be expressed as (Incropera and DeWitt, 1996):

$$\dot{E}_{st} = \frac{dU_t}{dt} = \frac{d}{dt}\left(\rho V c_p T\right) \tag{2-14}$$

where

ρ = density of mass within control volume (kg/m^3)

V = control volume (m^3)

c_p = specific heat (W·hr/kg/^{o}K)

An infinitesimally small control volume, *dxdydz*, is defined and shown in Figure 2-3. If there are temperature gradients in concrete, conduction heat will occur across each of the control surfaces. The conduction heat rates perpendicular to each control surface at the *x*, *y*, and *z* coordinate locations are indicated by the terms q_x, q_y, and q_z, respectively. The conduction heat rates at the opposite surfaces can be expressed as a Taylor series expansion by neglecting higher order terms.

$$q_{x+dx} = q_x + \frac{\partial q_x}{\partial x} dx \tag{2-15}$$

$$q_{y+dy} = q_y + \frac{\partial q_y}{\partial y} dy \tag{2-16}$$

$$q_{z+dz} = q_z + \frac{\partial q_z}{\partial z} dz \tag{2-17}$$

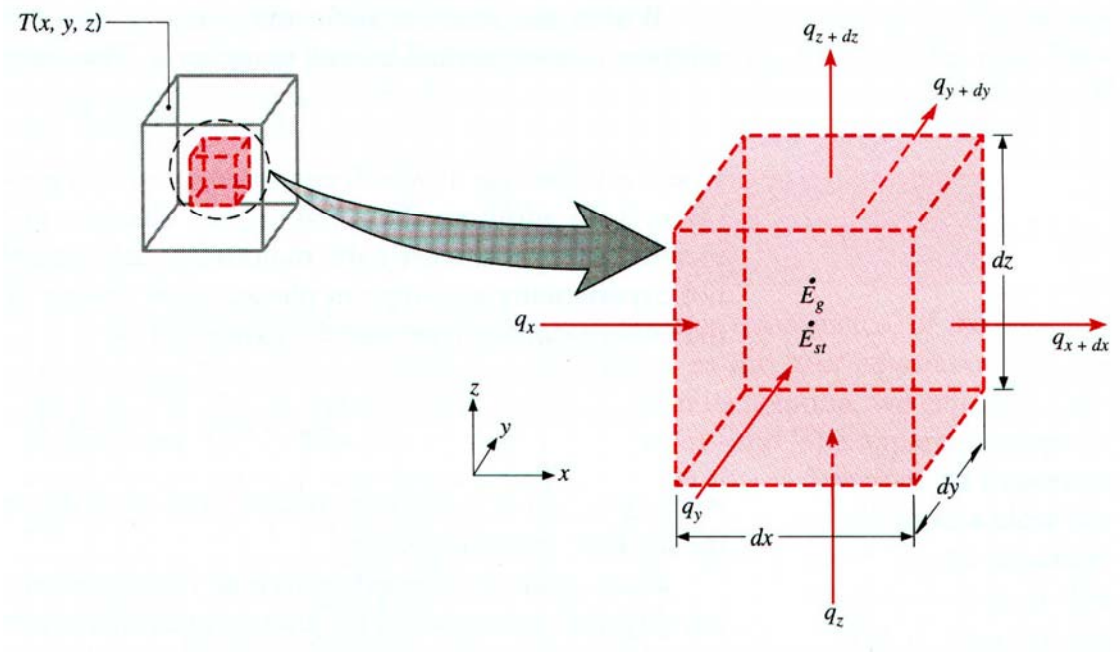

Figure 2-3 Thermal Conduction through an Infinitesimally Small Control Volume (Incropera and DeWitt, 1996).

Within the hydrating concrete, there should be an energy source term associated with the rate of thermal energy generation.

$$\dot{E}_g = \dot{q} dx dy dz \tag{2-18}$$

where $\dot{q}$ is the rate at which energy is generated per unit volume of the concrete (W/m^3). In addition, there may be changes in the amount of the internal thermal energy stored in the control volume of concrete. The energy storage term may be expressed as:

$$\dot{E}_{st} = \rho c_p \frac{\partial T}{\partial t} dx dy dz \tag{2-19}$$

Equation (2-12) is transformed into equation (2-20) by applying the methodology of conservation of energy and by referring equation (2-15) to (2-19) and Figure 2-3 (Klemens, 1969; Siegel and Howell, 1981).

$$q_x - \left(q_x + \frac{\partial q_x}{\partial x}dx\right) + q_y - \left(q_y + \frac{\partial q_y}{\partial y}dy\right) + q_z - \left(q_z + \frac{\partial q_z}{\partial z}dz\right) + \dot{q}dxdydz$$

$$= \rho c_p \frac{\partial T}{\partial t}dxdydz \qquad (2\text{-}20)$$

where

$\dot{q}$ = rate of energy generation per unit volume (W/m^3)

$\rho c_p \frac{\partial T}{\partial t}$ = rate of change of the thermal energy per unit volume (W/m^3)

The conduction heat inflow at the control surface shown in Figure 2-3 can be further expressed by Fourier's law as:

$$q_x = -kdydz\frac{\partial T}{\partial x} \qquad (2\text{-}21)$$

$$q_y = -kdxdz\frac{\partial T}{\partial y} \qquad (2\text{-}22)$$

$$q_z = -kdxdy\frac{\partial T}{\partial z} \qquad (2\text{-}23)$$

where k is the thermal conductivity ($W/m/^oK$). Equations (2-21) to (2-23) are substituted into equation (2-20) and dividing out the dimensions of the control volume ($dxdydz$) to obtain equation (2-24) (Klemens, 1969; Siegel and Howell, 1981).

$$\frac{\partial}{\partial x}\left(k\frac{\partial}{\partial x}\right) + \frac{\partial}{\partial y}\left(k\frac{\partial}{\partial y}\right) + \frac{\partial}{\partial z}\left(k\frac{\partial}{\partial z}\right) + \dot{q} = \rho c_p \frac{\partial T}{\partial t} \qquad (2\text{-}24)$$

Conduction is a mode of heat transfer in which heat is transferred by random molecular motion in a concrete slab, while convection represents a mode of heat transfer in which heat is transported through mixing of hot and cold fluid particles between the slab surface and a moving fluid (i.e., wind). Heat transfer by radiation represents the transmission of energy by electromagnetic waves. For concrete pavement, radiation and convection play a dominant role in transferring heat between the slab surface and the surrounding air, while conduction plays a separate role in transferring heat within the slab as shown in Figure 2-4.

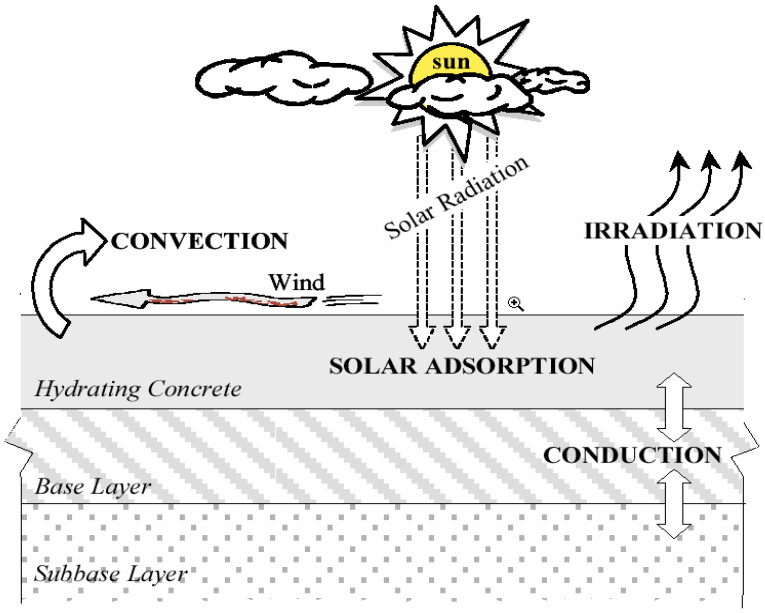

Figure 2-4 Heat Transfer Mechanisms between Pavement and Its Surroundings (Ruiz et al., 2001).

Conduction

Heat conduction is explained as heat transfer from points of higher temperature to points of lower temperature in a concrete slab. Heat energy is transferred within the slab due to interaction between the particles of different temperatures. Molecules at a high temperature are said to have high energy, which makes the molecules themselves randomly translate, and internally rotate and vibrate. Heat energy transferred by these random molecular motions is called energy diffusion. Conduction can also be expressed by using Fourier's law in the form of a rate equation. Conduction for a temperature distribution, *T,* in one dimension can be expressed as a function of direction *x* as (Klemens, 1969; ASHRAE, 1972):

$$q''_{cond} = -k\frac{dT}{dx} \tag{2-25}$$

where the conductive heat flux, q''_{cond} (W/m^2), is the heat transfer rate in the *x* direction per unit area perpendicular to the direction of transfer. The thermal conductivity *k* is an important material property related to heat transfer characteristics of the concrete. The process of conduction is spontaneous and irreversible, and it is related to the entropy of

the concrete. The second law of thermodynamics, the governing principle behind the distribution of entropy, is used to derive the heat conduction equation. This approach has been used to estimate the temperature distribution and the associated frost action in multi-layer pavement systems (Dempsey et al., 1986).

Convection

Heat energy is transferred from a slab surface to the surrounding environment by currents of fluid particles. In addition, this heat transfer is facilitated by random molecular motion in the fluid. In other words, convection heat transfer occurs between a flow of wind and a surface of a concrete slab when they are at different temperatures. If the temperatures between a slab surface and a wind flow differ, temperature in the fluid flow above the slab will vary from T_s at the slab surface to T_a in the flow far above the slab surface. Convection heat transfer is expressed as (Says and Crawford, 1980; Kaviany, 1994):

$$q''_{conv} = h_c\left(T_s - T_a\right) \tag{2-26}$$

where q''_{conv} (W/m^2) is the convective heat flux and h_c (W/m^2/^{o}K) is the convective heat transfer coefficient. The convective heat transfer coefficient is difficult to determine because of the many variables that affect it. An empirical formula was suggested to relate convection heat transfer coefficient to wind velocity and roughness of slab surface (Branco et al., 1992):

$$h_c = 6 + 3.7v \tag{2-27}$$

where 6 W/m^2/^{o}K represents an average slab surface roughness without wind effects. And the heat transfer coefficient increases with the increase of wind speed proportionally.

Irradiation

Irradiation transfers heat energy by electromagnetic waves, while conduction and convection require a material medium. Emissive power E (W/m^2) indicates the rate of heat energy release from a surface of a concrete slab with unit area by irradiation. The upper limit of emissive power is shown as (Incropera and DeWitt, 1996):

$$E = \varepsilon\sigma T_s^4 \tag{2-28}$$

where T_s (^oK) is the absolute temperature at the surface of a concrete slab and σ (=5.67×10^{-8} W/m^2/$^oK^4$) is the Stafan-Boltzmann constant. The term ε is the emissivity, which ranges from 0 to 1, and is a radiative property of a slab surface, and provides a measure of how efficiently the surface emits energy relative to a blackbody.

Irradiation for a concrete pavement is determined on the basis that a slab surface at temperature T_s is radiating to a much larger surface at temperature T_a surrounding the slab surface. Irradiation heat transfer can be expressed as (Siegel and Howell, 1981; Meinel and Meinel, 1976):

$$q_r'' = \varepsilon\sigma\left(T_s^4 - T_a^4\right) \tag{2-29}$$

Equation (2-20) is assumed to yield a reasonable estimate of heat exchange between a slab surface and the surrounding environment under cloudy weather conditions (Williamson, 1967; Thepchatri et al., 1977).

Solar Radiation

Solar radiation (q_s'') absorbed directly into a concrete slab surface causes the surface of the slab to be heated more rapidly than the interior region. This effect contributes to a temperature gradient through the depth of the slab (Branco et al., 1992; Hsieh et al., 1989). There are several factors that influence the solar radiation absorption into a given slab surface. These factors include the time of the day or year, the latitude, cloudiness, and so on (Chapman, 1982; Taljaston, 1987; Branco et al., 1992). The solar radiation consists of direct and indirect components. The direct component is the solar radiation that is directly incident on the surface, while indirect radiation refers to the solar radiation resulting from multiple scattering by the environment. Accordingly, the total solar radiation that reaches the surface of a concrete slab is the sum of direct and indirect contributions (Branco et al., 1992):

$$q_s'' = \alpha\left[I_d \sin\theta + I_i\left(\frac{1+\cos\gamma}{2}\right)\right] \tag{2-30}$$

where

q_s'' = solar radiation (W/m^2)

α = surface heat absorptivity of concrete (= 0.6) (Chapman, 1982)

I_d = direct solar radiation (W/m^2)

I_i = indirect solar radiation (W/m^2)

θ = incidence angle of solar radiation against the slab surface (degree)

γ = inclination angle of slab surface (degree)

The amount of solar radiation received by the slab surface depends on the incidence angle of solar radiation against the slab surface and the inclination angle of the slab surface. The incident angle of solar radiation can be determined by a method presented by Hsieh et al. (1989). The indirect solar radiation may range from 10 percent of the total solar radiation on a clear day to nearly 100 percent on a totally sunny day. No solar radiation absorption occurs at night since the sun's rays are no longer prevalent.

Boundary Conditions of Heat Transfer for Pavements

The environmental effects associated with concrete pavement construction are prevalent both at the pavement surface and at the bottom. At the pavement surface, heat transfer is affected by all the heat mechanisms previously noted. At the bottom of the concrete layer, heat transfer is affected by the capacity of the subbase to thermally conduct heat via its thermal properties. Similarly, heat transfer to the soil under the subbase is affected by conduction and is dependent on the thermal properties of soil. These two conditions are summarized as follows:

$$-k\nabla T \cdot n + q''_{conv} + q''_r - q''_s + q''_e = 0 \text{ on pavement surface} \quad (2\text{-}31)$$

$$k\nabla T \cdot n = 0 \text{ on pavement bottom} \quad (2\text{-}32)$$

where

k = thermal conductivity (W/m/^{o}C)

q''_{conv} = heat flux due to convection (W/m^2)

q''_r = heat flux due to irradiation (W/m^2)

q''_s = solar radiation absorption (W/m^2)

q''_e = heat flux due to evaporation (W/m^2)

∇ = gradient notation

n = unit direction of heat flow by vector notation

MODELING VERTICAL MOISTURE PROFILES

TMAC^2, a two-dimensional finite element method (FEM) program, predicts moisture distribution of a concrete pavement at an early age using the material properties, curing conditions, initial and boundary conditions. The finite element mesh of TMAC^2 has a total of 120 rectangular elements (5 columns × 24 rows) with 539 nodal points (9 nodal points per each element). TMAC^2 simultaneously models the moisture and temperature of a concrete pavement in specified environmental conditions. Many other capabilities such as prediction of strength, elastic modulus, and tensile creep development, and design of mixture proportion have been incorporated into the software.

Boundary Conditions

From the time of placement when a concrete is assumed to be completely wet and highly diffusive, moisture differences between ambient conditions and those inside the concrete cause moisture to move from the concrete matrix to the surrounding atmosphere. To numerically simulate this phenomenon, the humidity at the concrete surface has been assumed to be the same as the ambient humidity during its whole life (Parrot, 1988), although actual surface humidity is different from ambient humidity as noted by curing tests.

$H = 1.0$ initial condition

$H_s = aH_a + bH_c + cL$ boundary condition

Where a to c are laboratory derived coefficients and H_c is concrete humidity as predicted by TMAC^2. The linear relationship shown in Figure 2-5 was established based on a series of laboratory curing tests (Jeong and Zollinger, 2003). Surface humidity (H_s) was modeled as a function of ambient

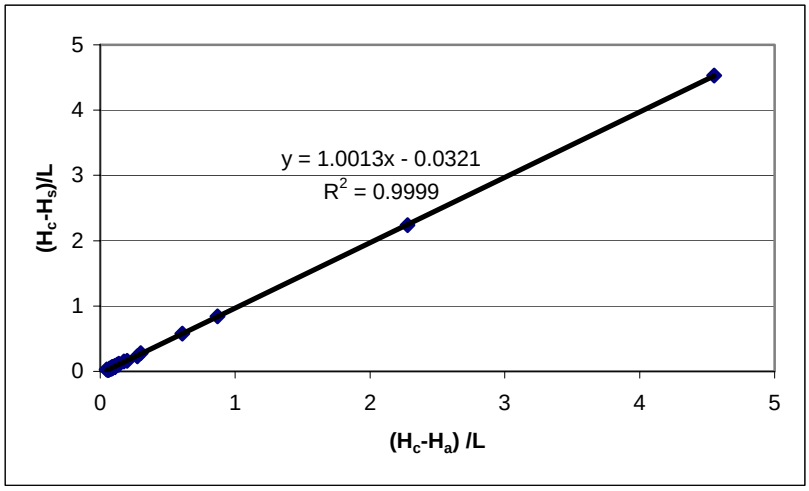

Figure 2-5 Modeling of Surface Humidity Using Curing Test Data.

humidity (H_a), concrete humidity at 1.9 cm (0.75 inch) below the top surface (H_c), and effective curing thickness (L). The effective curing thickness (L) was originally proposed by Bažant and Najjar (1972) and was used by Jeong and Zollinger (2003) to represent the effectiveness of various curing methods.

$$L = \frac{\ln \frac{H_s}{H_a}}{\frac{\partial H_s}{\partial x}}$$

Modeling of Concrete Moisture Diffusivity

Another effort for more accurate moisture distribution using TMAC^2 was modeling back-calculated moisture diffusivity by transforming the governing equation of moisture diffusion to calibrate predicted humidity (H). The governing equation of moisture diffusion is derived from Darcy's law by introducing moisture isotherm concept as (Bažant and Najjar, 1972):

$$\frac{\partial H}{\partial t} = D\frac{\partial^2 H}{\partial x^2} + \frac{\partial H_s}{\partial t} + K\frac{\partial T}{\partial t} \qquad (2\text{-}33)$$

where T is temperature and ∂H_s is change in concrete humidity due to hydration (or self-desiccation) at a constant water content and time (t), which is expressed as a function of degree of hydration (α) and experimental coefficients (a and b) (Lim, 2002).

$$\partial H_s = \frac{a+\alpha}{b} \qquad (2\text{-}34)$$

The coefficients (a and b) will vary in accordance with the factors influencing the hydration process, e.g., w/c and curing temperature. In equation (2-33), D is diffusivity (L^2/t) and K is hygrothermic coefficient representing the change in concrete humidity due to one degree change in temperature. If the dry bulb temperature, T, used in equation (2-33) is assigned a constant temperature value, the third term in the right side of the equation will become zero, simplifying equation (2-33) to:

$$\frac{\partial H}{\partial t} = D\frac{\partial^2 H}{\partial x^2} + \frac{\partial H_s}{\partial t} \qquad (2\text{-}35)$$

The form of equation (2-35) can be rearranged to isolate the moisture diffusivity as:

$$D = \frac{\frac{\partial (H - H_s)}{\partial t}}{\frac{\partial^2 H}{\partial x^2}} \qquad (2\text{-}36)$$

The values of the moisture diffusivity vary with time and position and can be back-calculated using the above expression and relative humidity data collected from either the field or laboratory. The back-calculated values of moisture diffusivity over time are used to develop a diffusivity model specific to a given concrete mixture and to more accurately predict moisture in that concrete mixture while it is hardening.

The research team conducted laboratory tests using an arrangement of relative humidity sensors to allow observation of the trends of relative humidity with time and to back-calculate the moisture diffusivity. Concrete was placed in a cylindrical PVC mold with a diameter of 20.3 cm (8 inch) and a height of 30.5 cm (12 inch). Moisture sensors were located 2.5, 7.6, and 12.7 cm (1, 3, and 5 inch) below the exposed surface. The temperature and relative humidity of the curing room were maintained at 32 °C and 50 percent, respectively, during the testing. Immediately after placement, the concrete manifests low relative humidity as noted in Figure 2-6, which appears to be due to significantly high values of moisture diffusivity in the concrete while it is in a fresh state as shown in Figure 2-6. Low vapor pressure of concrete due to high moisture diffusivity results in low initial relative humidities. On the basis of numerous results from the field and the lab, the trend of relative humidity of concrete can be categorized by three stages as shown in Figure 2-6. During the first stage (placement of concrete), the initially high relative humidity decreases rapidly due to high values of moisture diffusivity of concrete. This decrease may be caused by a condition of non-equilibrium between the vapor pressure

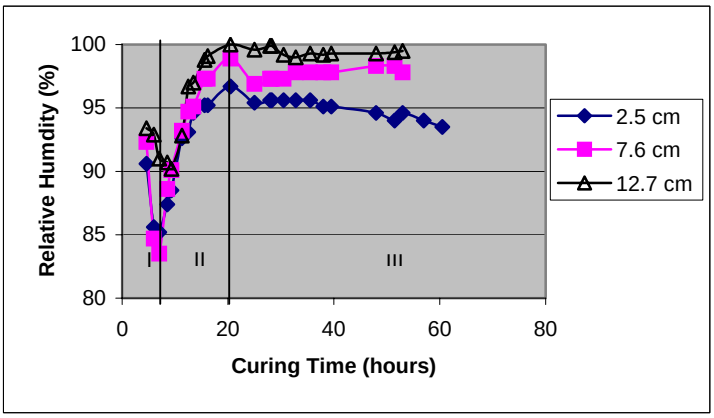

Figure 2-6 Relative Humidity History of Concrete (Laboratory Test) (Jeong and Zollinger, 2003).

inside the concrete and the surrounding atmosphere immediately after placement. The rate of evaporation during this stage may be accompanied by some bleeding. In Stage II, referred to as the bleeding stage, the relative humidity increases with time and comes to a peak as the initially high moisture diffusivity begins to decrease. The moisture diffusivity, nonetheless, is still at a comparatively high level, so the evaporation rate is still at a comparatively high rate. During the third stage (referred to as post bleeding), relative humidity decreases with time and is equilibrated to ambient relative humidity due to reduced moisture diffusivity of the concrete. The duration of each stage depends upon the prevalent curing conditions and water content of the concrete mixture.

Using the concrete humidity (adjusted for self-desiccation), moisture diffusivities were back-calculated by equation (2-36) as shown in Figure 2-7. Significiant changes occurred in back-calculated moisture diffusivity during the early stages of hardening. The diffusivities were significantly high initially, but diminished quickly as expected since D diminishes as a function of the concrete age. Previous research (Bažant and Najjar, 1972; Parrott, 1991; Xi et al., 1994) also has indicated that the moisture diffusivity has been found to be a function of humidity and paste porosity. Thus, it is reasonable that moisture diffusivity (D) is assumed to vary with temperature (T), humidity (H), and degree of hydration (α) in concrete on the basis of the test results as:

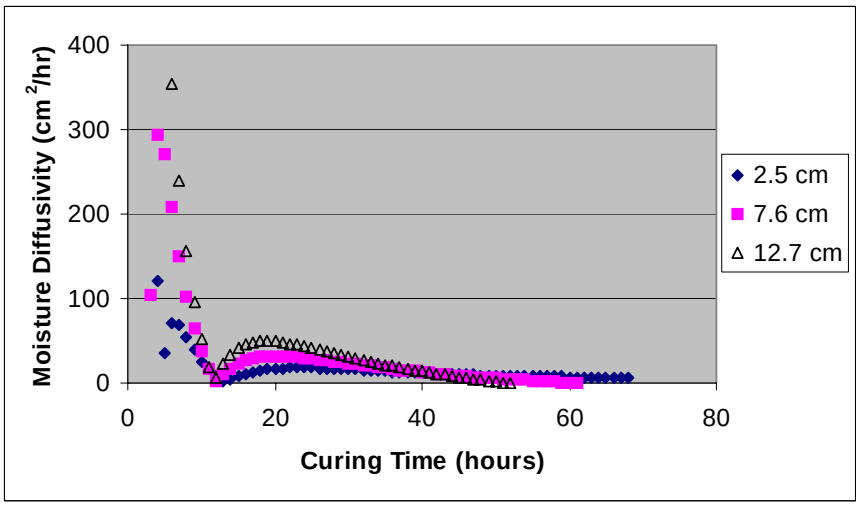

Figure 2-7 Back-Calculated Moisture Diffusivity.

$$D = \frac{a}{\alpha}\left(-\ln\frac{1}{T}\right)^{H} + b \qquad (2\text{-}37)$$

where a and b are laboratory derived coefficients. The moisture diffusivity predicted by equation (2-37) corresponds with the back-calculated moisture diffusivity with 0.84 of R-square value as shown in Figure 2-8. Relative humidity of the concrete specimen was forward-calculated (Figure 2-9) using the moisture diffusivity model (equation (2-33)) and the

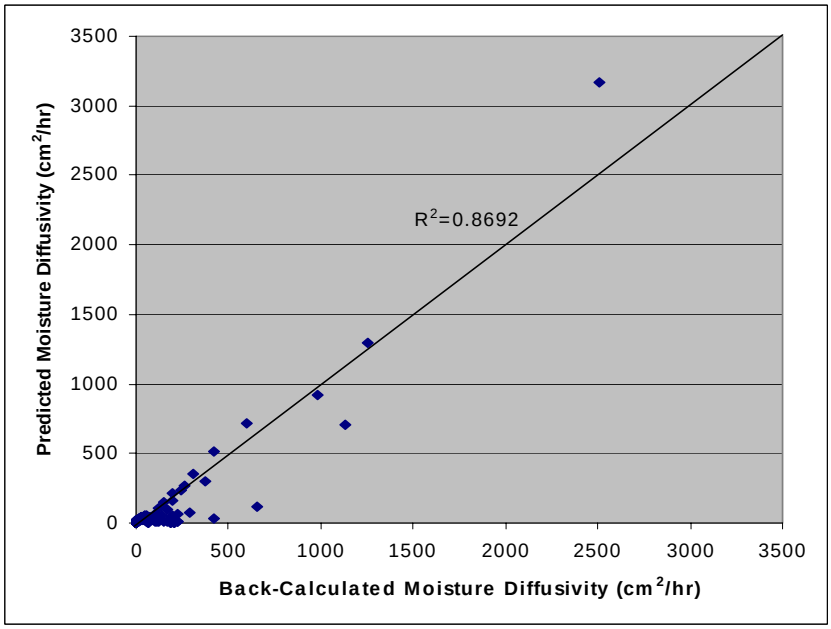

Figure 2-8 Back-Calculated versus Predicted Moisture Diffusivity.

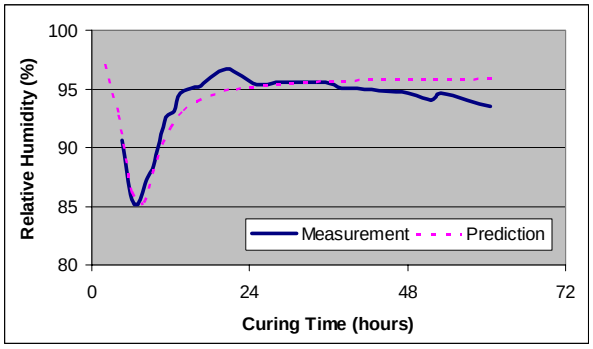

(a) 2.5 cm (1 inch) from Top Surface

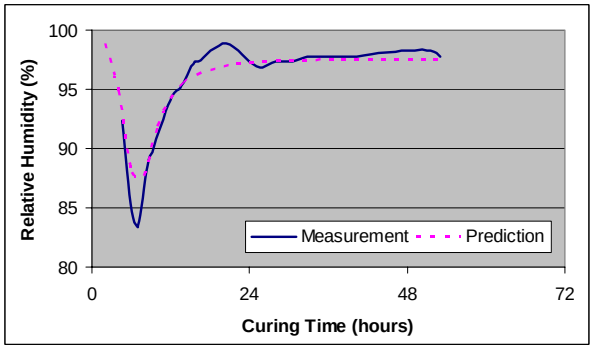

(b) 7.6 cm (3 inch) from Top Surface

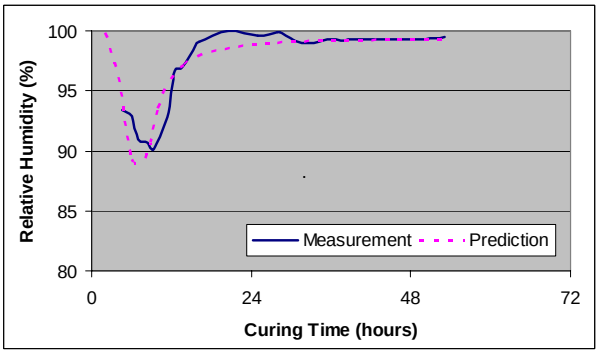

(c) 12.7 cm (5 inch) from Top Surface

Figure 2-9 Comparisons between Measured and Predicted Relative Humidity of Concrete Specimen.

initial and the previously noted boundary conditions (as shown in Figure 2-9). Significantly large changes in relative humidity initially were predicted using the high back-calculated moisture diffusivities. The predictability of TMAC[2] to simulate the moisture distribution of the concrete improved after the measured relative humidity reached a maximum value.

Field Validation

A 30.5 cm (12 inch) thick test slab was constructed at the Riverside Campus Annex test facility of the Texas A&M University located in Bryan, Texas (Jeong and Zollinger, 2003). Relative humidity of the test slab was predicted using the back-calculated moisture diffusivity model based on ambient humidity and initial and boundary conditions. The high back-calculated moisture diffusivity and low ambient relative humidity initially caused a significant decrease in the relative humidity of the slab up to a few hours after placement. The comparison is shown in Figure 2-10.

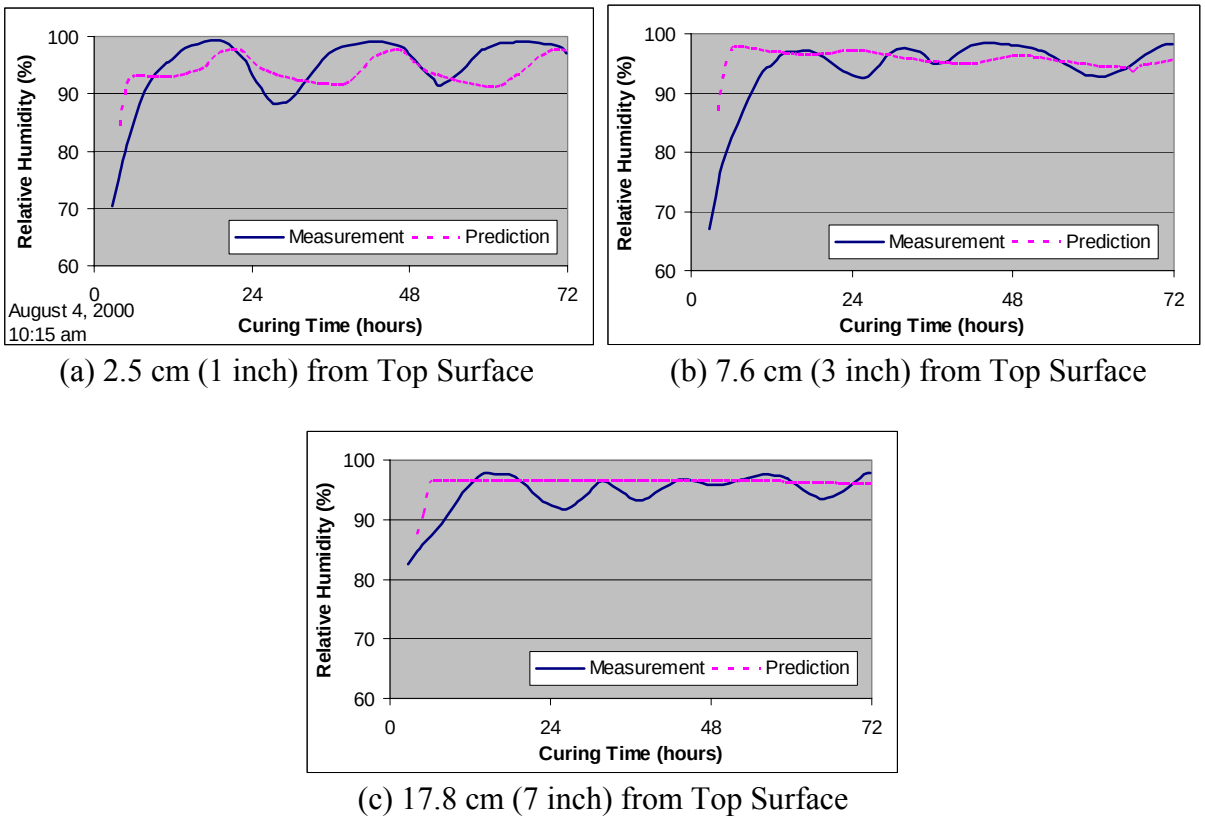

(a) 2.5 cm (1 inch) from Top Surface

(b) 7.6 cm (3 inch) from Top Surface

(c) 17.8 cm (7 inch) from Top Surface

Figure 2-10 Comparison between Measured and Predicted Relative Humidity of Field Test Slab.

MODELING VERTICAL TEMPERATURE PROFILES

Temperature distributions of the concrete pavement are estimated by analyzing the transient heat transfer between the concrete and the surrounding condition as represented by the boundary value equations where the effects of environmental factors such as air temperature, wind velocity, solar radiation, and heat of vaporization are accounted for. The heat of hydration also must be considered to accurately estimate temperature distributions of the early-age concrete pavement. The hydration process generates internal heat, which influences the rate of chemical reactions of the cementitious materials and water while the environmental conditions influence concrete temperature and moisture conditions at the surface.

Governing Equation of Heat Transfer

The governing equation of heat transfer for temperature prediction in an early-age concrete pavement taking heat of hydration and ambient temperature conditions into account is (Klemens, 1969; Incropera and DeWitt, 1996):

$$\frac{\partial}{\partial x}\left(k_x \frac{\partial T}{\partial x}\right)+\frac{\partial}{\partial y}\left(k_y \frac{\partial T}{\partial y}\right)+Q_h = \rho c_p \frac{\partial T}{\partial t} \qquad (2\text{-}38)$$

where

T = concrete temperature (^{o}C)

t = time (hours)

x, y = coordinates in concrete pavement (m)

k_x, k_y = thermal conductivities of concrete (W/m/^{o}C)

Q_h = heat of hydration (W/m^3)

ρ = concrete density (kg/m^3)

c_p = specific heat of concrete (J/kg/^{o}C)

Density (ρ) and specific heat (c_p) of concrete in equation (2-38) are basic material properties determined by laboratory and ASTM test procedures that are not elaborated here. The heat of hydration of concrete (Q_h) in equation (2-38) is the amount of heat that is released into the surroundings of the concrete pavement due to the hydration process. The heat of the hydration is mathematically defined as (Wang and Zollinger, 2000):

$$Q_h = H_u C \alpha \frac{\lambda_1 \kappa_1}{t_1} \frac{[\ln(\tau)]^{-(1+\kappa_1)}}{\tau} \cdot \exp\left[-\frac{E}{R}\left(\frac{1}{T+273} - \frac{1}{T_r+273}\right)\right] \qquad (2\text{-}39)$$

where

H_u = total heat of hydration (J/g)

C = cement content (g/cm^2)

λ_1, κ_1, t_1 = hydration shape and time parameters

τ = age parameter $= 1 + \frac{t_e}{t_1}$

t_e = equivalent age

α = degree of hydration

E = activation energy (J/mol)

R = universal gas constant (= 8.3144 J/mol/^{o}C)

T_r = reference temperature (= 20 ^{o}C)

The equivalent age (t_e) is predicted by the Arrhenius maturity theory and then is used in the calculation of degree of hydration of concrete as (Bažant and Najjar, 1972; Emborg, 1989):

$$t_e = \sum_{t=0}^{age} \beta_T \beta_H \Delta t$$

$$\alpha = \exp\left[-\lambda_1 (\ln \tau)^{-\kappa_1}\right]$$

where

β_T = temperature correction factor

$$= \exp\left[-\frac{E}{R}\left(\frac{1}{T+273} - \frac{1}{T_r+273}\right)\right]$$

β_H = moisture correction factor, which is assumed to be 1.0 in this project

$$= \frac{1}{1+(7.5-7.5H)^4}$$

H = humidity of concrete

Heat Flux Due to Evaporation

Including heat flux due to evaporation in the boundary condition of heat transfer at the slab top surface is important to accurately predict the temperature of concrete pavement. So far, only few temperature prediction models have considered the evaporation effects in their boundary conditions (Kapila et al., 1997). There have been many efforts to develop concrete temperature prediction models that can be easily used although they ignore the effect of heat flux due to evaporation in their boundary conditions (Yang, 1996; Ruiz et al., 2001). Heat flux due to evaporation can be calculated by:

$$q_e'' = EH_v$$

where

E = rate of evaporation (kg/m^2/hr or W/m^3)

H_v = heat of vaporization of water

= $597.3 - 0.564T_s$ (cal/g) (Linsley et al., 1975)

= $427(597.3 - 0.564T_s)$ (m)

Because none of the existing evaporation models did consider the drying characteristics of concrete, a modified version of the Penman's evaporation model was prescribed as (Jeong and Zollinger, 2003):

$$E = \delta \frac{q_s''}{H_v} + J \qquad (2\text{-}40)$$

where

δ = calibration factor for moisture condition of concrete surface

J = rate of evaporation from concrete due to convective heat transfer, irradiation, and aerodynamic effects (kg/m^2/hr)

The rate of evaporation under laboratory curing conditions (i.e., non-solar effects) shown in equation (2-40) is expressed by a model proposed by Bazant and Najjar (1972) as:

$$J = B \ln \frac{H_s}{H_a} \qquad (2\text{-}41)$$

where

B = surface moisture emissivity (kg/m^2/hr)

H_s = concrete surface humidity

H_a = ambient humidity

The surface moisture emissivity was formulized as functions of effective curing thickness (L), laboratory derived coefficients (a - f), and wind speed (v) during and after bleeding, respectively (Jeong and Zollinger, 2003):

$$B = a + b\exp(-L) + cv^2 \qquad \text{during bleeding} \qquad (2\text{-}42)$$

$$B = d + \frac{e\ln L}{L} + fv^{2.5} \qquad \text{after bleeding} \qquad (2\text{-}43)$$

where the unit of surface moisture emissivity is kg/m^2/hr, effective curing thickness is cm, and wind speed is m/s.

As explained through the above equations, solar radiation, wind speed, ambient humidity, and concrete humidity at both the surface and 1.9 cm (0.75 inch) below the top surface are required to calculate the heat flux due to evaporation. Among those, solar radiation, wind speed, and ambient humidity can be predicted by a database of a local weather station where the pavement is constructed. Concrete humidity can be predicted by the humidity module of TMAC^2, which uses surface humidity as its boundary condition. Surface humidity has been assumed to be equivalent to the ambient humidity to simplify the moisture boundary condition at the top surface (Parrott, 1988; Parrott, 1991). However, it is noted that the concrete surface humidity is not the same as the ambient humidity due to such factors as the presence of a curing compound (Jeong and Zollinger, 2003). Consequently, surface humidity was represented as a function of ambient humidity (H_a), concrete humidity at 1.9 cm (0.75 inch) below top surface (H_c), and effective curing thickness (L) (Figure 2-5) to account for the effect of a curing compound based on a relationship derived from laboratory curing test results (Jeong and Zollinger, 2003).

Validation of Thermal FEM Analysis

To calculate heat of hydration of the test slab, parameters of equation (2-39) such as total heat of hydration, activation energy, and hydration shape and time parameters were found from laboratory tests. A super-insulated steel Qdrum semi-adiabatic

calorimeter was used to calculate total heat of hydration of the test slab. The calorimeter measures the heat energy accumulated in the concrete due to heat of hydration and the heat flow through the super-insulated wall of the calorimeter. Concrete was placed in a 15.2 × 30.5 cm (6 × 12 inch) plastic cylinder mold. This specimen was put inside the calorimeter with a tightly sealed and insulated lid. Data collected from a datalogger connected to the calorimeter indicated 385 J/g of total heat of hydration from the concrete specimen.

Activation energy was determined in accordance with ASTM C 1074 (1999) using mortar cube specimens. Mortar was placed in brass cubic molds with 5.1 cm (2 inch) sides, and the specimens were submerged into temperature-controlled water baths at 12, 25, and 35 °C, respectively. The specimens were demolded immediately before the compressive strength test was performed at 3, 7, 14, and 28 days using a universal hydraulic testing machine. Ultimate compressive strengths for each curing temperature were estimated by interceptions of best-fit straight lines of reciprocal of average cube strength versus reciprocal of age as shown in Figure 2-11. Activation energy of 31.4 kJ/mol was determined by the slope of best-fit straight line of the natural logarithm of the reciprocal of age versus the reciprocal of absolute curing temperature as shown in Figure 2-12. The slope of the line is the value of activation energy divided by the gas constant (8.3144 J/mol/°K).

To get the shape and time parameters λ_1, κ_1, and t_1 shown in equations related to equation (2-39), compressive strength tests of the 10.2 × 20.3 cm (4 × 8 inch) standard cylinder specimens were made at 1, 3,

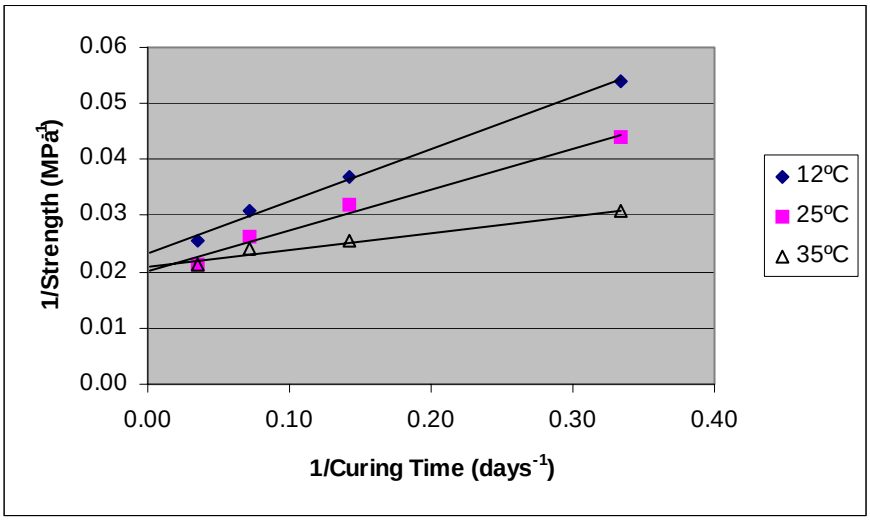

Figure 2-11 Reciprocal of Mortar Cube Strength versus Reciprocal of Age.

7, and 14 days after placement. The parameters were determined by the relative strengths (degree of hydration) and maturity of the specimens using least square linear regression analysis. The values of the parameters

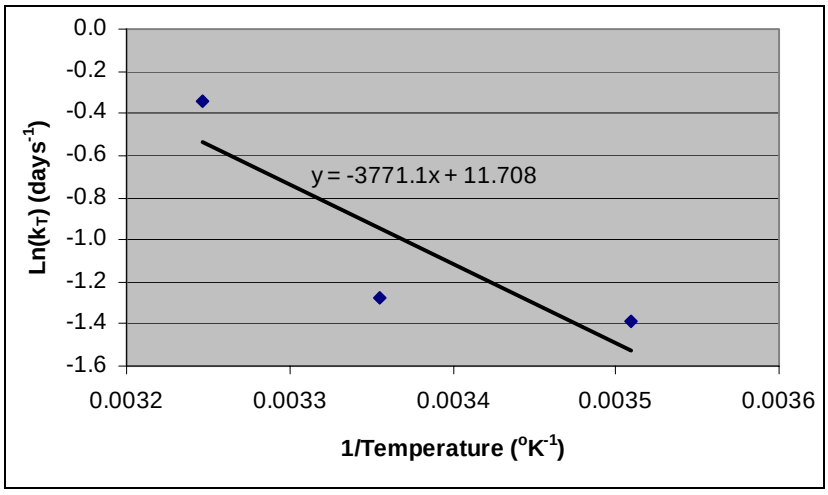

Figure 2-12 Logarithm of Reciprocal of Rate Constant of Mortar Cube versus Reciprocal of Curing Temperature.

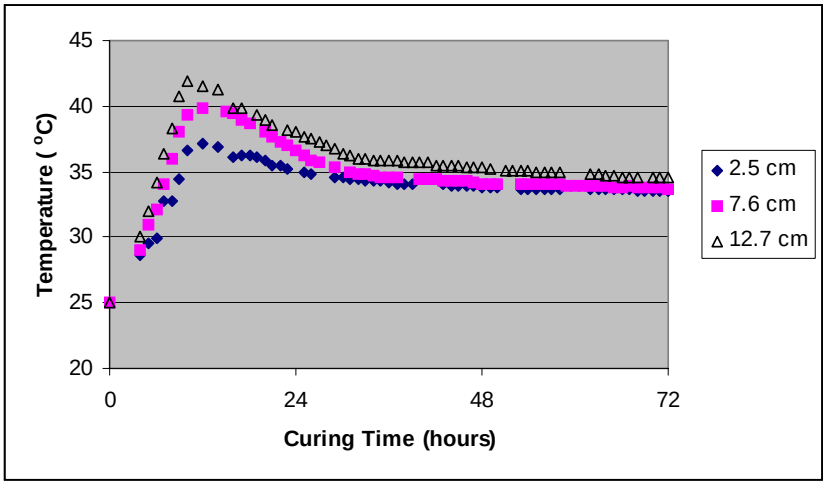

(a) Temperature

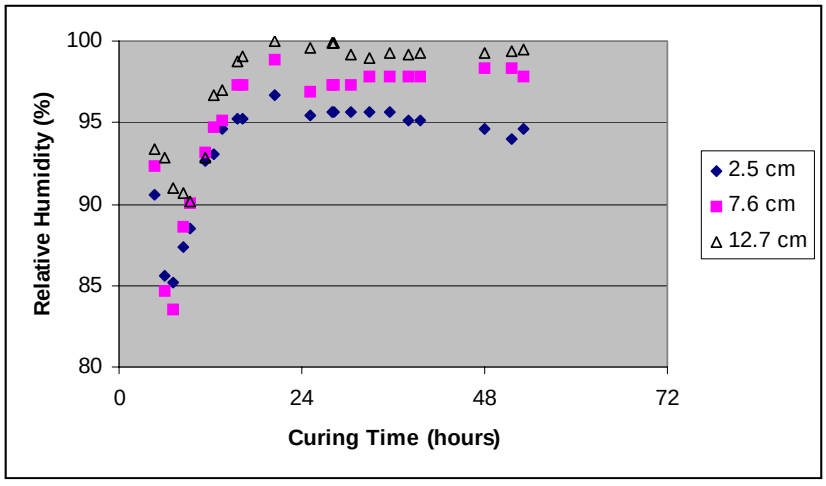

(b) Relative Humidity

Figure 2-13 Measured Concrete Temperature and Moisture (Laboratory).

for the mix proportion used in the test slab were found to be 0.69, 1.52, and 13, respectively. The curve of the degree of hydration (α) with equivalent age (t_e) is shown in Figure 2-12.

Back-Calculation and Model Calibration

Thermal conductivity is a parameter that dominates the heat movements in concrete pavement (Figure 2-13). For better

prediction of temperature in hardening concrete, the thermal conductivity back-calculated from the governing equation of heat transfer (equation (2-38)) as:

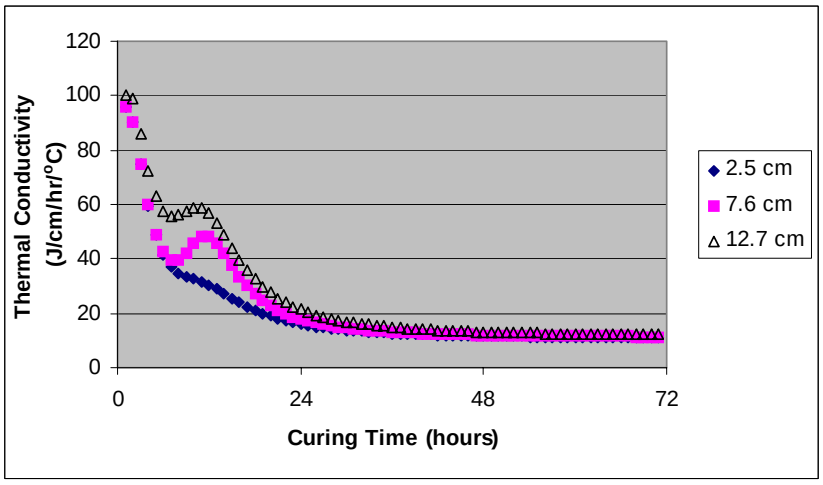

Figure 2-14 Back-Calculated Thermal Conductivity.

$$k = \frac{\rho c_p \dfrac{\partial T}{\partial t} - Q_h}{\dfrac{\partial^2 T}{\partial x^2}} \qquad (2\text{-}44)$$

The back-calculated values (Figures 2-14 and 2-15) are expected to yield valid estimates of thermal conductivity over time and to more accurately predict temperature in hardening concrete. The temperature and moisture profiles of a concrete cylinder (Figure 2-13) with a 20.3 cm (8 inch) diameter and 30.5 cm (12 inch) height were characterized in the laboratory by using third degree

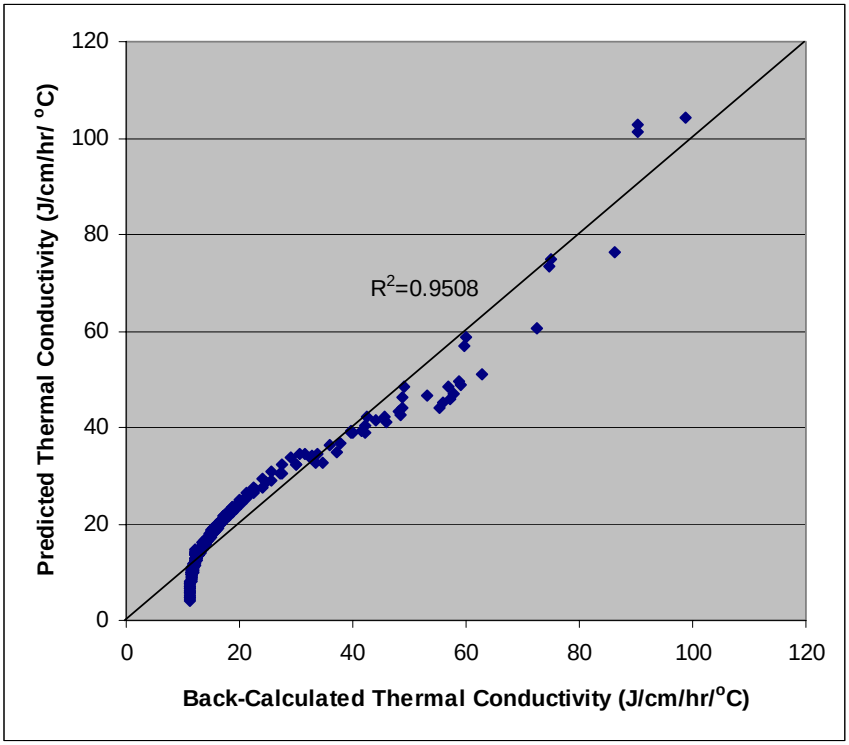

Figure 2-15 Back-Calculated versus Predicted Thermal Conductivity.

polynomial fits based on the data measured at 2.5, 7.6, and 12.7 (1, 3, and 5 inch). Temperature and moisture at 27.9 cm (11 inch) were assumed to be the same as those measured at 12.7 cm (5 inch) to form the polynomial fits. The polynomial fits allowed for interpolation or extrapolation of the temperature and moisture for time steps and positions other than those where measurements were made. Using the concrete temperature profile functions, thermal conductivities were back-calculated by equation (2-44). As shown in Figure 2-14, the deeper the measurement point from the slab top surface, the slightly higher the thermal conductivity is.

Thermal conductivity generally has been considered to be a function of moisture content in concrete or a linear function of the degree of hydration (Hsieh et al., 1989; Trinhztfy et al., 1982). The back-calculated thermal conductivity varied with temperature in addition to moisture and degree of hydration. Therefore, the back-calculated thermal conductivity (k) was modeled as a function of temperature (T), humidity (H), and degree of hydration (α) of concrete as:

$$k = a \ln\left[\frac{1}{\alpha}\left(-\ln\frac{1}{T}\right)^{H}\right] + b \qquad (2\text{-}45)$$

where a and b are laboratory derived coefficients. The thermal conductivity predicted by equation (2-45) corresponds with the back-calculated thermal conductivity (equation (2-44)) with high R-square value as shown in Figure 2-15.

Model Validation

Temperature of the test slab was forward-calculated using the thermal conductivity model, other material properties, and initial and boundary conditions. Input parameters to simulate the temperature of the test slab are summarized in Table 2.1. Effective curing thickness of the test slab (L) and humidity data decrease with curing time as shown in Figure 2-16.

Table 2-1 Summary of Input Parameters.

Parameters	Values
Initial Temperature, T_0 (^{o}C)	29.8
Density, ρ (g/cm^3)	2.286
Specific Heat, c_p (J/g/^{o}C)	1.044
Absorptivity, α_s	0.5
Emissivity, ε	0.9
Total Heat, H_u (J/g)	385
Cement Content, C (g/cm^3)	0.289
Activation Energy, E (kJ/mol)	31.4
Parameter, λ_1	0.69
Parameter, κ_1	1.52
Parameter, t_1	13

To consider heat loss due to evaporation in the boundary condition at the slab top surface, rate of evaporation of the test slab was calculated and the data collected from the test slab (Jeong and Zollinger, 2003). The variation of the evaporation rate shown in Figure 2-17 indicates that a substantial amount of evaporation occurred in the afternoon of the day of slab placement due to weather conditions and then decreased considerably the next day. The rate of evaporation also cycled between a maximum in the afternoon and minimum in the morning. Condensation and moisture absorption on the slab surface occurs in the morning when the ambient temperature falls below the dew point temperature. The absorbed surface moisture evaporated in the afternoon elevating the rate of evaporation than in the morning. Figure 2-18 shows the effects of the heat flux due to evaporation on the predicted results. It is clear that the temperature profiles predicted by TMAC[2] correspond to the temperature profiles measured in the field reasonably well, as shown in Figure 2-18. The predicted profiles can be transmitted easily to analytical software for stress and deformation evaluation.

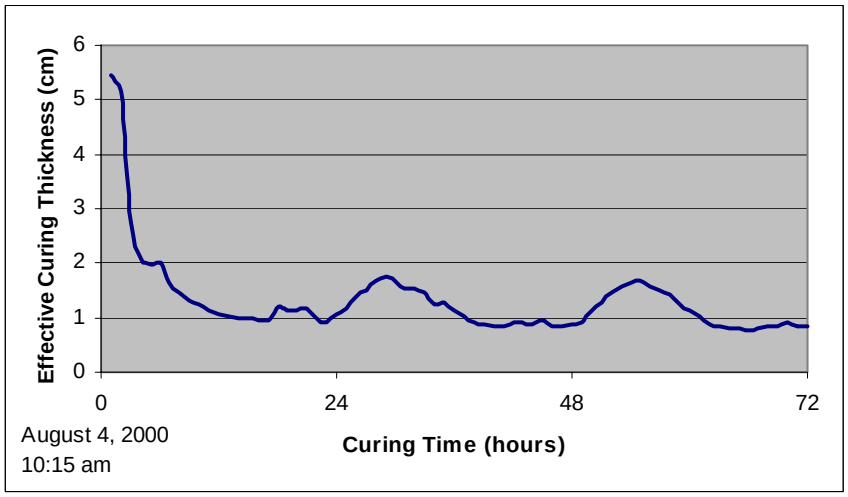

Figure 2-16 Predicted Effective Curing Thickness of Test Slab.

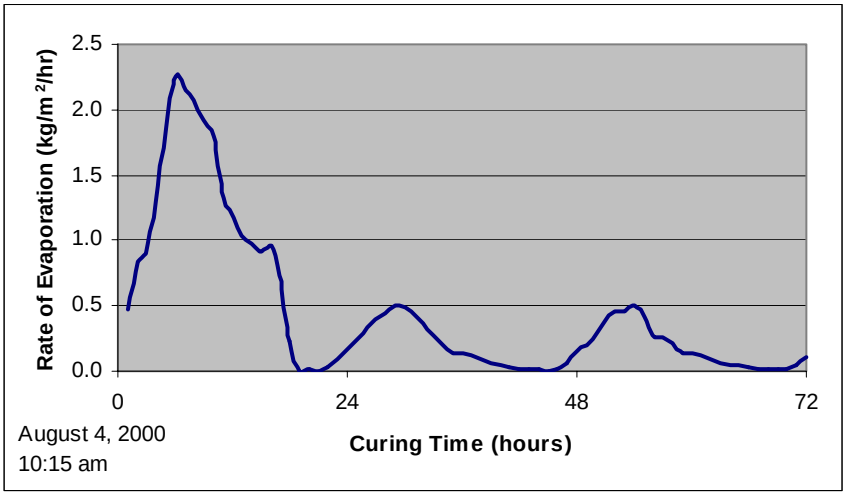

Figure 2-17 Predicted Rate of Evaporation from Test Slab.

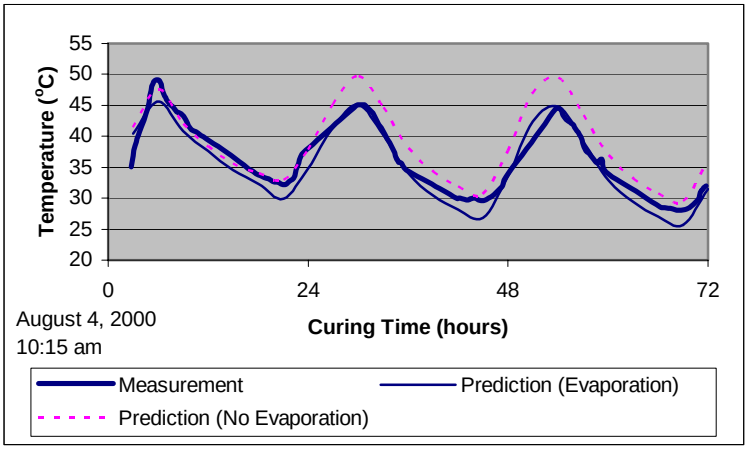

(a) 2.5 cm (1 inch) from Top

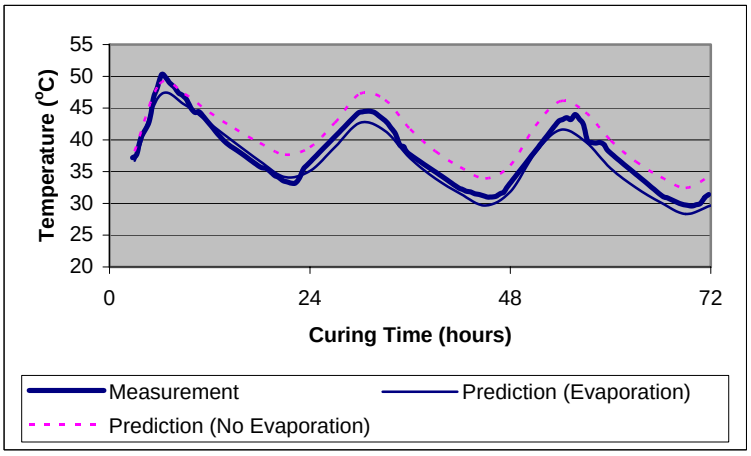

(b) 7.6 cm (3 inch) from Top

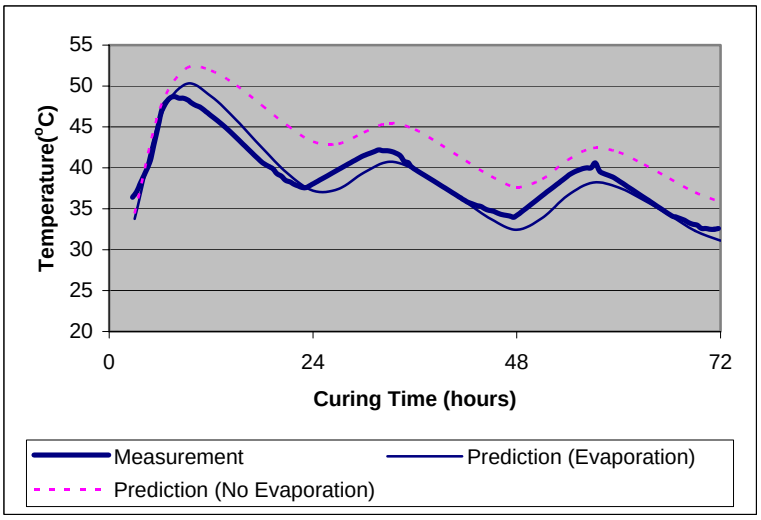

(c) 17.8 cm (7 inch) from Top

Figure 2-18 Measured versus Predicted Temperature Histories of Test Slab.

CHAPTER 3
MOISTURE-RELATED STRENGTH FACTORS IN CONCRETE PAVEMENTS

INTRODUCTION

Protective curing of newly placed concrete is typically carried out until the concrete strength reaches a minimum required strength. The capability to accurately predict the minimum time necessary to cure hydrating concrete is a valuable tool in the management of concrete construction scheduling, especially in fast-track construction. Typically, destructive strength testing has been the only method used to accurately ascertain if the cure time has been adequate. However, the amount of time to prepare and manage the test specimens sometimes presents coordination difficulties for highway agencies. Therefore, non-destructive test methods that use a minimum number of test specimens should benefit and streamline coordination of quality control measures.

Maturity, a parameter related to the temperature and time of curing, has been used as a non-destructive test parameter relative to concrete strength gain. Maturity is a parameter that maintains some proportion to time and temperature of the concrete aging process and traditionally is calculated from measured concrete temperatures. The relationship between concrete strength and maturity can be used simply to estimate in-place strength. Several different mathematical models (Chin, 1972; Freiesleben Hansen and Pedersen, 1977; Lew and Reichard, 1978; Nykanen, 1956; Pane and Hansen, 2002; Plowman, 1956) have been developed to represent the strength-maturity relationships. The strength-maturity relationship of concrete depends upon the mixture proportions and concrete curing temperature during strength gain. Incidentally, it has been found that a strength-maturity relationship developed under a given temperature condition cannot be used for any other temperature conditions unless a temperature-independent is used. Such an approach can be used at different temperature conditions, as long as the mix proportions remain unchanged. Moreover, this approach can be used in the field where the curing conditions are typically different from those where the maturity-strength relationship was developed to evaluate the in-place concrete strength.

Concrete hardens with an increase of hydration products formed mainly by reaction between water and cement. Evaporation during the hydration should be held to a minimum to facilitate strength gain. Powers (1947) suggested that hydration stops when the relative humidity inside the concrete decreases to 80 percent. Thus, appropriate moisture retention in concrete during its early stage is important to obtain a high degree of curing. Because the strength of concrete is significantly influenced by the moisture within the concrete, existing maturity concepts should be modified to consider the effect of moisture. Other factors affecting the strength on concrete considered in this study are reported in Appendix D.

MATURITY CALCULATED BY TEMPERATURE AND TIME

In order to investigate how a temperature-independent strength-maturity model can be developed from laboratory test specimens, eight beam specimens (2 sets) with the size of 15.2 × 15.2 × 50.8 cm (6 × 6 × 20 inch) were prepared and cured in chambers with temperatures of 16 °C and 29 °C and relative humidity of 70 percent for each of the specimens. The mix proportions used for laboratory tests are shown in Table 3-1. The materials and the water were placed in the chambers 24 hours prior to mixing in order to bring their temperature levels to a constant temperature. After placement, thermocouples for temperature and maturity measurements were placed 7.6 cm (3 inch) into the wet concrete at the ends. The maturity values were calculated by using the Nurse-Saul equation with a datum temperature value of -10 ºC as below (Saul, 1951).

Table 3-1 Mix Proportions in 1 m^3 (35.3 ft^3) of Beam Specimen Concrete.

Materials	Proportions
Coarse Aggregate (Limestone)	1076 kg (2372 lb)
Fine Aggregate	749 kg (1651 lb)
Cement (Type I)	397 kg (875 lb)
Water	127 kg (280 kg)
Water/Cement Ratio	0.32
Air Entrainment (Paveair 90)	0.1 liters (3.3 oz-US)
Water Reducer (Pozzolith 300 N)	0.3 liters (10.0 oz-US)
Superplasticizer (Reobilt 1000)	3.0 liters (99.8 oz-US)
Concrete Unit Weight	2353 kg/m^3 (147 lb/ft^3)

$$M = \sum_{0}^{t} (T - T_0) \cdot \Delta t \qquad (3\text{-}1)$$

where

M = maturity at age t (°C-hrs)

T = average temperature of the concrete during time interval Δt (°C)

T_0 = datum temperature (°C)

The beam specimens cured in the environmental chambers were tested at various times during the 48-hour curing period. Strength tests followed TxDOT procedure Tex-420-A (single point loading test) using a hydraulic loading device. Both the maturity and the strength values were recorded at the same points in time.

Determination of Ultimate Strength

Since the curing temperatures were different for each set of specimens, the ultimate strengths were expected to be different from each other. Strength and maturity data were analyzed by the reciprocal method (Figure 3-1) to find the ultimate strength of the concrete. Carino (1982) proposed the reciprocal method which included an offset maturity, M_0 (McIntosh, 1949), in the original reciprocal formulation developed by Kee (1971).

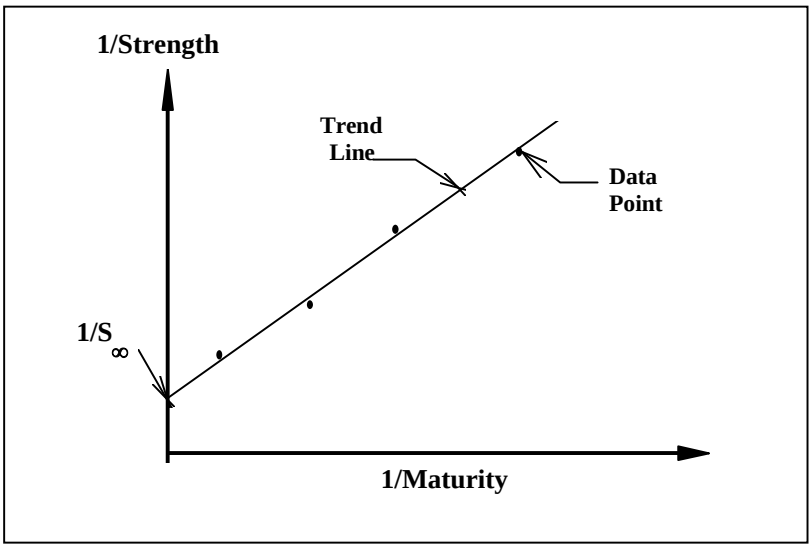

Figure 3-1 Reciprocal Method.

$$\frac{1}{S} = \frac{1}{S_\infty} + \frac{1}{A} \cdot \frac{1}{(M - M_0)} \qquad (3\text{-}2)$$

The offset maturity accounts for the fact that the strength of concrete does not begin to develop until a certain amount of maturity is reached. As seen from equation (3-2), there is a linear relationship between the reciprocal of strength and the reciprocal of maturity. This equation indicates that the intercept value is the reciprocal of the ultimate strength. Figure 3-2 presents the reciprocals of strength against the reciprocals of maturity when the offset

maturity values are zero. Trend lines were plotted among the data points for each set of the beam specimens by using the least squares linear regression method. Ultimate bending strength was predicted as 9.42 MPa (1366 psi) for the 16 °C specimens. The interception of the trend line for 29 °C specimens and the y-axis shown in Figure 3-2 was negative, which suggests that the offset maturity is non-zero in this case.

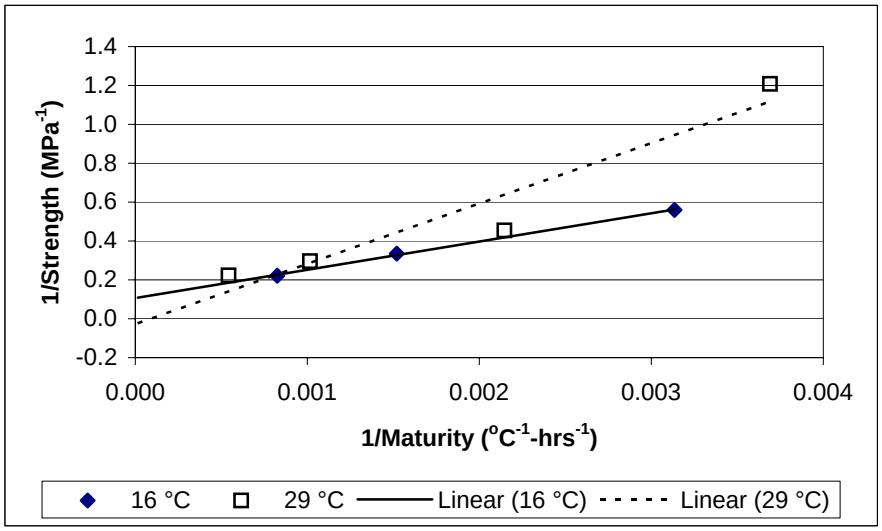

Figure 3-2 Determination of Ultimate Bending Strength by Reciprocal Method.

Using linear regression analysis, the value of M_0 was determined to be 180 ºC-hrs. Maturity of the concrete was modified by subtracting the M_0 from the original values. The modified reciprocal method for the 29° C data is displayed in Figure 3-3. Ultimate bending strength was predicted to be 6.31 MPa (915 psi) for the concrete specimens cured in the 29 °C chamber. However, more reasonable ultimate strength values can be obtained by using equation (3-3) suggested

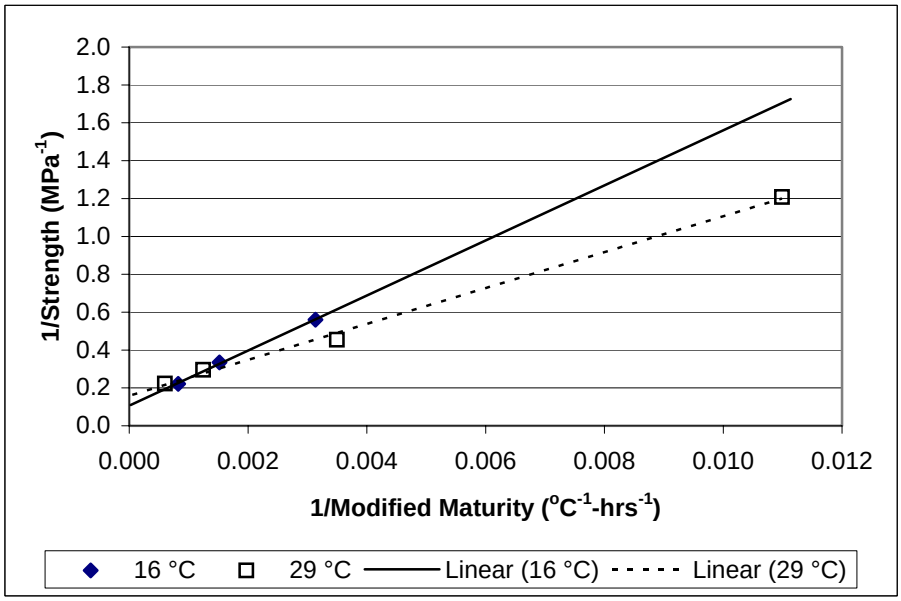

Figure 3-3 Modified Reciprocal Method.

by Freiesleben Hansen and Pedersen (1977) when the M_0 value is non-zero. Kaleidagraph (1996) or other similar tools can be used to find the parameters of this strength-maturity model which is also temperature-independent.

$$S = S_\infty e^{-\left[\frac{\tau}{M}\right]^a} \tag{3-3}$$

where τ is the characteristic time constant, and a is the shape parameter. The regression analysis for the model yielded ultimate bending strength values of 6.58 MPa (955 psi) and 5.63 MPa (816 psi) for specimens cured in the 16 °C and 29 °C chambers, respectively. The ultimate bending strength of specimens cured at 16 °C were higher than that of the specimens cured at 29 °C.

Temperature-Independent Strength-Maturity Relationship

Equation (3-3) can be transformed into a linear form, as follows:

$$\frac{S}{S_\infty} = e^{-\left(\frac{\tau}{M}\right)^a}$$

$$Ln\left(\frac{S}{S_\infty}\right) = -\left(\frac{\tau}{M}\right)^a$$

$$Ln\left(-Ln\left(\frac{S}{S_\infty}\right)\right) = aLn\left(\frac{\tau}{M}\right)$$

$$Ln\left(-Ln\left(\frac{S}{S_\infty}\right)\right) = a\left(Ln\tau - LnM\right)$$

$$Ln\left(-Ln\left(\frac{S}{S_\infty}\right)\right) = aLn\tau - aLnM \tag{3-4}$$

Equation (3-4) reveals that there is a linear relationship between the double natural logarithm of the relative strength (degree of hydration) and the natural logarithm of the maturity. When ultimate strength is calculated, this relationship can be used in prediction of the concrete strength at a construction site where maturity is measured.

The linear relationship between the double logarithm of the relative strength values and the logarithm of the maturity for all tested specimens is presented in Figure 3-4. The linear regression analysis for the combined data points yielded very high values of

R-square. This conclusion supports the hypothesis that the logarithmic relationship between the relative strength and the maturity is independent of curing temperature and unique for the same mix proportions.

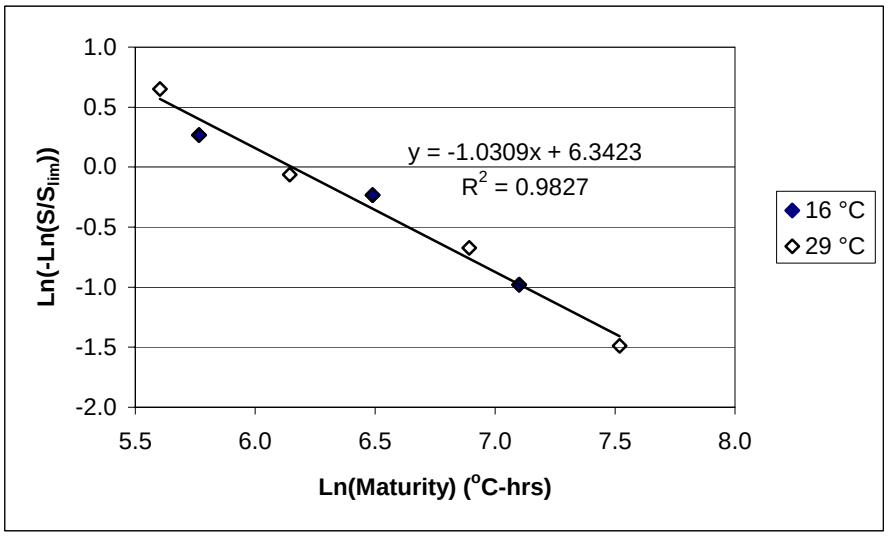

Figure 3-4 Logarithmic Relationship between Relative Strength and Maturity for All Beam Specimens.

MOISTURE-MODIFIED MATURITY

Moisture condition influences strength development of concrete because hydration involves a reaction between water and cement. Thus, the strength of concrete can be variable with respect to different moisture levels within the concrete even for the same mix proportions. Therefore, moisture should be incorporated into the temperature-based maturity concept presented previously to better predict the strength gain of concrete.

Laboratory Investigation of Moisture Effect

A laboratory test program was carried out to investigate moisture-modified maturity of concrete. Concrete was formed in a cylinder mold (Figure 3.5) that had a diameter and height of 30.5 cm (12 inch). The mold consisted of 1.3 cm (0.5 inch) thick PVC wall and an end plate. The mold insulated the concrete against lateral drying, effectively causing one-dimensional moisture movement through the top surface. Before placing the concrete, maturity sensors were placed inside the mold 2.5, 7.6, and 17.8 cm (1, 3, and 7 inch) from the top as shown in Figure 3-5 using brass casings threaded into the wall of the mold in which to support the sensors. Vibrating wire strain gauges also were included in the instrumentation, but the strain related results are not presented in this report.

Concrete placed in the mold was compacted according to ASTM C 192 (1999). According to the mix proportions shown in Table 3-2, a water cement ratio of 0.32 was used and the unit weight of concrete was determined by ASTM C 29 (1999) and was found to be 2439 kg/m^3 (152 lb/ft^3). Immediately after the placement, the specimen was moved to an environmental chamber set at 60 ^{o}C and 15 percent relative humidity.

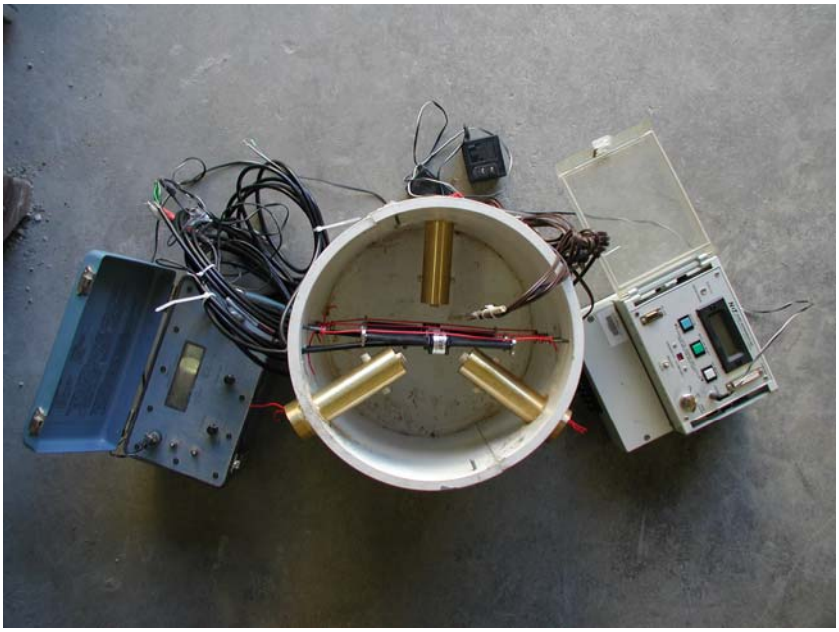

Figure 3-5 Instrumented 30.5 × 30.5 cm PVC Cylinder Mold.

Three and an half hours after placement, three temperature and moisture monitoring sensors manufactured by ATEK (Figure 3.6) were placed at the previously noted positions to measure temperature and relative humidity of the concrete. The relative humidity sensors operate on chilled mirror technology, which measures the dry bulb and the dew point temperature from inside brass casings. Access holes in the casings allowed the vapor pressure of the concrete to equilibrate inside the casings. Conventional maturity of the concrete specimen also was measured by a maturity meter.

Table 3-2 Mix Proportions in 1 m^3 (35.3 ft^3) of Cylinder Specimen Concrete.

Materials	Proportions
Coarse Aggregate (Sandstone)	1076 kg (2372 lb)
Fine Aggregate	869 kg (1916 lb)
Cement (Type I)	281 kg (618 lb)
Fly Ash (Type C)	120 (264 lb)
Water	90 kg (198 lb)
Water/Cement Ratio	0.32
Superplastisizer (Reobilt 1000)	2.7 liters (92.7 oz-US)
Concrete Unit Weight	2439 kg/m^3 (152 lb/ft^3)

Concrete strength also was determined at 2.5, 7.6, and 17.8 cm (1, 3, and 7 inch) from the top surface using standard 15.2 × 30.5 cm (6 × 12 inch) cylinder specimens. The specimens also were cured in the 60 ^{o}C and 15 percent relative humidity chamber similar to the 30.5 × 30.5 cm (12 × 12 inch) cylinder specimen. As

shown in Figure 3-6, temperature also was recorded by thermometers to correlate to the maturity of the 30.5 × 30.5 cm (12 × 12 inch) cylinder specimen. The standard cylinder specimens were demolded at 3, 9, and 15 days after placement and subsequently cut into three pieces with 5.1 cm (2 inch) thickness at 2.5, 7.6, and 17.8 cm (1, 3, and 7 inch) from top surface. Splitting tensile strength tests were conducted in accordance with ASTM C 496 (1999) for each piece of the specimens immediately after cutting.

Figure 3-6 Instrumented 15.2 × 30.5 cm Standard Cylinder Mold.

Temperature and Moisture Measurements

Temperature, relative humidity, and conventional maturity of the 30.5 × 30.5 cm (12 × 12 inch) cylinder specimen were determined over a 21 day period at each depth. The concrete temperature at the time of placement was 23 ^{o}C and reached a maximum temperature of 62 ^{o}C approximately 12 hours after placement as shown in Figure 3-7 (a). Subsequently, the temperature of the specimen stabilized near 60 ^{o}C. The trend of maturity with curing time was almost linear because of the continuously stabilized temperature of the specimen as shown in Figure 3-7 (b). Because of low relative humidity in the environmental chamber, the relative humidity near the top surface of the specimen decreased over the 21 day period due to a high level of evaporation. The relative humidity decreased to 53, 82, and 91 percent at depths of 2.5, 7.6, and 17.8 cm (1, 3, and 7 inch), respectively, at 21 days after placement.

Strength of Concrete at Different Moisture Levels

Concrete strength at 2.5, 7.6, and 17.8 cm (1, 3, and 7 inch) from the top surface of the strength specimens were determined by splitting tensile testing of 5.1 cm (2 inch) slices cut at the noted positions. The strength data were correlated to the moisture and the maturity data obtained from the moisture specimen. At the same conventional maturity, strengths of each piece cut from different depths of the standard cylinder specimens are separated (Figure 3-8) due to the different moisture levels (Figure 3-7 (c)) although they consist of the same mix proportions (Table 3-2). This implies that temperature-based maturity concepts have shortcomings in predicting concrete strength cured under the different moisture conditions.

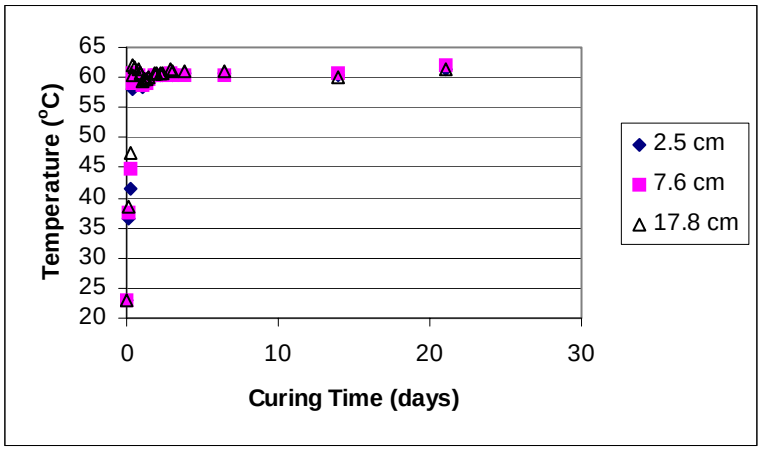

(a) Temperature

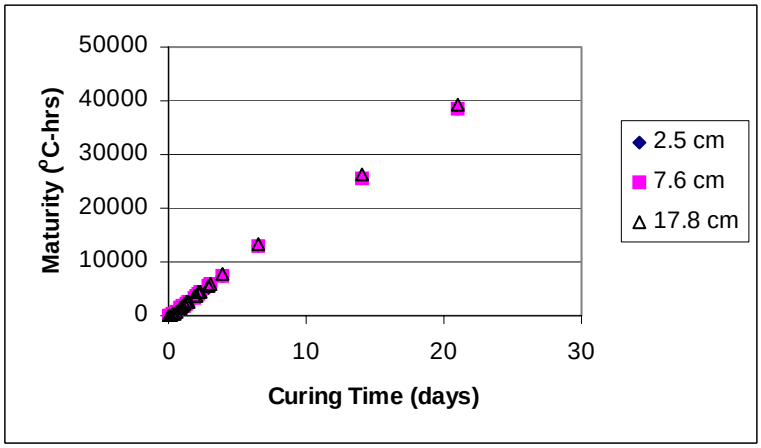

(b) Temperature-Based Maturity

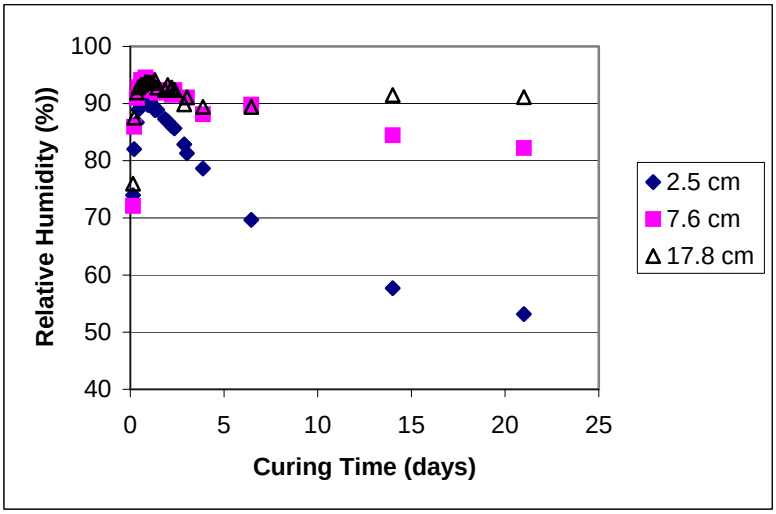

(c) Relative Humidity

Figure 3-7 Temperature, Moisture, and Maturity Histories at Different Depths of 30.5 × 30.5 cm Cylinder Specimen.

The reciprocal of strength at the different locations was plotted against the reciprocal of maturity as shown in Figure 3-9. Ultimate splitting tensile strength was predicted as 3.07, 3.14, and 3.26 MPa (445, 455, and 473 psi) for the segments cut 2.5, 7.6, and 17.8 cm (1, 3, and 7 inch) from the top surface, respectively. The trends of double logarithm of the relative strength of each segment against the logarithm of the maturity are different by depths as presented in Figure 3-10, although they were made from the same mix proportions.

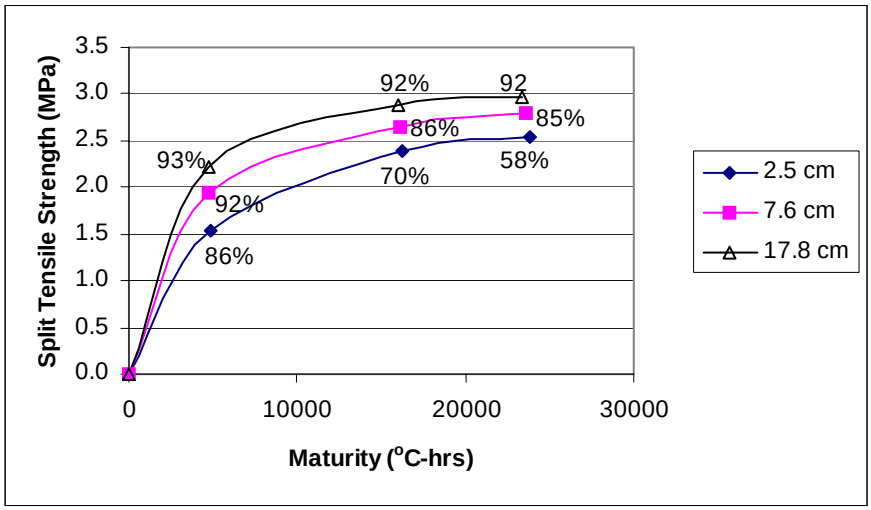

Figure 3-8 Measured Splitting Tensile Strengths and Relative Humidity with Maturity at Different Depths of Specimens.

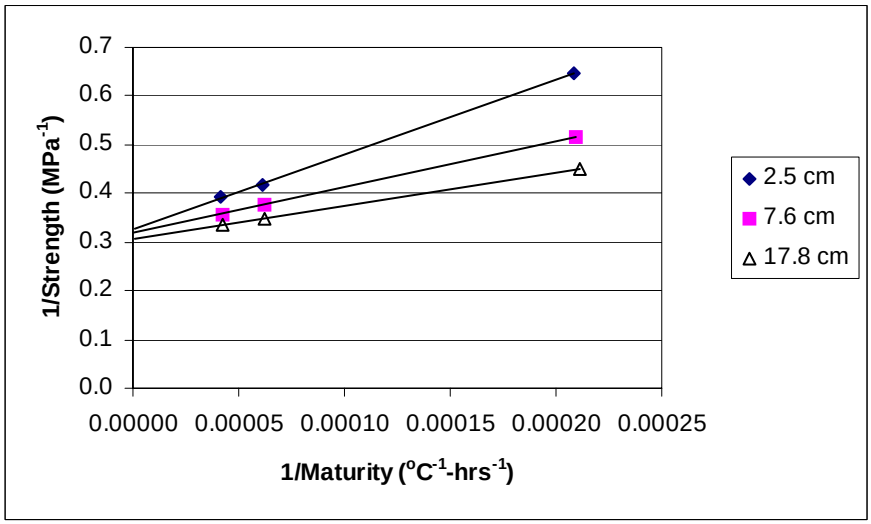

Figure 3-9 Reciprocal Method for Ultimate Splitting Tensile Strengths at Different Depths of Specimens.

Because of the different trends of each segment, standard errors of the intercept and the slope of the trend line made from all data points were relatively high as shown in Figure 3-10. This fact implies that the moisture, one of the most important factors of hydration

of concrete, needs to be incorporated into the existing temperature-based maturity for better prediction of strengths of concrete under variable moisture conditions.

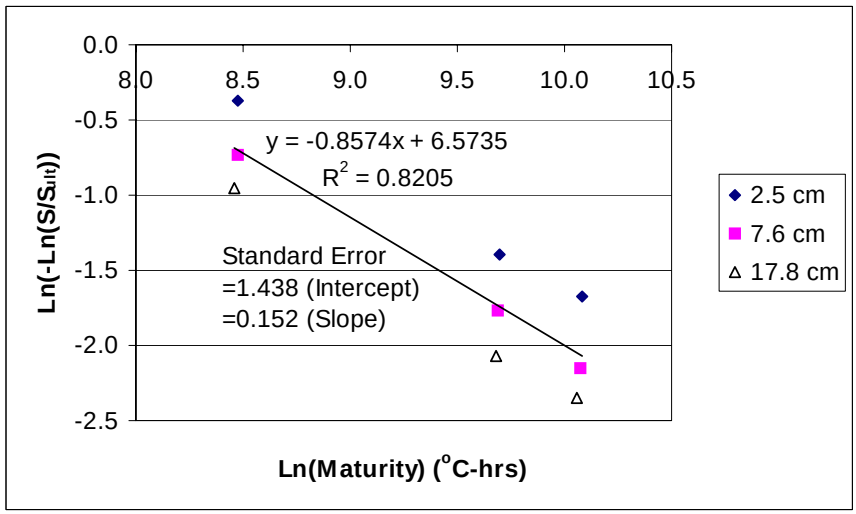

Figure 3-10 Logarithmic Relationship between Relative Strength and Maturity at Different Depths of Specimens.

Moisture Modification Factor (β_H)

A moisture modification factor shown in equation (3-5) was originally modeled for numerical computation of moisture effect on equivalent curing time (Bažant, 1969) on the basis of the observation of concrete moisture (Powers, 1947).

$$\beta_H = \left[1 + (7.5 - 7.5H)^4\right]^{-1} \qquad (3\text{-}5)$$

where β_H is the moisture modification factor and H is the humidity of the concrete. The value of the moisture modification factor decreases as the relative humidity of the concrete decreases as shown in Figure 3-11. The moisture modification factor represents the influence of moisture upon the rate of hydration reaction. Therefore, strength of concrete at a level of moisture can be adjusted by use of the moisture modification

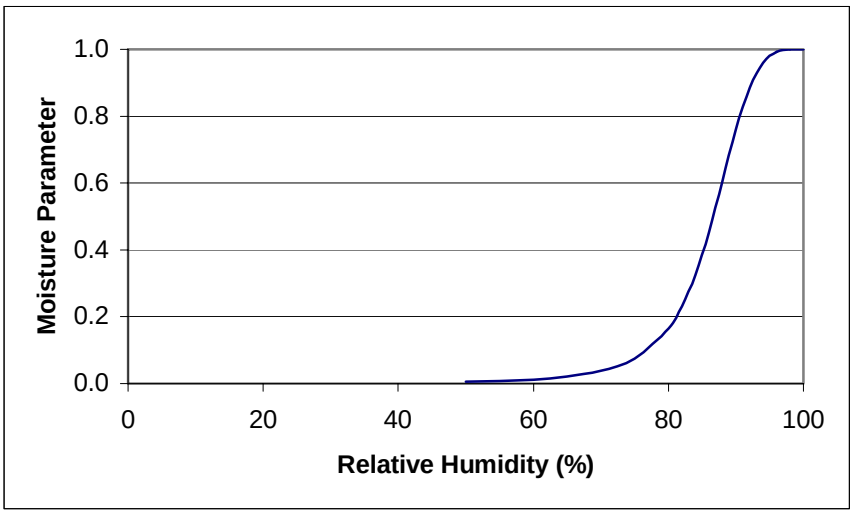

Figure 3-11 Moisture Modification Factor Varies with Relative Humidity (Bažant, 1969).

factor. It is suggested that the temperature-based maturity may be adjusted by incorporating the moisture modification factor into the Nurse-Saul maturity function (equation (3-1)) as:

$$M_H = \beta_H \cdot \sum_0^t (T - T_0) \cdot \Delta t = \frac{\sum_0^t (T - T_0) \cdot \Delta t}{1 + (7.5 - 7.5H)^4} \qquad (3\text{-}6)$$

The relationship between the double natural logarithm of the relative strength and the natural logarithm of the moisture-modified maturity presented in Figure 3-12 shows an improved linear trend evidenced by the R-square value and standard errors of the trend line in Figure 3-10. The improved linear relationship implies that the moisture-modified maturity is useful in prediction of concrete strengths under variable curing conditions.

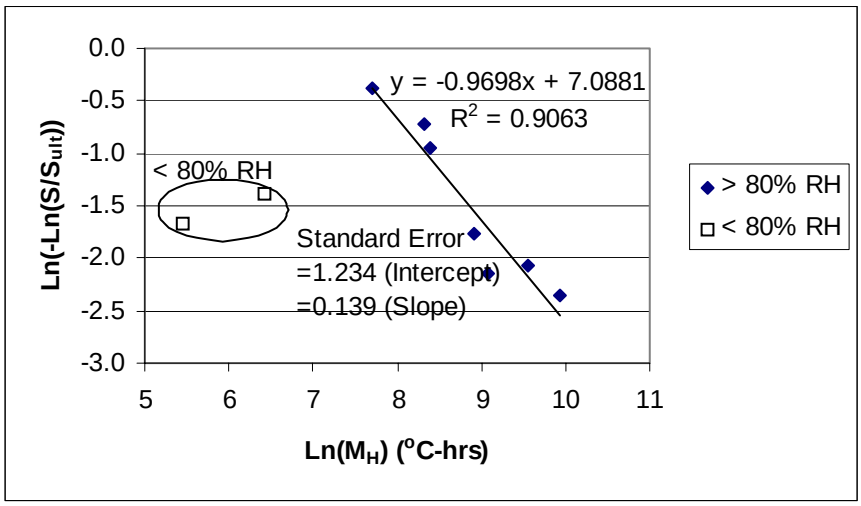

Figure 3-12 Logarithmic Relationship between Relative Strength and Moisture-Modified Maturity at All Depths of Specimens.

The trend line in Figure 3-12 is based only on data points with relative humidity over 80 percent. Because the moisture modification factor originally was modeled under the observation that hydration completely stopped when the relative humidity of the drying concrete decreased to approximately 80 percent, there exist two erratic points that are associated with concrete tested at relative humidity below 80 percent. Due to recent technological advancements, measured relative humidity values are highly reliable due to significant development of the measurement devices and instrumentation techniques compared to a few decades ago. Nonetheless, the strength increased steadily in spite of the measured relative humidity being below 80 percent as shown in Figure 3-12. This indicates a basis on which to make modifications to the model coefficients originally

suggested by Bažant and Najjar (1972). The model of moisture-modified maturity (equation (3-6)) was improved by modifying the coefficients in the moisture modification factor shown in equation (3-7).

$$\beta_H^{'} = \left[1 + (a - aH)^b\right]^{-1} \tag{3-7}$$

Moisture-modified maturity is re-formulized by using the corrected moisture modification factor, which uses 5.0 and 1 as its coefficients, *a* and *b*.

$$M_H^{'} = \beta_H^{'} \cdot \sum_0^t (T - T_0) \cdot \Delta t = \frac{\sum_0^t (T - T_0) \cdot \Delta t}{1 + (5 - 5H)}$$

The new trend of the corrected moisture modification factor and the improved logarithmic relationship between relative strength and new moisture-modified maturity are shown in Figures 3-13 and 3-14, respectively. The R-square value and the standard errors of the trend line shown in Figure 3-14 were made from all data points in the chart. The results shown in Figure 3-15 suggest that the proposed moisture-modified maturity can successfully coalesce the splitting tensile strength curves at different curing moisture presented in Figure 3-8 into one curve.

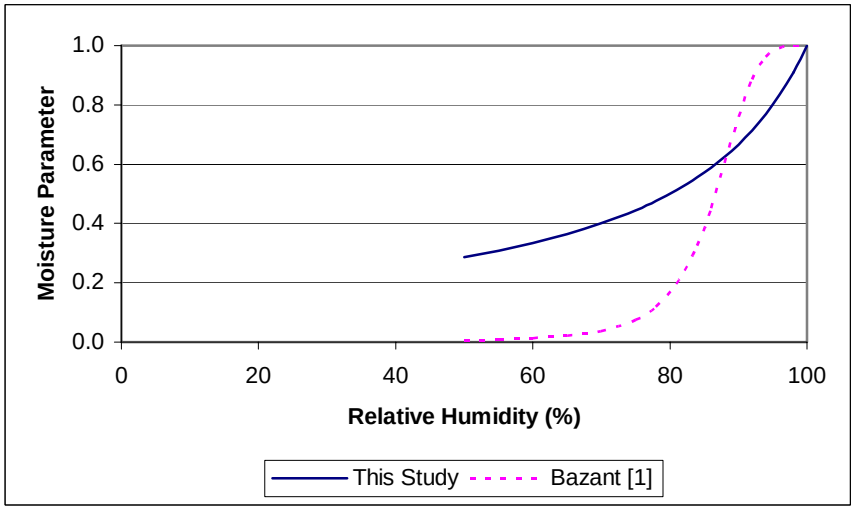

Figure 3-13 Corrected Moisture Modification Factor Varies with Relative Humidity.

CONCLUSIONS

It is suggested that the linear relationship between the double natural logarithm of relative strength and the natural logarithm of the maturity is independent of curing temperature. Once the strength-maturity relationship is obtained for a given mixture design, this relationship can be used to find the opening maturity under any curing

temperature. To consider the effect of moisture on the strength-maturity relationship, the Nurse-Saul maturity model was modified by including a moisture modification factor as suggested by Bažant. The moisture modification factor originally was developed based on the observation that hydration stopped when the relative humidity of the drying concrete decreased to approximately 80 percent. However, concrete strength steadily increased below 80 percent of relative humidity and, as a result, the moisture modification factor was modified. The improved linear logarithmic relationship between relative strength and maturity was made by using the corrected moisture modification factor. To consider the moisture variation due to environmental conditions in the field, a cumulative moisture modification factor that utilizes moisture history of concrete needs to be incorporated.

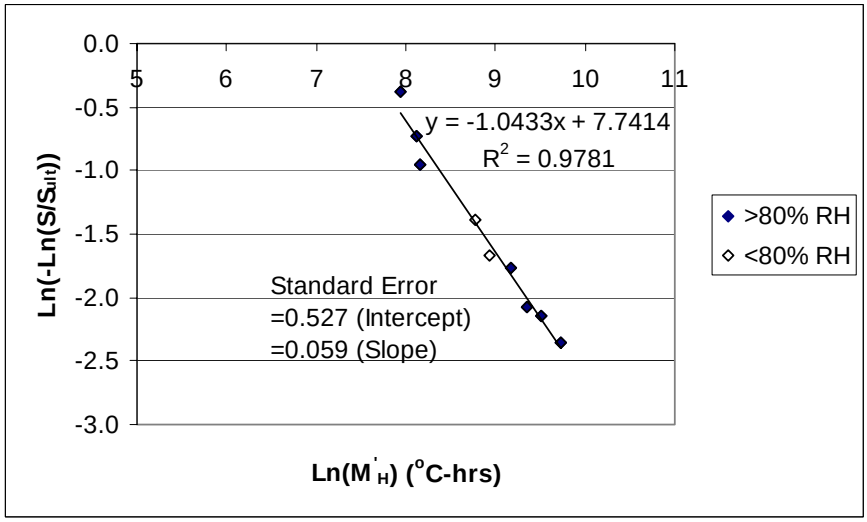

Figure 3-14 Improved Logarithmic Relationship between Relative Strength and Corrected Moisture-Modified Maturity at All Depths of Specimens.

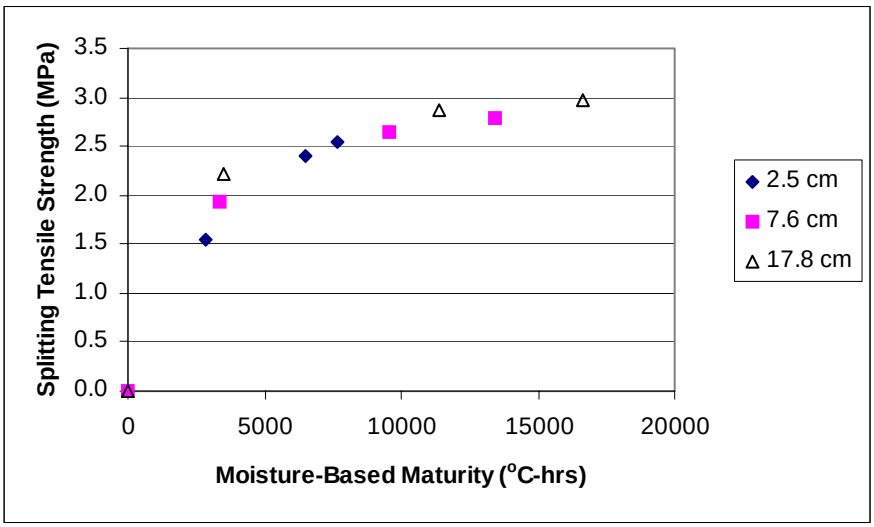

Figure 3-15 Splitting Tensile Strength with Corrected Moisture-Modified Maturity at All Depths of Specimens.

CHAPTER 4
EVAPORATION MODELING FOR CONCRETE PAVEMENTS

Early age moisture loss from the surface of a concrete pavement may induce undesirable effects that play a factor in long-term performance. Early-aged detrimental behaviors such as slab curling, warping, delamination, and even plastic shrinkage cracking are affected by the amount of evaporation and the effectiveness of the curing medium. The rate of evaporation is a key item relative to monitoring the quality of the curing. However, most approaches for this are largely empirical and are only useful under laboratory conditions. The effective curing thickness concept is introduced as a method to evaluate the curing effectiveness of a curing method.

The surface relative humidity has the biggest influence on both the effective curing thickness and the rate of evaporation. Prediction of the evaporation rate of concrete depends on the surface relative humidity and is important for evaluation of the method of curing. Existing evaporation models, including the American Concrete Institute (ACI) nomograph, were evaluated relative to their capability to predict the evaporation from the curing concrete. A modified version of Penman's evaporation model is presented in terms of data collected in a series of laboratory experiments.

INTRODUCTION

Available moisture in hardening concrete evolves into two types of water — one referred to as evaporable water held in both capillary and gel pores including interlayer pores and the other as non-evaporable water combined structurally in the hydration products (Neville, 1996; Mindess and Young, 1981). The sum of these portions equals the total water content in the paste. Water available in the capillary pores evaporates at the surface of concrete when it is exposed to ambient weather conditions, causing a decrease in vapor pressure above the concrete surface. Because the predominance of moisture movement associated with evaporation occurs near the surface of the concrete, moisture variations within the cross section of the concrete are found mostly near the surface. Typical relative humidity profiles for both a specimen made in the laboratory and a test slab made in the field are shown in Figure 4-1. These moisture profiles are of concern with

respect to the effect on slab deflections and development of delaminations in bonded concrete overlay systems (Wang and Zollinger, 2000) at an early age.

Evaporation at the surface of a concrete slab can be defined as the net rate of vapor transport to the surrounding atmosphere (Linsley et al., 1975). This change in state requires an exchange of approximately 600 calories for each gram of water evaporated. Vaporization removes heat from bleed water near the surface of the concrete slab. Therefore, evaporation is another important factor to be considered in the analysis of thermally induced effects on a concrete slab in addition to conduction, convection, and radiation (Kapila et al., 1997).

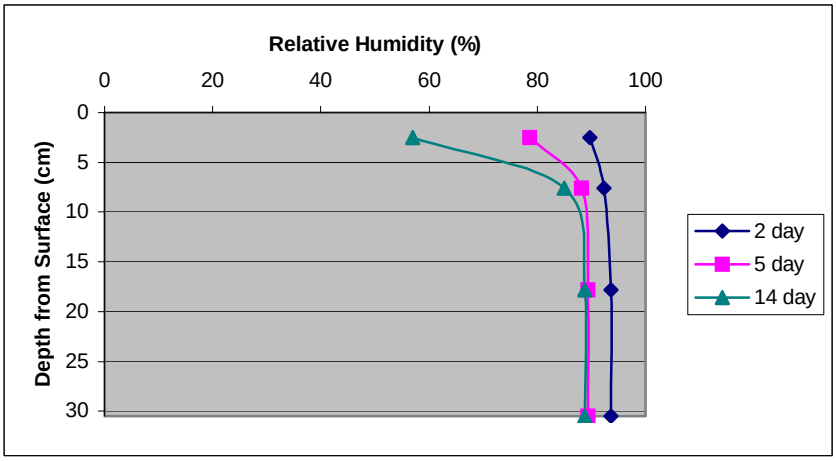

(a)

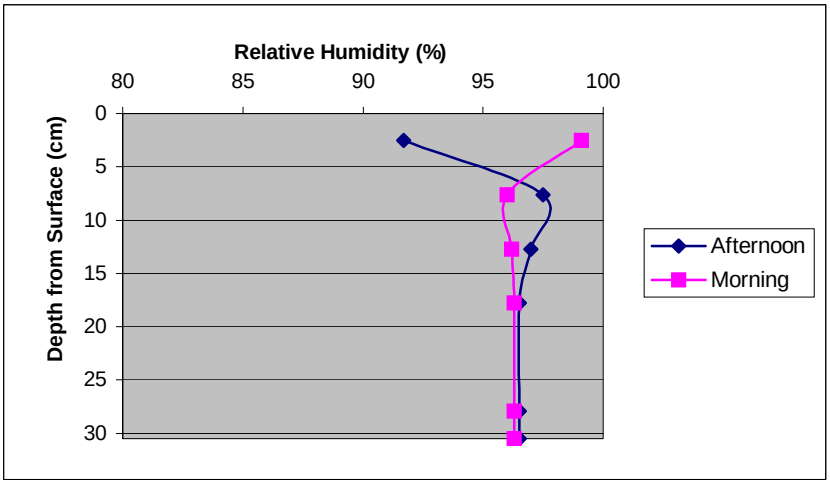

(b)

Figure 4-1 Moisture Profiles in Concrete: (a) From a Specimen Cured in 15 Percent Room Relative Humidity; (b) From a Test Slab Cured in Field.

Evaporation is controlled by use of the appropriate curing method to minimize potential for undesirable cracking and deformation at early ages. The presence of water serves to enhance both hydration and strength development. As hydration advances and fills the space available in the capillary pores, capillary porosity continues to decrease and the amount of the gel pores increases. Gel pores tend to limit the movement of moisture through the capillary pores. Thus, the increase of hydrated products and reduced capillary

porosity reduces the rate of evaporation. Drying shrinkage, due to evaporation, which leads to cracking or warping is also controlled by minimization of water loss from capillary pores (Mindess and Young, 1981; Neville, 1996). Strength of concrete is affected not only by the total moisture content but also by the moisture variations in the concrete. For an example, test data have indicated that even a short period of drying causes a recognizable decrease in the magnitude of tensile strength of the concrete due to the moisture variation at the concrete surface (Walker and Bloem, 1957).

Numerous efforts have been made to develop empirical models to express evaporation as a function of atmospheric factors (Penman, 1948; Thornthwaite, 1948; Menzel, 1954; Wilson, 1990; Wilson, 1994; Veihmeyer, 1964). Most of the models are of the Dalton type and have been presented in the form of (Dalton, 1802):

$$E = (e_s - e_d)\, f(v) \tag{4-1}$$

where

E	=	rate of evaporation ($ML^{-2}T^{-1}$)
e_s	=	saturation vapor pressure of water surface (ML^{-2})
e_d	=	vapor pressure of air above water surface (ML^{-2})
$f(v)$	=	wind function
v	=	wind speed (LT^{-1})
M	=	mass
L	=	length
T	=	time

The ACI nomograph (1996) shown in Figure 4-2 was based on the Menzels model (1954) derived from Dalton's model (1802) and the Lake Hefner test results conducted between 1950 and 1952 (Kohler et al., 1955). The Menzels model, equation (4-2), has been accepted as one of the best methods for predicting evaporation of bleed water while it is exposed on the surface of the concrete (which inherently excludes the consideration of curing media).

$$E = 0.44(e_s - e_d)(0.253 + 0.096v) \tag{4-2}$$

However, since the quantified net radiation was not measured during the Lake Hefner tests, this model fails to consider the effects of radiation on evaporation. Another shortcoming is

related to vapor pressure effects, which can be overcome by considering the many equations that have been suggested to express vapor pressure as a function of temperature (Tetens, 1930; Murray, 1967; Dilley, 1968). Another widely used method for evaporation prediction is Penman's model (Penman, 1948). Penman's model, shown in equation (4-3), is also a Dalton's type model but resolves the difficulties associated with them relative to wind and surface vapor pressure effects. This model predicts evaporation by considering both net radiation and aerodynamic effects.

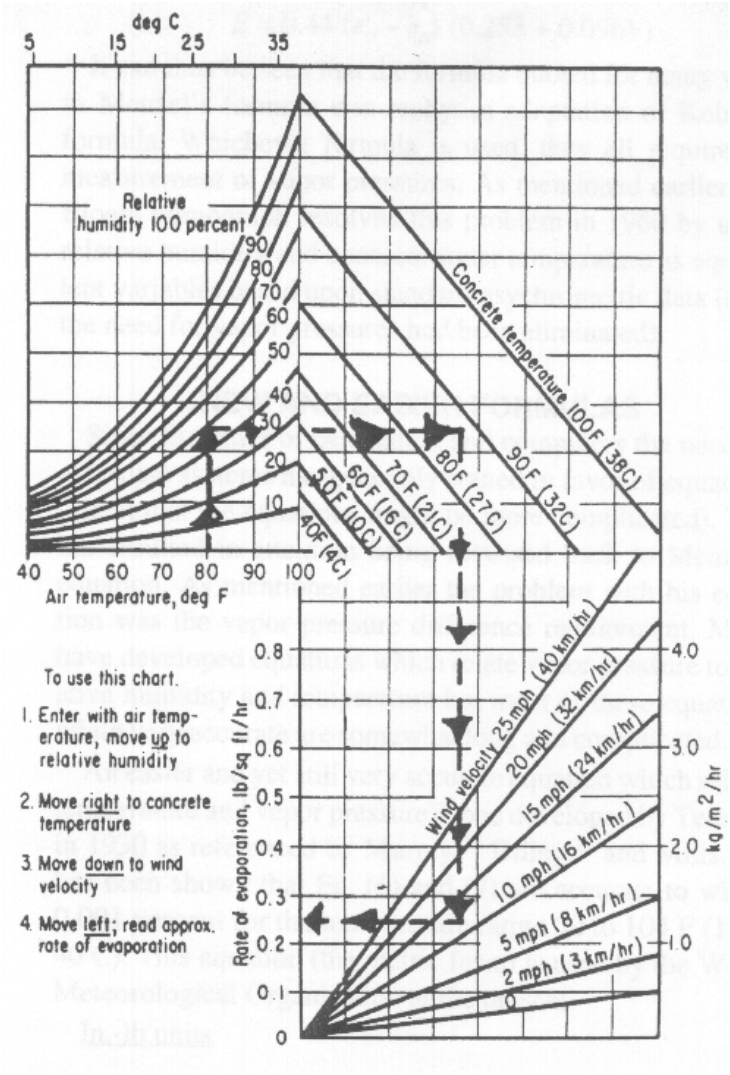

Figure 4-2 ACI Evaporation Nomograph (ACI, 1996).

$$E = \frac{\Delta E_q + \gamma E_a}{\Delta + \gamma} \tag{4-3}$$

where

Δ = slope of the saturation vapor pressure versus temperature curve (ML^{-2})

$$= \frac{e_s - e_a}{T_s - T_a}$$

e_a = saturation vapor pressure of air (ML^{-2})

T_s = surface temperature

T_a = air temperature

E_q = rate of evaporation due to net radiation ($ML^{-2}T^{-1}$)

γ = psychrometric constant (ML^{-2})

E_a = rate of evaporation due to aerodynamic effects ($ML^{-2}T^{-1}$)

Both the ACI nomograph and Penman's model are based on evaporation from a water surface but fail to consider the effects of changes of moisture within the concrete with time, and consequently cannot accurately predict evaporation from concrete (particularly, beyond the cessation of bleeding). Therefore, development of a theoretical model for prediction of evaporation from concrete both before and after bleeding is necessary.

LABORATORY TEST PROGRAM

A laboratory test program was carried out to develop a test methodology and a database to formulate a modified version of Penman's model to yield an improved evaluation method for different methods of curing for concrete pavement construction. A cylindrical mold with inside diameter of 30.5 cm (12 inch) and a height of 15.2 cm (6 inch) was prepared. The mold consisted of 1.3 cm (0.5 inch) thick PVC wall and end plate with a thickness of 0.6 cm (0.25 inch). Concrete was placed in the mold and was compacted according to ASTM C 192 (1999). The concrete mixture for this testing consisted of a crushed limestone coarse aggregate and a natural sand as the fine aggregate. Table 4-1 presents the mix proportions. A water-cement ratio of 0.46 was used, and the unit weight of concrete was determined using ASTM C 29 (1999) and was found to be 2422 kg/m^3 (151 lb/ft^3).

Table 4-1 Mix Proportions in 1 m^3 (35.3 ft^3) of Concrete.

Materials	Proportions
Coarse Aggregate (Limestone)	1143 kg (2520 lb)
Fine Aggregate (Natural Sand)	753 kg (1660 lb)
Cement (Type I)	360 kg (794 lb)
Water	166 kg (366 lb)
Water/Cement	0.46
Concrete Unit Weight	2422 kg/m^3 (151 lb/ft^3)

After placing concrete in the mold, a curing monitoring system manufactured by ATEK and an electronic

scale with 0.1 gram accuracy was used to collect data from the concrete while it cured. The ATEK system consisted of three sensors to measure the ambient relative humidity, and the relative humidity at the concrete surface and inside the concrete as shown in Figure 4-3. The relative humidity inside the concrete was determined from a chilled mirror type sensor, which measures the dry bulb and the dew point temperature from inside a plastic casing. The relative humidity (H) data are calculated from dry bulb (T) and dew point (T_{dp}) temperature data using the following expression:

$$H = \exp\left[\left(\frac{17.502T_{dp}}{240.97+T_{dp}}\right)-\left(\frac{17.502T}{240.97+T}\right)\right]$$

The ATEK system includes a plastic casing, as noted in Figure 4-3, connected to an aluminum stand that supports the weight of the curing monitoring system, which is inserted approximately 5.1 cm (2 inches) into the concrete. There are four holes in the casing 1.9 cm (0.75 inch) below the concrete surface to allow the vapor pressure of the concrete to equilibrate inside the casing. The surface sensor measures the relative humidity from inside a PVC

(a)

(b)

(c)

Figure 4-3 Instrumentation and Devices: (a) View of Setup; (b) Chilled Mirror Sensors and Reader; (c) Stand and Tip.

cylinder with an inside diameter and height of 6.4 cm (2.5 inch) and 5.1 cm (2 inch), respectively, as shown in Figure 4-3 (b). The cylinder is placed on the concrete surface in an area cleared of the curing membrane such that the sensor will register the relative humidity just below the curing membrane. The third sensor measures the relative humidity just above the curing membrane. During the curing, weight loss of the specimen and relative humidity conditions, surface, and in the concrete were measured until the surface relative humidity equilibrated with the ambient relative humidity. Four different wind speeds, zero, 2.08, 2.83, and 5.33 m/s (zero, 4.65, 6.33, and 11.92 mph), were used at room temperature and relative humidity of 40 ^{o}C and 15 percent, respectively.

RELATIVE HUMIDITY TRENDS

Other laboratory tests were conducted using a different relative humidity sensor arrangement to observe the trends of relative humidity with time and to use in back-calculate the moisture diffusivity. Concrete was placed in a cylindrical PVC mold with a diameter of 20.3 cm (8 inch) and a height of 30.5 cm (12 inch). Moisture sensors were located 2.5, 7.6, and 12.7 cm (1, 3, and 5 inch) below the exposed surface. The temperature and relative humidity of the curing room were 32 ^{o}C and 50 percent, respectively.

Immediately after placement, the concrete manifests low relative humidity as noted in Figure 4-4, which appears to be due to significantly high values of moisture diffusivity in the concrete while it is in a fresh state as shown in Figure 4-5. Low vapor pressure of concrete due to high moisture diffusivity results in low initial relative humidities. On the basis of numerous results from the field

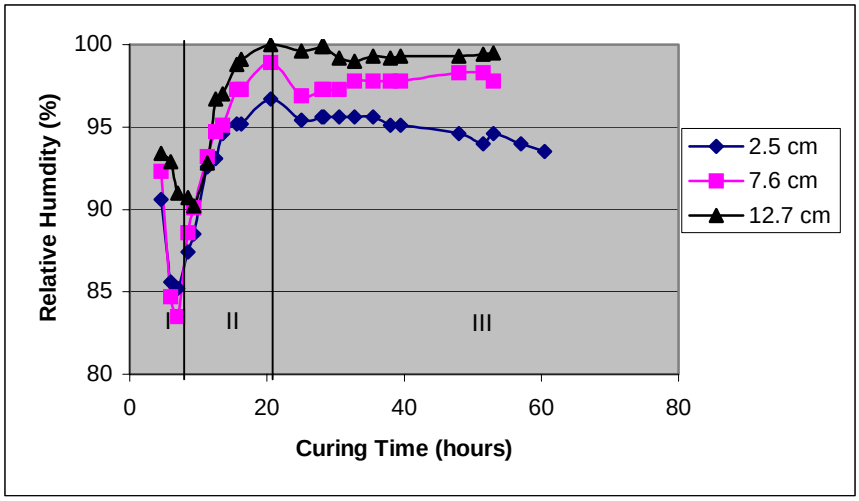

Figure 4-4 Relative Humidity History of Concrete (Laboratory Test).

and the lab, the trend of relative humidity of concrete can be categorized by three stages as shown in Figure 4-4. During the first stage (placement of concrete), the initially high relative humidity decreases rapidly due to high values of moisture diffusivity of concrete. This decrease may be caused by a condition of non-equilibrium between the vapor pressure inside the concrete and the surrounding atmosphere immediately after placement. The rate of evaporation during this stage may be accompanied by some bleeding. In Stage II, referred to as the bleeding stage, the relative humidity increases with time and comes to a peak as the initially high moisture diffusivity begins to decrease. The moisture diffusivity, nonetheless, is still at a comparatively high level so the evaporation rate is still at a comparatively high rate. During the third stage (referred to as post bleeding), relative humidity decreases with time and is equilibrated to the ambient relative humidity due to reduced moisture diffusivity of the concrete. The duration of each stage depends upon the prevalent curing conditions and water content of the concrete mixture.

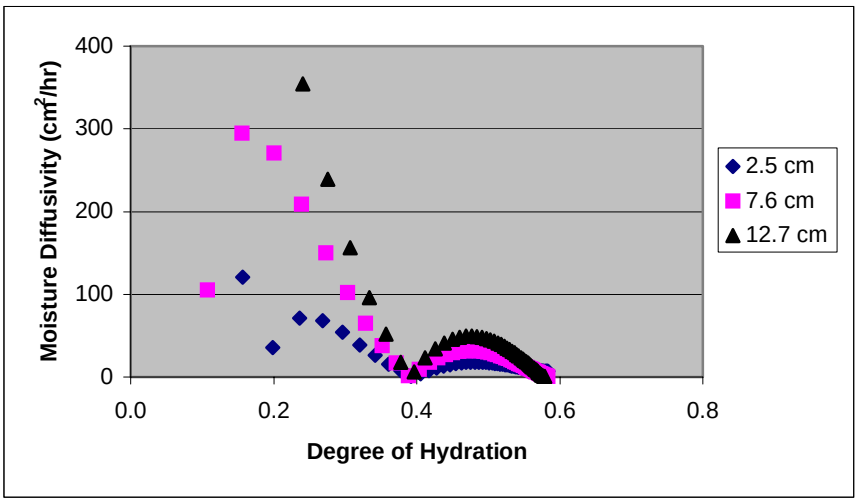

Figure 4-5 Back-Calculated Moisture Diffusivity.

DETERMINATION OF CURING EFFECTIVENESS

As concrete dries, free moisture disappears from the surface due to evaporation. Furthermore, higher rates of evaporation induce larger moisture variations within the cross section of the concrete immediately below the surface. If evaporation is minimized by a given curing method, the relative humidity immediately below the surface will be relatively constant with time and will have little variation due to effects of the relative humidity outside the concrete because of the insulative effects of the curing membrane. The effects of the ambient moisture conditions and the moisture levels at the concrete surface need to

be included in the modified Penman's model to improve its sensitivity to the curing conditions of the concrete. To this end, the researchers adopted the effective curing thickness concept originally introduced by (Bažant and Najjar, 1972):

$$L = \frac{\ln \frac{H_s}{H_a}}{\frac{\partial H_s}{\partial x}}$$

where

L = effective curing thickness (L)

H_s = surface relative humidity

H_a = ambient relative humidity

Effective curing thickness can be described as the equivalent layer of concrete that would provide the same degree of curing as the curing medium. Properly cured concrete has an effective curing thickness in the range of 7.6 to 12.5 cm (3 to 5 inch). In other words, the thicker the effective curing thickness is, the larger the humidity difference between the surface and the point immediately below the surface (Bažant and Najjar, 1972).

For a few hours after placement, the relative humidity of the surface and inside the concrete increases because of bleeding as shown in Figure 4-6. Bleed water exists on the concrete surface in spite of the high rates of evaporation over this period of time as shown in Figure 4-7. It is after the bleeding is complete that the surface relative humidity eventually diminishes to the ambient relative humidity.

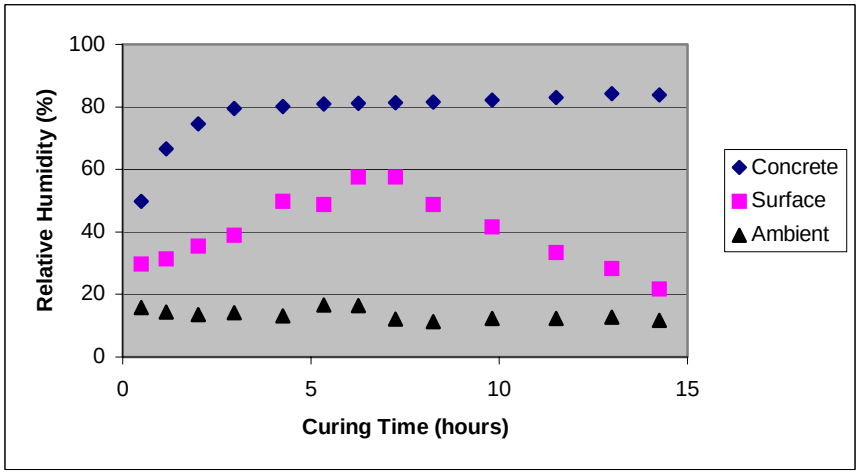

Figure 4-6 Relative Humidity with Curing Time at Each Position (No Wind Case).

The initial rates of evaporation computed from the test data were clearly affected by wind speeds (v). Higher wind speeds initially increase the amount of accumulative evaporation while there was little effect after a few hours as shown in Figure 4-7. ACI

committee 305 suggests that there should be precautions for plastic shrinkage cracking when the evaporation rate exceeds 1.0 kg/m^2/hr (0.2 lb/ft^2/hr) (ACI, 1996). At a wind speed of 5.33 m/s (11.92 mph), the measured evaporation rate exceeded the critical values for approximately 2 hours and then gradually decreased to zero. The measured evaporation rates during this time had nearly the same values as the evaporation rates obtained from the ACI nomograph. However, the measured evaporation rates were much smaller than the evaporation rates predicted by the ACI nomograph after bleeding as shown in Figure 4-8. The ACI nomograph is apparently not sensitive to the effects of various curing methods because the nomograph does not consider the moisture condition in the concrete. Since most curing methods are applied after the bleeding has stopped, the ACI nomograph may have limitations with respect to the prediction of evaporation for both cured and uncured concrete after the bleeding stage.

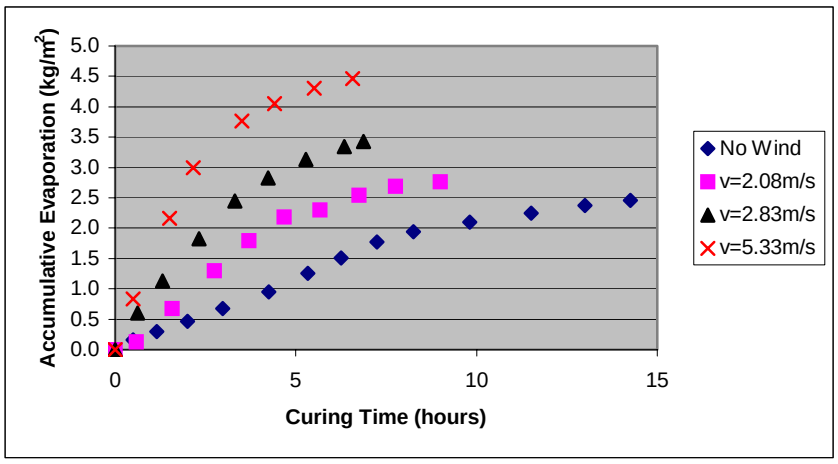

(a)

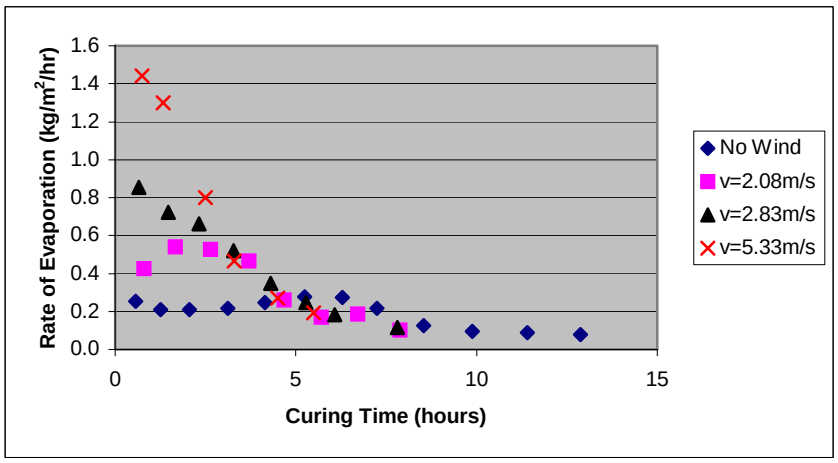

(b)

Figure 4-7 Wind Effect on Evaporation: (a) Accumulative Evaporation; (b) Rate of Evaporation.

The effect of wind speed on the surface relative humidity is shown in Figure 4-9. Obviously, the magnitude of peak surface relative humidity and the duration of bleeding decreased as wind speed increased. The peak surface relative humidity occurred 6.3, 4.7, 3.3, and 2.2 hours after placement for zero, 2.08, 2.83, and 5.33 m/s (zero, 4.65, 6.33, and

11.92 mph) of wind speed, respectively. Interestingly enough, there were little differences in the rate of increase or decrease of surface relative humidity between wind speeds as indicated by the trends shown in Figure 4-9.

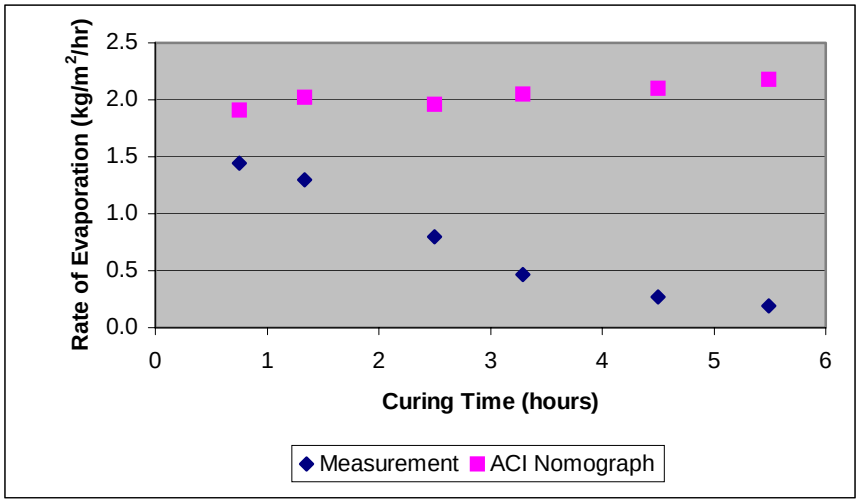

Figure 4-8 Comparison of Evaporation Rate between Measurement and ACI Nomograph (v = 5.33 m/s).

The trends of effective curing thickness shown in Figure 4-10 were similar to those of the surface relative humidity because the effective curing thickness is governed mainly by the surface relative humidity. The effective curing thickness increased throughout the duration of the bleeding as effected by the level of wind speed. The higher wind speed caused a lower effective curing thickness because of the greater loss of moisture from the concrete surface by evaporation. Effective curing thickness represents the quality of curing as shown in Figure 4-10 and perhaps can be used as an indicator of curing quality under both field and laboratory condition. Rate of evaporation is closely related to the curing effectiveness, and a new evaporation model is developed by the test data presented above.

NEW EVAPORATION MODEL

A new evaporation model (equation (4-4)) is based upon the Penman's model previously described in equation (4-3). Both net radiation and aerodynamic

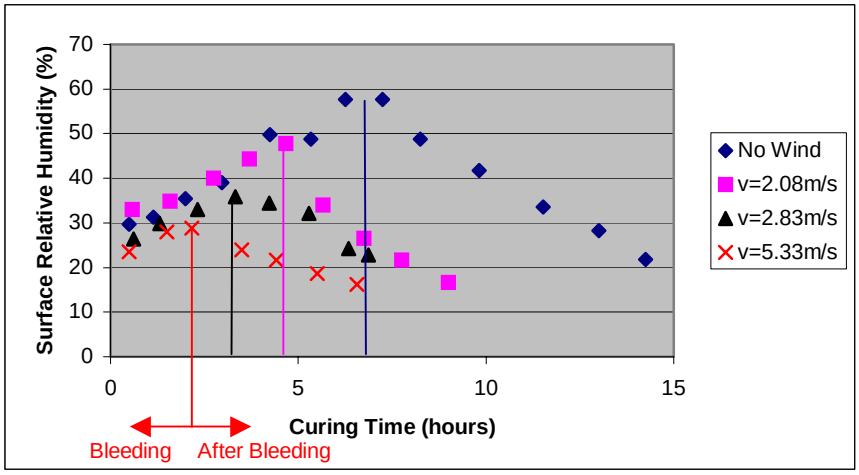

Figure 4-9 Wind Effect on Surface Relative Humidity.

effects are considered in the new model in the same way as in the original Penman's model. As further described below, many constituents in the original model are replaced with other expressions and concrete properties with respect to moisture loss; each are considered and included to formulate the new model to provide more accurate and simpler to understand predictions.

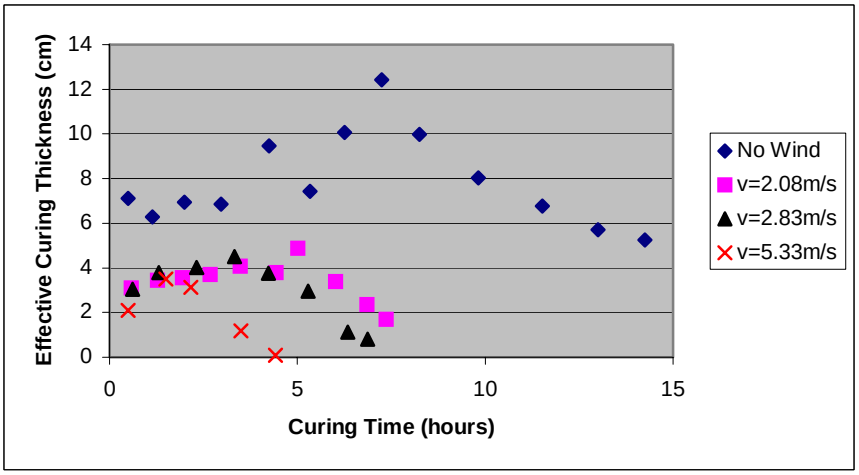

Figure 4-10 Wind Effect on Effective Curing Thickness.

$$E = \delta \frac{Q_s}{H_v} + J \qquad (4\text{-}4)$$

where

E = rate of evaporation from concrete due to both net radiation and aerodynamic effects (kg/m^2/hr)

δ = calibration factor for moisture condition of concrete surface

Q_s = solar radiation absorption through electromagnetic waves (kg/m/hr)

= $\alpha\left[I_d \sin\theta + I_i\left(\frac{1+\cos\gamma}{2}\right)\right]$ (Branco, 1992)

α = surface heat absorptivity of concrete (= 0.6) (Chapman, 1982)

I_d = direct solar radiation (kg/m/hr)

I_i = indirect solar radiation (kg/m/hr)

θ = incidence angle of solar radiation against the slab surface (degree)

γ = inclination angle of slab surface (degree)

H_v = heat of vaporization (heat removed from water on the surface of the concrete slab being vaporized)

= $597.3 - 0.564T_s$ (cal/g) (Linsley, 1975)

$= \quad 427(597.3 - 0.564T_s)$ (m)

J = rate of evaporation from concrete due to convective heat transfer, irradiation, and aerodynamic effects (kg/m^2/hr)

Key parameters of the modified model are described and further elaborated below. The rate of evaporation (E) consists of two components, one due to aerodynamic effects (E_a) explained as the rate of evaporation of a saturated vapor immediately above the water surface (Penman, 1948) and the other due to energy effects (E_q) as shown in equation (4-3). The net radiation (Q_n), which represents the energy exchange at the concrete surface, consists of the elements such as solar radiation, convective heat transfer, and irradiation as:

$$Q_n = Q_s - Q_c - Q_r$$

where

Q_n = net radiation at concrete surface (kg/m/hr)

Q_s = solar radiation absorption (kg/m/hr)

Q_c = heat flux due to convection (kg/m/hr)

$= \quad h_c(T_s - T_a)$ (Branco, 1992)

h_c = convective heat transfer coefficient

$= \quad 6 + 3.7v$ (W/m^2/^{o}C) (Branco, 1992)

$= \quad 367(6 + 3.7v)$ (kg/m/hr/^{o}C)

Q_r = heat energy from high to low temperature body (kg/m/hr)

$= \quad \varepsilon\sigma(T_s^4 - T_a^4)$ (Incropera and DeWitt, 1996)

$= \quad \varepsilon[4.8 + 0.075(T_a - 5)](T_s - T_a)$ (Branco, 1992)

ε = surface heat emissivity of concrete (= 0.88) (Chapman, 1982)

σ = Stefan-Boltzmann constant (= 5.67 × 10^{-8} W/m^2/^{o}K^4 = 2.08 × 10^{-5} kg/m/hr/^{o}K^4) (Chapman, 1982)

Although several parameters are involved, under laboratory conditions, only convective heat transfer and irradiation are considered to have an effect on evaporation.

During bleeding, a concrete surface is covered with a continuous layer of water that is perhaps maintained for a period of time depending on the water content in the mix and

the rate of evaporation. However, as evaporation continues, the water layer on the concrete surface becomes less continuous and isolated until it completely vanishes from the concrete surface. Beyond this point evaporation continues under dry surface conditions. In light of this phenomenon, it is clear that evaporation modeling for hydrating concrete needs to be sensitive to evaporation under both wet and dry surface conditions. In either case, the rate of evaporation at a concrete surface under laboratory curing conditions (i.e., non-solar effects) in terms of the variation in moisture movement from the concrete to the atmosphere is represented by the parameter J (Bažant and Najjar, 1972), which is included in equation (4-4):

$$J = B \ln \frac{H_s}{H_a}$$

where B is surface moisture emissivity and has been found to be a function of the effective curing thickness and wind speed and is closely related to the given curing conditions. Characterization of surface moisture emissivity is very useful since it provides the means to include the moisture characteristics of the concrete as a function of curing time to be incorporated into Penman's model. Additionally, if there is no solar radiation (Q_s), such as under laboratory conditions, the evaporation rate of concrete (E) can be assumed to be equal to the evaporation rate of concrete due to convective heat transfer, irradiation, and aerodynamic effects (J). Thus, surface moisture emissivity (B) can be characterized by a series of laboratory tests in absence of solar radiation.

$$B = \frac{J}{\ln \frac{H_s}{H_a}} = \frac{E}{\ln \frac{H_s}{H_a}}$$

Test results for evaporation and curing thickness imply that the characterization of surface moisture emissivity needs to be carried out in two categories: one during bleeding and the other after bleeding. Obviously, plots of surface moisture emissivity versus effective curing thickness in Figure 4-11 showed that the data should be divided into the two categories and then analyzed separately. Effective curing thickness increases while surface moisture emissivity decreases with curing time during bleeding. Conversely, effective curing thickness decreases while surface moisture emissivity increases with curing time after bleeding. This relation between effective curing thickness and surface moisture

emissivity was expected by (Bažant and Najjar, 1972) even though the two categories by bleeding were not considered. Consequently, the surface moisture emissivity (B) can be formulized as functions of effective curing thickness (L) and wind speed (v) during and after bleeding, respectively.

During bleeding ($R^2 = 0.994$):

$$B = a + b\exp(-L) + cv^2$$

After bleeding ($R^2 = 0.999$):

$$B = d + \frac{e\ln L}{L} + fv^{2.5} \quad (4\text{-}13)$$

where the unit of surface moisture emissivity is kg/m^2/hr, effective curing thickness is cm, and wind speed is m/s. The standard errors of coefficients ranged from 1.9 to 21.9 percent.

As previously mentioned, another source of evaporation is due to solar radiation at the concrete surface (Penman, 1948). Specifically, the rate of evaporation by solar radiation is calculated

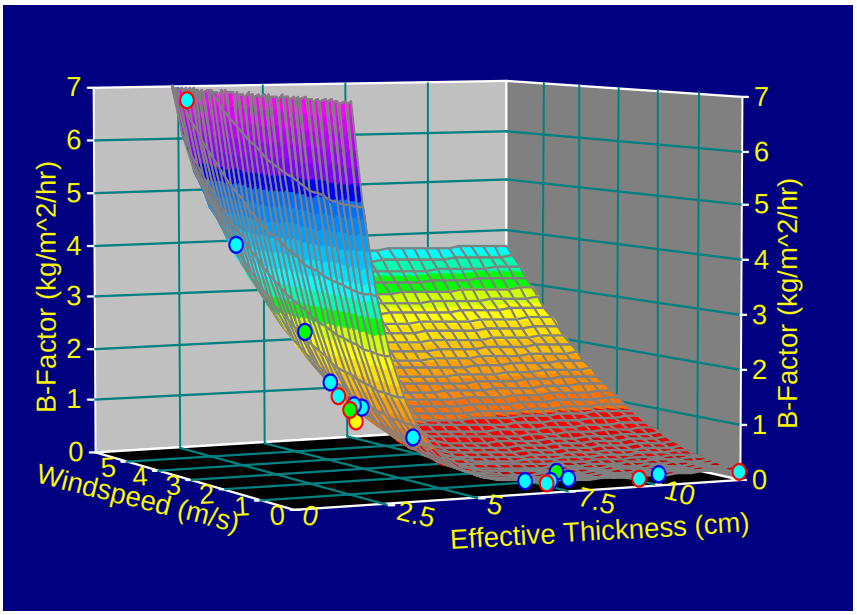

(a)

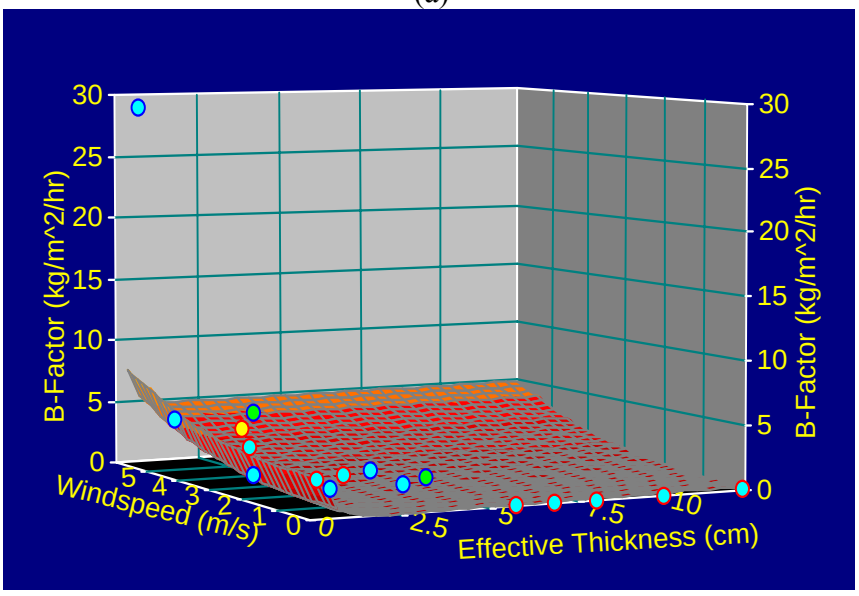

(b)

Figure 4-11 Trends of Surface Moisture Emissivity: (a) During Bleeding; (b) After Bleeding.

from the solar radiation divided by heat of vaporization (H_v) at the slab surface (Linsley et al., 1975). In this regard, moisture conditions at the concrete surface with time also should be considered since during the bleeding stage, the solar radiation will cause the higher rate of evaporation. However, the evaporation by solar radiation will decrease as the concrete surface dries after bleeding. The present form of Penman's model does not consider the drying effects of the concrete surface on evaporation due to solar radiation. Thus, a calibration factor considering drying effects of concrete on the evaporation by solar radiation was included in equation (4-4) using the effective curing thickness concept to represent the moisture condition at the concrete surface.

$$\delta = \frac{L}{C} \qquad \text{when} \quad C \geq L$$

$$\delta = 1 \qquad \text{when} \quad C < L$$

where δ is the calibration factor included in equation (4-4), and C is the ideal effective curing thickness (= 7.6 cm) determined by the experimental experience of the authors.

A field test was conducted at the Riverside Campus of Texas A&M University in Bryan, Texas, to demonstrate the validity of the new evaporation model (equation (4-4)) illustrated in Figure 4-12. This field test consisted of placing the concrete at 8:23 am, and the test was finished at 2:30 pm when the relative humidity at the concrete surface had equilibrated with the ambient relative humidity. Solar radiation and wind speed were measured by a weather station placed near the concrete specimen. Ambient temperature and relative humidity, and the temperature and relative humidity at the concrete surface, and inside the concrete also were measured by the ATEK curing monitoring system. The rate of evaporation calculated by the new evaporation model (equation (4-4)) agrees well with the measured one, while the rate of evaporation from the ACI nomograph is underestimated during bleeding (in the morning) and overestimated after bleeding (in the afternoon). The advantages of the new evaporation model are improved prediction and sensitivity to the factors that control the amount of evaporation from hardening concrete for different curing methods.

CONCLUSIONS

A test methodology was developed to evaluate curing methods for concrete pavement. Effective curing thickness is suggested to be a parameter to evaluate or assess the quality of curing concrete. Maintaining higher levels of surface relative humidity is important for better curing quality. The curing condition was influenced by wind speed significantly, and minimization of wind effects is an important factor for high curing quality.

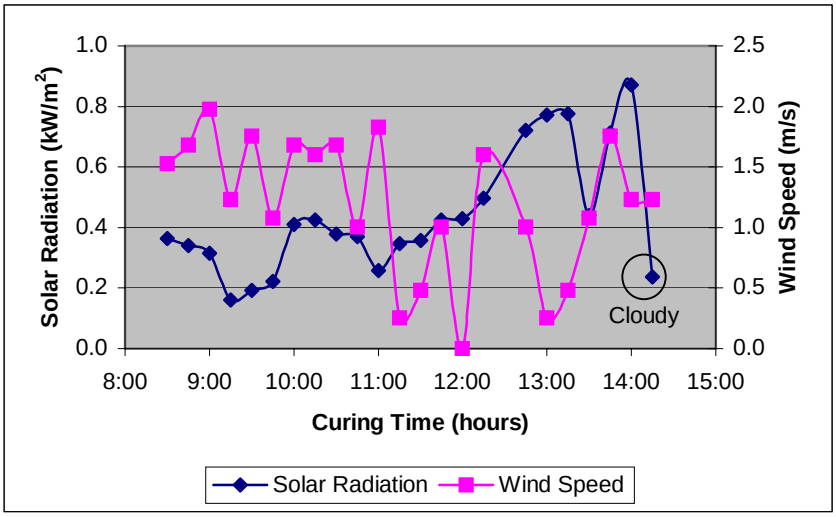

(a)

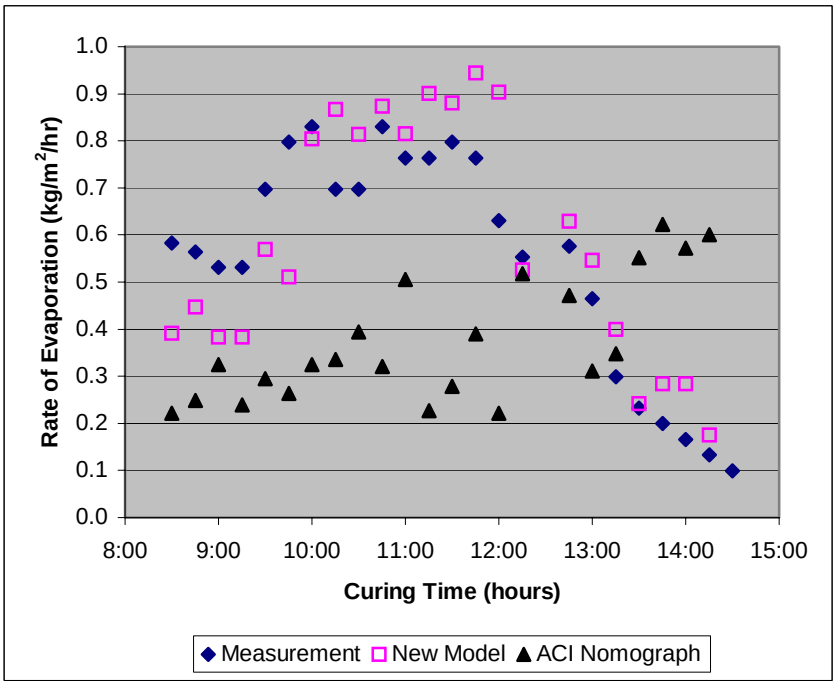

(b)

Figure 4-12 Validation of New Evaporation Model at Field: (a) Solar Radiation and Wind Speed Measured by Weather Station; (b) Comparison of Rate of Evaporation among Measurement, New Model, and ACI Nomograph.

None of the existing evaporation models were suitable to predict the evaporation of concrete after bleeding because they were developed based on an evaporation condition that is consistent with a continuous layer of water on the concrete surface. A modified version of Penman's model was prescribed on the basis of the drying characteristics of concrete after bleeding. The largest difference from the original

Penman's model was reflected in the drying characteristics of the concrete in predicting evaporation. Also, the surface moisture emissivity was characterized by a series of experiments. The surface moisture emissivity was found to be a function of effective curing thickness and wind speed. Another difference involves the adjustment of the solar radiation effect by the effective curing thickness. The modified Penman's model will allow for improved prediction of the amount of evaporation at a concrete pavement and evaluation of the method of curing.

CHAPTER 5
EVAPORATION INDUCTED CRACKING IN CONCRETE PAVEMENTS

INTRODUCTION

Previous research has shown that an understanding of the distribution and history of moisture at an early age is important relative to the quality of curing and its effect on delamination and spall potential. Its prediction is an inevitable task that must be achieved for a realistic estimation of drying shrinkage, thermal expansion, strength, maturity, and curing efficiency. Although some experimental data have been assembled over many years of research, little data at early ages of drying concrete are presently available.

One aspect of the effect of moisture in concrete pavement can be reflected in the countering effects of drying shrinkage versus that of creep behavior. These behavioral traits are of interest particularly in an early-age concrete with respect to slab deflections and formation of early-aged cracking or development of delamination in bonded concrete overlay systems. Material-related moisture properties (permeability, diffusivity, slope of the moisture isotherm, etc.) of concrete play a key role in the mathematical modeling and representation of stress and strain due to the net effect of drying shrinkage and creep strains under varying humidity conditions. Material tests are necessary to determine these pertinent material properties. Moisture transport models that represent the variation of moisture with time use these properties. In terms of engineering applications, prediction of humidity and diffusivity are important in consideration of spalling, warping, and other moisture-related stresses, strains, and deformations induced in concrete pavements.

Early-aged warping behavior is the main concern and probable cause of relatively high shear stresses that cause delamination in the vicinity of the slab corner or along slab edges. These delaminations are typically shallow and often develop into spalls (Huang, 1993). Spalling is here referred to as the breakdown or dislodging of concrete segments along a joint or crack in a concrete slab within 0.3 m (1 ft) of a joint or crack (Wang and Zollinger, 2000) that can affect the functional and structural integrity of the slab. The shear stresses previously referred to primarily develop from large moisture gradients causing a shearing action due to the gradient effect (Figure 5-1). The development of the gradient is

due to evaporation as a function of the ambient temperature and curing conditions during and after placement of the concrete (shown previously in Figure 4-1). Typically, the delamination is relatively shallow in depth (Figure 5-2) and occurs at an early concrete age when stresses caused by the moisture variation surpass the concrete shear strength. Significant spalling is unlikely to occur where the delaminations are not formed. In the event that they are formed, their extension into spalling appears to be by fatigue due to wheel loads and to some extent temperature fluctuations.

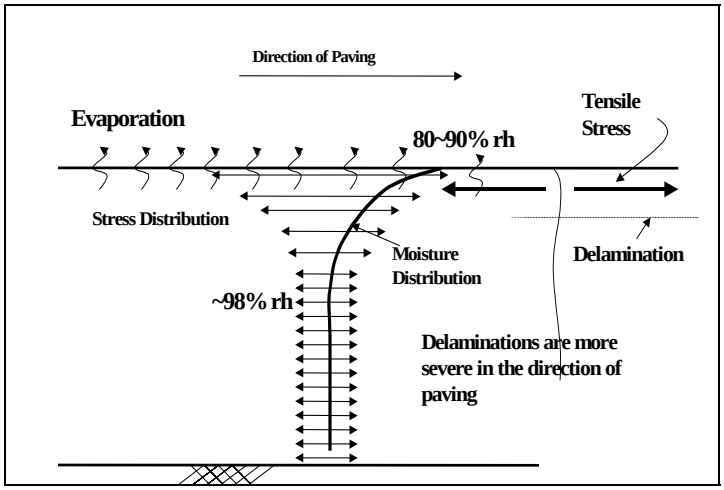

Figure 5-1 Formation of Horizontal Delamination (Wang and Zollinger, 2000)

Conditions necessary for formation of the delaminations include sufficiently low interfacial strength between the coarse aggregate and mortar, and sufficiently high evaporation of pore water from the hydrating concrete resulting in differential drying shrinkage induced shear stress near the pavement surface. Temperature variation also may be a factor in the development of the delamination shear fracture but is presumed not to be as large as the shrinkage contribution. Once delaminations have formed, they may extend later into spalls as a result of incompressibles, freeze-thaw cycles, traffic loading, and other effects of this sort.

Figure 5-2 Delamination in an Unspalled Concrete Core.

DELAMINATION DEVELOPMENT DUE TO MOISTURE PROFILES

Concrete tends to expand or contract slightly with a gain or a loss in moisture. Immediately after placement, the concrete may exhibit plastic shrinkage

as a result of loss of water by evaporation from the surface of the pavement. The plastic shrinkage induces tensile stress at the surface of the concrete and may result in surface cracking that is generally closely spaced, very tight, and penetrating only up to a couple of inches from the surface.

Contraction due to the loss of water from hardened concrete is referred to as drying shrinkage. Concrete exposed to the natural environment typically undergoes a certain amount of drying shrinkage that is comprised of both reversible and non-reversible components. Drying shrinkage is affected by the ambient relative humidity, aggregate content, volume to exposed surface ratio, and water to cement ratio of the concrete mix. In the opinion of the authors, approximately 15 to 20 percent of the ultimate shrinkage takes place within the first 2 to 3 weeks, and about 80 percent of the ultimate shrinkage takes place within 1 year for concrete exposed to air (Neville, 1996). In the construction of concrete pavement systems, drying shrinkage can be accommodated by the placement of sawcut joints or the development of random cracking. However, in addition to these effects, varying drying shrinkage vertically through the thickness of a concrete slab is of concern because of the potential for delaminations at an early age.

Delamination Modeling

Shear stress (or delamination stress) can be determined based on slab curling and warping behavior. Slab warping (mainly driven by differential drying shrinkage) can occur in two stages as denoted by Tang et al., (1993) delineated by separation of the slab corner from contact (i.e., liftoff) with the subgrade versus where the slab is in contact with the subgrade (i.e., zero liftoff). A set of functions developed on this basis was formulated to determine either edge or corner deflection due to curling and warping. In assuming the following model form for deformation at a slab corner, a form similar to that used by Tang et al. (1993) was adopted as:

$$w = \frac{\left(A_1 \cos x + A_2 \sin x\right)\left(B_1 \cos y \cosh y + B_2 \sin y \sinh y\right)}{e^x} \qquad (5\text{-}1)$$

where

$$y = \frac{Y}{\ell}$$

x $= \frac{X}{\ell}$

Y = distance from slab corner along the transverse joint

X = distance from slab corner along the longitudinal joint

A_i, B_i = function coefficients

Medium-thick plate theory provided the basis for several boundary conditions that were considered in the development of the coefficient equations and are summarized in Table 5-1. Two sets of solutions of the coefficient equations were developed depending whether the bottom of the slab was in contact with the subgrade or base support. A non-contact condition is referred to hereafter as liftoff, where a contact condition is referred to as a zero liftoff condition. The coordinate system adopted for the corner curling and warping model is shown in Figure 5-3. Several parameters listed above and their definitions are explained in Table 5-2. Since some of the coefficients are not independent of one another, evaluation of them should be accomplished using an appropriate numerical method to interactively calculate the coefficients. Curling and warping curvature within the x-y plane was modeled by deriving the curling and warping deformation model with respect to x and y (equations (5-1 and 5-2)).

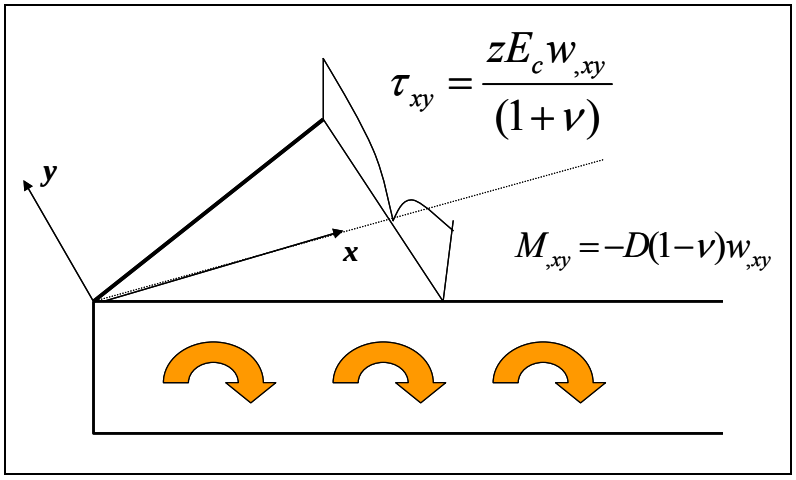

Figure 5-3 Coordination of Corner Curling and Warping Deformation Model (Wang and Zollinger, 2000).

$$w_{,xy} = \frac{[\cos x(A_2 - A_1) - \sin x(A_2 + A_1)][(B_2 - B_1)\sin y \cosh y + (B_2 + B_1)\cos y \sinh y]}{e^x \ell^2}$$

The coefficients substituted into the curling and warping curvature model can be used to determine the twisting moment (M_{xy}) and the shear or delamination stress (τ_{xy}) derived from plate theory as:

Table 5-1 Corner Curling and Warping Curvature Coefficients**.**

$$w_{,xy} = \frac{[\cos x(A_2 - A_1) - \sin x(A_2 + A_1)][(B_2 - B_1)\sin y \cosh y + (B_2 + B_1)\cos y \sinh y]}{e^x \ell^2}$$

Zero Liftoff Case	**Liftoff Case (** $0 > x \le s$ **)**
$A_1 = T_R A_2$	$A_1 = T_R A_2$
$A_2 = \dfrac{w_0}{B_1 - \nu B_2 T_R}$	$A_2 = \dfrac{e^s\left(w_0 - \dfrac{w_c s^3}{3\ell^2}\right)}{\nu B_2 \sin s + B_1 \cos s - T_R(B_1 \sin s + \nu B_2 \cos s)}$
$B_1 = 1$	$B_1 = 1$
$B_2 = B_1 \dfrac{T_R + 1}{T_R - 1}$	$B_2 = \dfrac{\dfrac{w_c x^2 e^x}{2A_2} - B_1\left[C_2 + T_R C_1\right]}{C_1 - T_R C_2}$

Note:

(1) $T_R = \dfrac{1 + \tan\dfrac{W}{2\ell}}{1 - \tan\dfrac{W}{2\ell}}$; W = slab width

(2) $w_0 = A_0(1+\nu)\ell^2$; $A_0 = \dfrac{\varepsilon}{h}$; $\varepsilon = \alpha\Delta T_{eq} + \varepsilon_\infty \Delta(1 - H^3)_{eq}$; $w_c = -\dfrac{\rho h}{k}$

(3) $C_1 = \cos s - \sin s$

(4) $C_2 = \cos s + \sin s$

(5) $s = \dfrac{S}{\ell}$; S = length of liftoff$= -\ln\left[\dfrac{w_c}{B_1 A_2\left(T_R \cos s + \sin s\right)}\right]\ell$

$$M_{xy} = -D(1-\nu)w_{,xy}$$

$$\tau_{xy} = \frac{E_c z}{1+\nu} w_{,xy} \qquad (5\text{-}2)$$

where

D = flexural rigidity of the slab

$$= \frac{Eh^3}{12\left(1-\nu^2\right)}$$

E_c = concrete modulus of elasticity

z = distance from the middle surface of the slab

υ = Poisson's Ratio

Table 5-2 Key Parameters of Corner Curling and Warping Coefficient Equations.

Parameters	Symbols
Ultimate Concrete Shrinkage	ε_∞
Concrete Humidity	H
Coefficient of Thermal Expansion	α_T
Concrete Temperature	T
Slab Thickness	h
Slab Width	W
Concrete Poisson Ratio	ν
Radius of Relative Stiffness	ℓ
Dimensionless Length of Liftoff	s
Edge Gap	w_0

Probability of Delamination

The probability of delamination can be formulated using equations 5-1, 5-2, and that given in Table 5-1 in terms of the probability that the shear stress (τ) will exceed the shear strength (f_τ):

$$prob\left(\tau - f_\tau > 0\right)$$

Assuming the difference τ - f_τ is normally distributed, its associated normal standard deviate can be formulated as:

$$z = \frac{\tau - f_\tau - 0}{\sqrt{VAR(\tau) + VAR(f_\tau)}}$$

The variance of shear strength (VAR(f_τ)) is given by:

$$VAR\left(f_\tau\right) = \left(COV\left(f_\tau\right) \cdot \overline{f_\tau}\right)^2$$

The variance of shear stress (VAR (τ)) is formulated from the first order, second moment method:

$$VAR\{\tau\} = \sum_i \left[\frac{\partial \tau}{\partial X_i}\right]^2 VAR\left(X_i\right) + \sum_j \sum_k \frac{\partial \tau}{\partial X_j} VAR\left(X_i\right) \frac{\partial \tau}{\partial X_k} VAR\left(X_k\right) \rho_{ij}$$

where

X_i = variance factor (E_c, A_0)
ρ = correlation factor (which is = 0 in this instance)
A_0 = previously defined

Developing further:

$$VAR(\tau) = \left(\frac{\partial \tau}{\partial E_c}\right)^2 VAR(E_c) + \left(\frac{\partial \tau}{\partial A_0}\right)^2 VAR(A_0)$$

where

$$\frac{\partial \tau}{\partial E_c} = \frac{z}{1+\upsilon}\left(w_{,xy} + z\frac{\partial w_{,xy}}{\partial E_c}\right)$$

and setting

$$w_{,xy} = \frac{[\cos x(A_2 - A_1) - \sin x(A_2 + A_1)][(B_2 - B_1)\sin y \cosh y + (B_2 + B_1)\cos y \sinh y]}{e^x \ell^2} = \frac{X_c}{e^x \ell^2}$$

then

$$\frac{\partial w_{,xy}}{\partial E_c} = e^{-x}\frac{x}{4E_c\ell^2}X_c - 2e^{-x}\frac{1}{4E_c\ell^2}X_c + e^{-x}\frac{1}{\ell^2}\frac{\partial X_c}{\partial E_c}$$

where

$$\frac{\partial X_c}{\partial E_c} = \left\{\cos(x)\frac{\partial A_2}{\partial E_c}(1 - T_R) + \sin(x)\frac{x}{4E_c}(A_2 - A_1) + \cos(x)\frac{x}{4E_c}(A_2 + A_1) - \sin(x)\frac{\partial A_2}{\partial E_c}(1 + T_R)\right\}$$
$$\cdot\left\{(B_2 - B_1)\sin(y)\cosh(y) + (B_2 + B_1)\cos(y)\sinh(y)\right\} + \left\{\cos(x)(A_2 - A_1) - \sin(x)(A_2 + A_1)\right\}$$
$$\cdot\left\{\begin{array}{l}\frac{\partial B_2}{\partial E_c}\sin(y)\cosh(y) - \cos(y)\cosh(y)\frac{y}{4E_c}(B_2 - B_1) - \sin(y)\sinh(y)\frac{y}{4E_c}(B_2 - B_1) + \\ \frac{\partial B_2}{\partial E_c}\cos(y)\sinh(y) + \sin(y)\cosh(y)\frac{y}{4E_c}(B_2 + B_1) - \cos(y)\cosh(y)\frac{y}{4E_c}(B_2 + B_1)\end{array}\right\}$$

$$\frac{\partial A_2}{\partial E_c} = \frac{1}{B_1 - \upsilon B_2 T_R}\frac{\partial w_0}{\partial E_c};\quad \frac{\partial w_0}{\partial E_c} = 2A_0\frac{\ell^2}{2E_c} = \frac{w_0}{2E_c}$$
$$\frac{\partial A_2}{\partial E_c} = \frac{w_0}{B_1 - \upsilon B_2 T_R}\frac{1}{2E_c}$$
$$\frac{\partial A_1}{\partial E_c} = T_R\frac{\partial A_2}{\partial E_c}$$

$$\frac{\partial B_1}{\partial E_c} = 0;\ \frac{\partial B_2}{\partial E_c} = B_1\left(\frac{\frac{\partial T_R}{\partial E_c}}{T_R - 1} - \frac{T_R + 1}{(T_R - 1)^2}\frac{\partial T_R}{\partial E_c}\right)$$

$$\frac{\partial T_R}{\partial E_c} = \left(\sec\left(\frac{W}{2\ell}\right)\right)^2 \frac{W}{8\ell E_c}\left[1 + \frac{\tan\left(\frac{W}{2\ell}\right)}{\left(1 + \tan\left(\frac{W}{2\ell}\right)\right)^2}\right]$$

$$\frac{\partial \tau}{\partial A_0} = z\frac{E_c}{1+\upsilon}\frac{\partial w_{,xy}}{\partial A_0}$$

$$\frac{\partial w_{,xy}}{\partial A_0} = \frac{e^{-x}}{\ell^2}\frac{\partial A_2}{\partial A_0}\{\cos(x) - \sin(x)\}\{(B_2 - B_1)\sin(y)\cosh(y) + (B_2 + B_1)\cos(y)\sinh(y))\}$$

$$\frac{\partial A_2}{\partial A_0} = \frac{(1+\upsilon)\ell^2}{B_1 - \upsilon B_2 T_R}$$

$$VAR(E_c) = (COV(E_c)\cdot E_c)^2$$

$$VAR(A_0) = \left(\frac{1}{h}\right)^2 VAR(\varepsilon_{env}) = \left(\frac{1}{h}\right)^2 (COV(\varepsilon_{env})\overline{\varepsilon_{env}})^2$$

ε_{env} = strain due to moisture and temperature gradient in the slab

The probability of delamination is based upon the difference between the shear strength and the shear stress and is used to differentiate between delamination and non-delamination conditions.

Sensitivity of Moisture to Delamination Stress

As a means to illustrate the factors that affect delamination distress, a limited sensitivity study was conducted using analysis from the TMAC[2] program and the delamination model. The sensitivity of moisture profiles to delamination stress was examined in two parts — one part by fixing key parameters at reasonable and typical levels. Temperature and moisture-related parameters were varied over a selected range in the analysis to examine their effect on the delamination stress development. The set values

of the parameters used in the sensitivity study are summarized in Table 5-3 (for an early age concrete). The parameters that were varied were:

- Equivalent Linear Humidity Difference Coefficient ($\Delta(1\text{-}H^3)_{eq}$)
- Equivalent Linear Temperature Difference (ΔT_{eq})
- Ultimate Concrete Shrinkage (ε_∞)
- Coefficient of Thermal Expansion (α_T)

Delamination stress is affected by moisture profiles in the concrete as shown in Figure 5-4 (a). The delamination stress increases with an increase of the equivalent linear humidity difference coefficient ($\Delta(1\text{-}H^3)_{eq}$) (Vepakomma et al., 2002). Because a larger humidity difference coefficient is calculated by larger changes in concrete moisture profiles, the potential for delamination will be greater. Delamination stress under liftoff conditions are much larger than for zero liftoff conditions. Sensitivity of temperature difference on the

Table 5-3 Typical Values of Parameters of Delamination Model.

Parameters	Values
Slab Thickness (h)	25.4 cm (10 inch)
Slab Width (W)	3.66 m (12 ft)
Concrete Elastic Modulus (E_c)	20.7 GPa (3000 ksi)
Concrete Poisson Ratio (ν)	0.15
Modulus of Subgrade Reaction (k)	27.1 MN/m^3 (100 psi/in)
Delamination Depth ($h/2\text{-}z$)	25.4 mm (1 inch)

delamination stress also was examined as shown in Figure 5-4 (b) and compared to its sensitivity to moisture difference. For this analysis, the maximum temperature gradient has been assumed to be about 0.66 ^{o}C/cm (3^{o}F/inch) during daytime and about 0.22 ^{o}C/cm (1 ^{o}F/inch) during nighttime. Thus, the largest equivalent linear temperature difference for 25.4 cm (10 inch) thick pavement was assumed to be 16.7 ^{o}C (30 ^{o}F). As compared in Figure 5-4, moisture effect on the delamination stress development is much larger than the temperature effect. Ultimate drying shrinkage of concrete and to some extent the (CoTE) have effects on the delamination stress as shown in Figure 5-4 (c) and (d), respectively, although the effects were smaller than moisture or temperature difference effects. The minimum and maximum ultimate shrinkage strain and CoTE values were assumed to be

400 and 1200 micro-strains, and 6 and 14 micro-strains/°C, respectively. Slab width, subgrade reaction modulus, and ratio of delamination depth to slab thickness, also have an effect on the magnitude of delamination stress.

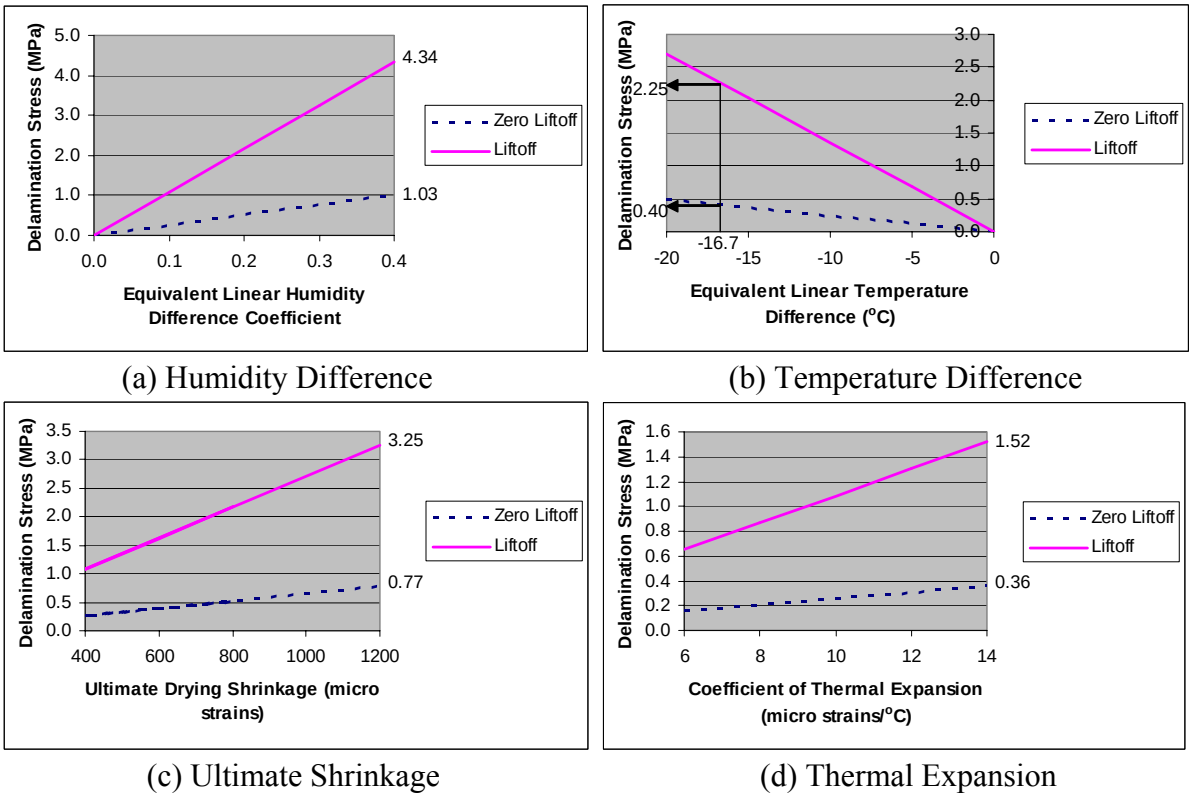

(a) Humidity Difference (b) Temperature Difference

(c) Ultimate Shrinkage (d) Thermal Expansion

Figure 5-4 Sensitivity Study for Delamination Stress.

Wind Speed, Curing Quality, and Aggregate Bond

The second part of this analysis focuses on other key factors affecting the formation of delamination of wind speed, curing quality, and aggregate bond strength. The evaporation depends to a large extent on the speed of the wind over the evaporating surface. Wind replaces the air over a hydrating concrete surface that tends to become gradually saturated with water vapor. If this air is not continuously replaced with drier air, the driving force for evaporation decreases.

As the surface of the concrete dries, a moisture gradient develops typically in the top 7.6 cm (3 inch) of the concrete, which exposes concrete pavement to delamination stress. Analysis of wind effect on moisture distribution was conducted by use of the

TMAC^2 program. High wind speed of 15 mph and low wind speed of 5 mph were selected in the analysis and other inputs were consistent with the field data collected from the US 59 test section reported in Appendix C. For a 5 mph wind speed condition, there is no obvious crossover between strength and delamination over time as shown in Figure 5-5. For a 15 mph wind condition, however, the strength is exceeded at the time of 10 hours after placement.

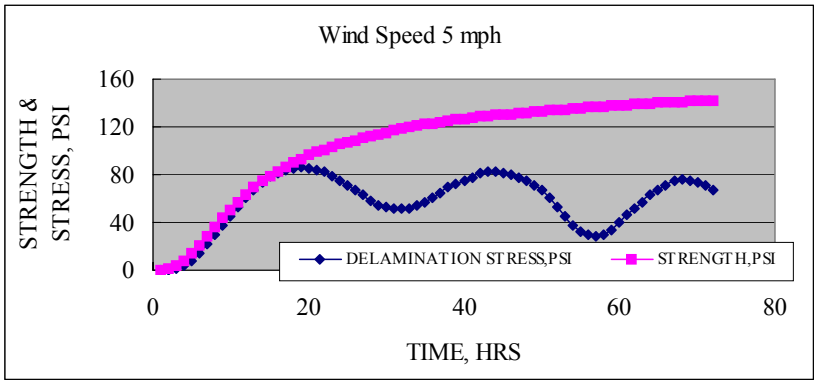

(a) Wind Speed of 5mph

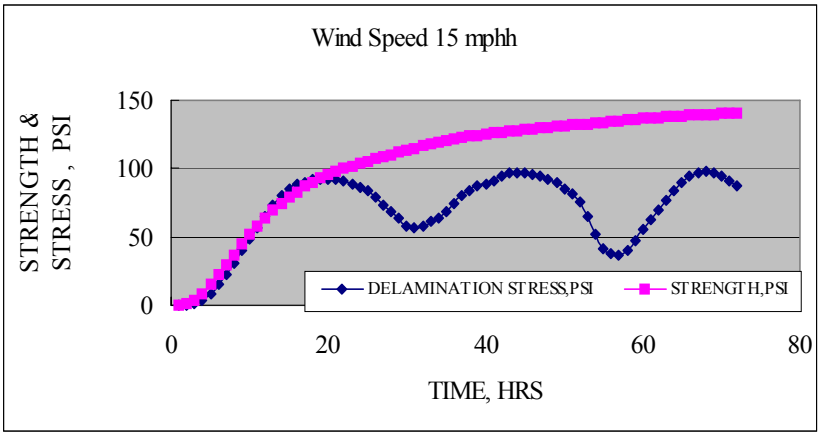

(b) Wind Speed of 15mph

Figure 5-5 Effect of Wind Speed on Delamination Stress.

Quality curing can effectively prevent moisture from evaporating from inside the concrete to the ambient air above it. The curing media works to seal the moisture below the concrete pavement surface. As stated before, effective curing thickness (ECT) is a useful index to evaluate curing quality. Laboratory testing data indicated that surface humidity, which is an important boundary condition for moisture analysis, is a function of ambient relative humidity, wind speed, and effective curing thickness.

A similar TMAC^2 analysis as shown in Figure 5-5 was carried out again to evaluate the impact of curing quality on delamination. An average of 2.5 cm (1 inch) and 5.1 cm (2 inch) effective thickness was used in the TMAC^2 analysis, and a wind speed of 15 mph was used to illustrate the effects of these parameters. For a 5.1 cm (2 inch) ECT, there was no

obvious crossover between strength and the delamination stress. However for a 2.5 cm (1 inch) ECT, the shear strength of the concrete was exceeded at the time of 10 hours after placement. This result indicates proper curing application can reduce the probability of delamination as illustrated in Figure 5-6, which compares the probability of the delamination among all the cases considered in the analysis (two levels of bond strengths of 350 and 700 $psi\sqrt{in}$ representing the bond provided by gravel and limestone aggregates, respectively and two values of ECT: 1 and 2 inches representing low and high curing quality). It is clear that low bond strength aggregates and curing that averages an ECT of 2.5 cm (1 inch) or less will experience a high probability of delamination which will translate into a high percentage of pavements suffering spall damage. Coarse aggregates manifesting a higher bond strength experience a lower probability of delamination but not if the wind speed during placement is too high. Prior to discussion of the specification for curing effectiveness, some explanation of the aggregate bond strength is presented.

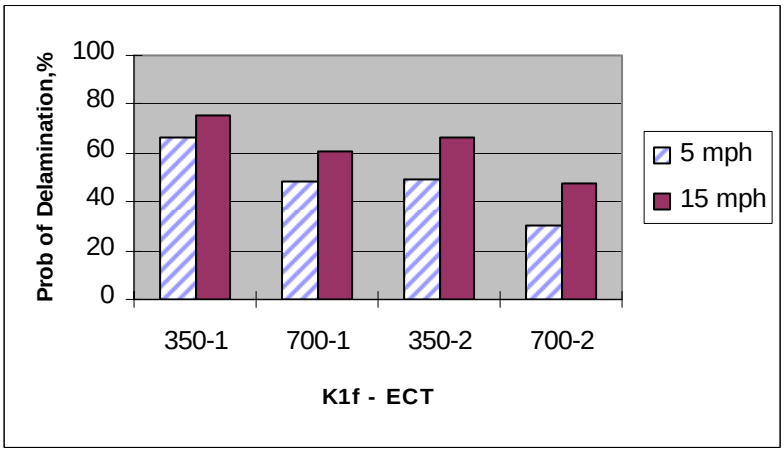

Figure 5-6 Probability of Delamination.

Aggregate Bond Strength

The most significant factor affecting delamination and eventual spalling is the early strength of the bond between the coarse aggregate and the mortar. Although up until recently difficult to measure and quantify, the aggregate-mortar bond is of prime importance in the development of concrete strength, especially strength related to the tensile capacity of the concrete. Normally this only involves the coarse aggregate, rather than the fine aggregate. The tensile strength can have a very significant role in the amount of spalling that occurs. Presently it is considered that the factors that mostly affect this bond include non-aggregate properties such as water-to-cement ratio, cement type, age, and compaction to reduce air voids. However, it is believed that absorption capacity,

mineralogical composition, and surface texture and shape of aggregates also influence the bond between the paste and the aggregate (Mindess, 1981; Farran, 1956).

Nonetheless, no recognized test exists to measure this property directly, but recent developments are available to measure aggregate properties related to the fracture resistance of concrete. Conducted at an early age where the crack passed between the aggregate and the mortar, the fracture characteristics of concrete serve as a measure of the bond strength in addition to other factors important to bond such as shape and surface texture of the aggregate. Recent developments using fracture mechanics strength theories have resulted in new approaches, specimen geometries, and strength parameters that have allowed the determination of the strength of concrete as well as the aggregate-mortar bond based on those theories.

A test procedure (Figure 5-7) suggested by the RILEM Committee on Fracture Mechanics (1990) to determine the fracture properties of toughness and brittleness of a concrete mixture uses beam type specimens that range in size depending upon the loaded span. The fracture model that has been associated with the RILEM procedure is referred to as the Size Effect Law (SEL). SEL involves two fracture parameters: fracture toughness (K_{If}) and the process zone length (c_f, i.e., the brittleness factor) that may be interpreted to reflect the aggregate-mortar bond of early-age concrete. SEL suggests that the determination of K_{If} and c_f is found from testing several beam specimens of different sizes as indicated in the RILEM procedure. The strength parameters K_{If} and c_f have been used to characterize early-age concrete strength. Recently, new test method using a modified split tensile specimen based on SEL has been suggested. This method determines K_{if} and c_f from specimens of the same size (i.e., diameter) providing for a greater amount of convenience in specimen preparation. The various configurations

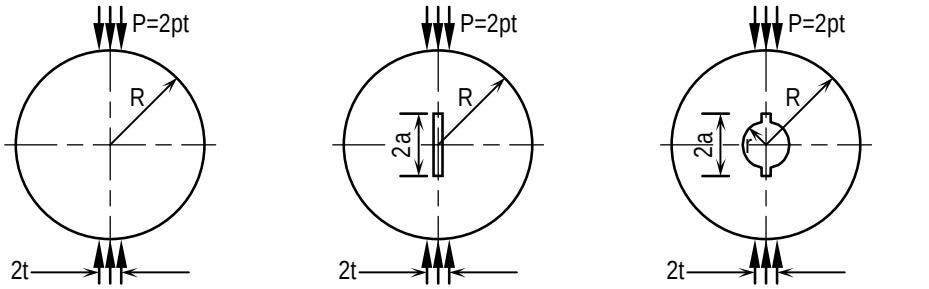

(a) Zero-notch (b) Notched (c) Notched with a hole

Figure 5-7 Split Tension Cylinders.

illustrated in Figure 5-7 are utilized in order to enhance the accuracy of the test method relative to specimen geometry effects.

Cylindrical specimens commonly are used for QC/QA purposes since they have the advantage of being easily cast or cored from pavement structures. The split tension of concrete cylinders, also known as the Brazilian disk test, is a standardized ASTM test method (ASTM C 496) typically used to obtain concrete tensile strength (Figure 5-7 (a)). In order to evaluate the fracture parameters, modified split tensile specimens are needed as shown in Figures 5-7b and 5-7c. A notch is needed in the test specimen shown in Figure 5-7 (b). A test specimen as shown in Figure C is needed to provide a required geometrical configuration represented by special functions noted as $F(\alpha)$, $g(\alpha)$, and $g'(\alpha)$. A small modification of the cylinder such as a hole drilled at the specimen center (Figure 5-7 (c)) dramatically improves the accuracy of these functions.

Assuming that the cylinder specimen length (b), diameter (d), and the crack lengths ($2a_o$) will always be the same for a standardized procedure, the only input necessary for the determination of the fracture parameters is the maximum applied load for each of the three different specimens. From fracture mechanics theory, the fracture parameters fracture toughness, K_{If}, and the fracture process zone length, c_f, can be determined. With the fracture parameters identified, the following expression is used to calculate the tensile strength of concrete:

$$\sigma_N = c_n \frac{K_{If}}{\sqrt{g'(\alpha_o)c_f + g(\alpha_o)d}}$$

The factor c_n is a geometry factor that varies depending on structure type and for a concrete pavement is a function of the radius of relative stiffness. σ_N is calculated as a function of the crack ratio (α - which is the percent of crack growth) and the fracture parameters. The fracture parameters are obtained from the cylindrical specimens as explained above and will vary according to aggregate type, shape, and texture.

Specification for Curing Quality (Appendix E)

A proposed specification for curing quality is provided in Appendix E on the basis of the results shown in Figure 5-6. This itemized specification is categorized with respect to coarse aggregate bond strength (in terms of fracture toughness – K_{1F}), wind speed, and

the required minimum effective curing thickness to prevent delamination at a 50 percent level of probability. The aggregate bond strength is referred to as concrete age of 1 day based on the test method previously described. The specification is divided at a wind speed of 10 mph where the ECTs for the greater than 10 mph group are nominally separated by 0.2 cm (0.5 inch) from the less than 10 mph group. The ECTs range from 0.1 cm to 0.4 cm (2.5 inch to 1.0 inch) for ambient relative humidities less than 80 percent and are set depending on the bonding characteristics of the coarse aggregate type.

Spalling Distress Mechanism

Spalling, whether traffic or freeze-thaw induced, typically occurs at random cracks and occasionally at joints subjected to high delamination stresses during and shortly after construction. The incidence of this distress type is strongly correlated to pre-existing horizontal delaminations that occur within 25 mm (1 inch) of the pavement surface and can later grow into a spall due to a variety of causes ranging from accumulation of incompressibles within the joint or crack, freeze-thaw cycles, to application of repeated shear loads induced by passing traffic.

Tang et al. (1993) introduced a spalling stress model to predict spall stress caused by passing wheel loads. The Tang model for spall stress (σ_t) is most easily described in Figure 5-8 with a modification from the original expression to account for tensile stress effects due to vertical shear on the crack face due to load transfer. As can be observed in Figure 5-8, several key parameters are included in the model and are re-defined as:

$$\sigma_t = \frac{1}{\sin\theta}\left[(\tau - \tau_f)\frac{l}{t} + \frac{\tau_f}{\tan\theta} + \frac{\sigma_{js}}{t}\right] + \frac{6M}{t^2} \qquad (5\text{-}3)$$

where

τ = shear stress from tire loading (≈ 170 kPa (25 psi))

τ_f = friction resistance at bottom of spall

l = length of spall (can be assumed to be 15 cm (6 inch))

t = depth of spall

θ = angle of spall fracture (can be assumed to be 60 ^{o})

σ_{js} = compressive stress caused by the joint sealant (= $k_s u$)

k_s = stiffness of the joint sealant (= $E_{sealant}$/depth of sealant)

u = thermal displacement of the joint sealant

M = spall bending moment due to shear from load transfer effects

Discussion of the details related to the development of equation (5-3) are limited in this report since they are presented elsewhere (Zollinger et al., 1994), but an average value for the length of spall is suggested based on severity levels to simplify the stress analysis even though variations from this may be observed in field studies.

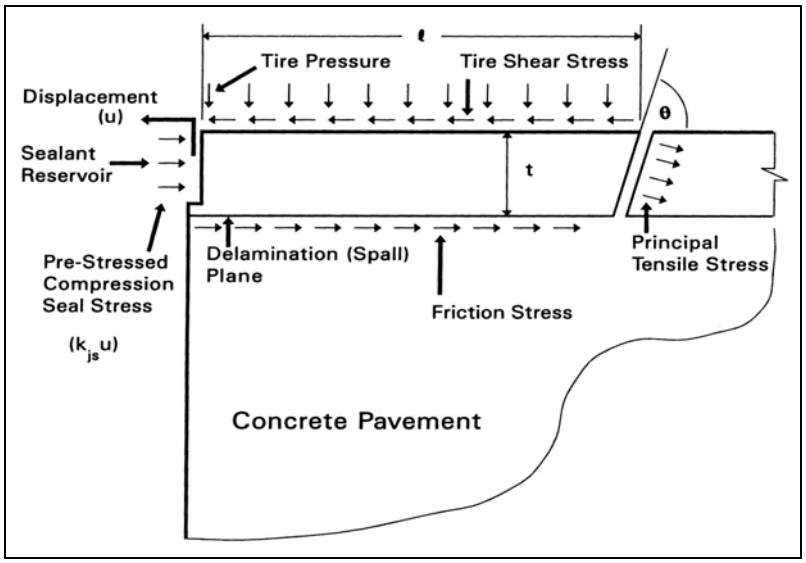

Figure 5-8 Concrete Pavement Spall Mechanism and Model (Tang et al., 1993).

The first term in equation (5-3) typically makes a small contribution to the tensile stress since the shear stress from passing wheel loads rarely exceeds the frictional resistance along the delamination. The most significant contributor to the stress predicted by equation (5-3) is the moment component, which is a function of the degree of load transfer as the joint or crack opens and closes, and the shear stiffness of the joint sealant. A bending moment is induced due to the combined effect of the shear component and the leverage arm '*l*'. The shear component consequently can be determined as an average of two parts, one due to load transfer and the other due to the transfer of shear strain through the joint sealant material. The net effect of this average is that high bending moments can be generated at both low and high load transfer conditions. The movement associated with this shear effect also has some effect on the shear resistance along the bottom face of the spall boundary (which defines the depth of delamination). Delamination depths greater than 40 to 50 mm

(1.5 to 2.0 inch) are not expected or predicted to develop into spall distress, even though deeper spalls would certainly not be any more tolerable.

CHAPTER 6
CONCLUSIONS AND RECOMMENDATIONS

This report documents a spalling mechanism that explains how climatic conditions, material properties, mixture designs, and construction methodology are tied together and combine to create situations that result in delamination and eventual spalling distress. It is evident that moisture, as measured by the relative humidity of the pore water, in concrete affects it both thermally and hydrally. The thermal effects are manifest in the increased CoTE value between 70 and 100 percent pore relative humidity and in the temperature cooling due to the heat of vaporization and the evaporation effect on the surface of the concrete. These effects are important to account for in the modeling of concrete pavement climatically in order to accurately portray the effect of concrete materials and aggregates on rigid pavement behavior.

Another important aspect relative to the modeling of moisture movement in concrete is the accurate assessment of the transport properties of concrete to provide appropriate accountability for the diffusion processes taking place during the hardening and curing period. Thermal conductivity and moisture diffusivity change with time, degree of hydration, and the moisture content of the concrete. These key properties are represented in the modeling process by sophisticated models that diminish these key characteristics as a function of the degree of hydration that can be calibrated based on available test data for a particular mixture of concrete. Thermal and moisture transport are mixture dependant and need defining in terms of mixture characteristics. The parameters of these models conceivably can be represented by mixture and material-based parametric equations that would undoubtedly improve the generality of these transport models in the modeling process.

To this end, a two-dimensional finite element program TMAC^2 has been developed to predict the moisture and temperature profiles of a concrete pavement in specified environmental conditions and simultaneously account for these important factors and concrete pavement performance. Darcy's Law was used as a governing equation of moisture diffusion in TMAC^2 to model the moisture profiles. Moisture diffusivity was back-calculated using moisture profile data collected from a test slab instrumented in this

project where dew point and dry bulb temperature data were collected on an hourly basis. The back-calculated moisture diffusivity showed very high values at the initial stage of concrete curing and stabilizes to small values as time passes. A model for the moisture diffusivity was used in the calculation of relative humidity. Surface humidity modeled from a laboratory test was used as the boundary condition, and the initial condition was considered. Calculated moisture profiles corresponded to the measured data. The measured initial relative humidity was significantly low, and it increased steadily until around 20 hours after placement because of high initial diffusivity and saturation values.

Curing condition is also a key player in concrete pavement performance and need to be adequately represented in the boundary conditions of the modeling process. The capability of a curing membrane to prevent evaporation is represented by the effective curing thickness, which is the equivalent thickness of concrete to accomplish the same amount of protection against moisture loss as the curing membrane provides. The ECT can be determined from three relative humidity readings taken above, at, and below the concrete surface and is consequently sensitive to wind conditions. Declining or low values of this parameter (on the order of 2.54 cm [1 inch]) serves as an early warning for adverse conditions that may result in delamination. Prototypes of the curing monitoring system (CMS) were developed and test run on several occasions as a means of monitoring the curing quality during the early stages of hardening. This device shows potential in providing a real-time measurement of curing quality and its effectiveness along with a measure of the moisture-based maturity. Specifications for construction were prepared in terms of the ECT in terms of concrete aggregate types (relative to its bond strength) and the wind conditions at the time of construction.

Incorporating a higher quality of curing for a concrete pavement reduces the gradient of moisture profile, which results in a significant decrease in equivalent linear relative humidity difference through the depth of the pavement. The decreased equivalent linear relative humidity difference influences the substantial amount of strain reduction and decreases vertical displacement due to curling and warping. Furthermore, the reduced moisture profile gradient at an early age affects a decrease of shear (delamination) stress and for a given aggregate type, the incidence of spalling distresses along joints or cracks in the pavement at later ages.

RECOMMENDATIONS

Several recommendations from this study can be made but a primary one is the development of a curing specification for improved curing of concrete pavement construction. A draft specification is listed in Appendix E developed under this project specifically written to minimize the incidence of delamination. A specification for improved curing may also need to be focused on the aggregate used in the concrete and applied according to the wind conditions at the time of curing. The CMS is designed to facilitate the implementation of a specification of this nature in the construction process.

The second recommendation is the development and advancement of moisture-based maturity as acceptance criteria for concrete paving construction. Limits will need to be established but can be selected in accordance with requirements spelled out in the specification for improved curing.

The third recommendation centers on the further development of the moisture-adjusted CoTE for the determination of cracking intervals for the design of CRC pavement in Texas and the associated longitudinal steel percentage. This is an important consideration in stress development and the effect of the depth of cover since the moisture affects apply mainly to the concrete in the top 7.6 cm (3 inch) of the pavement.

The fourth recommendation refers to the inclusion of the TMAC^2 routine to include the assessment of delamination and spalling distress in a version of the continuous reinforced concrete pavement (CRCP) analysis program. This also should include a modification for the CoTE and shrinkage considerations as well. Prediction of the vertical moisture profile in concrete pavement will add a very important parameter to appropriately assess the concrete strength within the top 7.6 cm (3 inch) of the pavement surface. This addition will provide for the determination of the moisture-based maturity and the adjustment for the concrete CoTE.

REFERENCES

ACI 305R-96, *Hot Weather Concreting*. Manual of Concrete Practice, Part 2, Farmington Hills, American Concrete Institute, 1996.

ASHRAE, *Handbook of Fundamentals.* American Society of Heating Refrigeration and Air Conditioning Engineers, New York, New York, 1972.

ASTM C 29. *Standard Test Method for Unit Weight and Voids Aggregates*. Annual Book of ASTM Standards, American Society for Testing and Materials, 1999.

ASTM C 192. *Standard Practice for Making and Curing Concrete Test Specimens in the Laboratory*. Annual Book of ASTM Standards, American Society for Testing and Materials, 1999.

ASTM C 496. *Standard Practice for Making and Curing Concrete Test Specimens in the Laboratory*. Annual Book of ASTM Standards, American Society for Testing and Materials, 1999.

ASTM C 1074. Standard Practice for Estimating Concrete Strength by the Maturity Method. *Annual Book of ASTM Standards*, American Society for Testing and Materials, West Conshohocken, Pennsylvania, 1999.

Bažant, Z.P., "Thermodynamic Theory of Deformations of Concrete with Explanation of Drying Creep." *American Concrete Institute Symposium on Designing for Effects of Creep, Shrinkage and Temperature*, SP 27, 1969.

Bažant, Z.P., "Constitutive Equation for Concrete Creep and Shrinkage Based on Thermodynamics of Multiphase Systems." *Materials and Structures*, Vol. 3, No. 13, pp. 3-36. 1970.

Bažant, Z.P. and L.J. Najjar. Nonlinear Water Diffusion in Nonsaturated Concrete. *Materials and Structures (RILEM)*, Vol. 5, No. 25, 1972.

Branco, F.A., R.A. Mendes, and E. Mirabell. Heat of Hydration Effects in Concrete Structures. *ACI Materials Journal*, Vol. 89, No. 2, pp. 139-145, 1992.

Buch, N. and D.G. Zollinger, "Preliminary Investigation on Effects of Moisture on Concrete Pavement Strength and Behavior." *Transportation Research Record 1382*, Transportation Research Board, National Research Council, Washington, D.C., pp. 26-31, 1993.

Carino, N.J., "Maturity Functions for Concrete." *Proceedings, RILEM International Conference on Concrete at Early Ages*, Ecole Nationale des Ponts et Chausses, Paris, France, pp. 111-115, 1982.

Chapman, A.J., *Fundamentals of Heat Transfer*. Macmillan Inc., New York, New York, 1982.

Chin, F.K., "Relation between Strength and Maturity of Concrete." *Journel of American Concrete Institute*, Vol. 68, No. 3, pp. 196-203, 1972.

Dalton, J., *Experimental Essays on Evaporation*. Literary and Philosophical Society of Manchester, Vol. 5, pp. 536-602, 1802.

Dempsey, B.J., W.A. Herlache, and A.J. Patel, "Climatic-Materials-Structural Pavement Analysis Program." *Transportation Research Record 1095*, Transportation Research Board, National Research Council, Washington, D.C., pp. 111-123, 1986.

Dilley, A.C., "On the Computer Calculation of Vapor Pressure and Specific Humidity Gradients from Psychometric Data." *Journal of Applied Meteorology*, Vol. 7, Aug. 1968.

Emborg, M., *Thermal Stresses in Concrete Structures at Early Ages*. Doctoral Thesis, Lulea University of Technology, Sweden, 1989.

Farran, I., "Contribution Mineralogique a l'Etude de l'Aderence entre les Constiuants Hydrates des Cements et les Materiaux Enrobes [Mineralogical Study of the Bond between Hydrated Cement and Aggregate]," *Revue des Materiaux de Construction*, No. 490-491, pp.155-172, 1956.

Freiesleben Hansen, P. and E.J. Pedersen, "Maturity Computer for Controlled Curing and Hardening of Concrete." *Nordisk Betong*, Stockholm, Sweden, pp. 464-470, 1977.

Hart, W.K., "The Effect of Moisture in Concrete," Bureau of Public Roads. Vol. 6, No. 1, (per p. 1-10), March 1925; Also Trans. ASCE, Vol. 84, 1926.

Hedlund, H. and G. Westman, "Evaluation and Comparison of Sealed and Non-Sealed Shrinkage Deformation Measurements of Concrete," *Autogenous Shrinkage of Concrete*, Tazawa, E., Edition. R&FN Spon, New York, pp. 123-134, 1999.

Hsieh, C.K., C. Qin, and E.E. Ryder, "Development of Computer Modeling for Prediction of Temperature Distribution Inside Concrete Pavements." *Rep. No. FL/DOT/SO/90-374*, Department of Mechanical Engineering, University of Florida, Gainesville, Florida, 1989.

Huang, C.L.D., "Multi-Phase Moisture Transfer in Porous Media Subjected to Temperature Gradient." *International Journal of Heat and Mass Transfer*, Vol. 22, No. 9, pp. 1295-1307, 1979.

Incropera, F.P. and D.P. DeWitt, *Fundamentals of Heat and Mass Transfer*. 4th edition, John Wiley and Sons, New York, 1996.

Janssen, D.J., "Moisture in Portland Cement Concrete." *Transportation Research Record 1121*, Transportation Research Board, National Research Council, Washington, D.C., pp. 40-44, 1987.

Jeong, J.H. and D.G. Zollinger, "Development of Test Methodology and Model for Evaluation of Curing Effectiveness in Concrete Pavement Construction." *Transportation Research Record*: *Journal of the Transportation Research Board 1861*, pp. 17-28, 2003.

Kaleidagraph. *Version 3.06*. Synergy Software, Reading, Pennsylvania, 1996.

Kapila, D., J. Falkowsky, and J.L. Plawsky, "Thermal Effects During the Curing of Concrete Pavements." *ACI Materials Journal*, Vol. 94, No. 2, Mar.-Apr. 1997.

Kasi, S.S.H. and S.E. Pihlajavaara, "An Approximate Solution of a Quasi-Linear Diffusion." *Publication No. 153*, The Station Institute for Technical Research, Helsinki, Finland, 1969.

Kaviany, M., *Principles of Convective Heat Transfer*. Springer-Verlag, New York, New York, 1994.

Kee, C.F., "Relation Between Strength and Maturity of Concrete." *Proc*., *ACI J*., Vol. 68, No. 3, pp. 196-203, 1971.

Klemens, P.G., *Theory of the Thermal Conductivity of Solids*. Academic Press, London, England, 1969.

Kohler, M.A., T.J. Nordenson, and W.E. Fox, *Evaporation from Pans and Lakes*. Research Paper, No. 38, U.S. Department of Commerce, Washington, D.C., May 1955.

Lew, H.S. and T.W. Reichard, "Prediction of Strength of Concrete from Maturity." *Accelerated Strength Testing*, SP-56, American Concrete Institute, Detroit, Michigan, 1978.

Lim, Seungwook, "Viscoelastic Age-Dependent Analysis of Restrained Shrinkage Stress Development in Early-Age Concrete." *PhD Dissertation*, Texas A&M University, December 2002.

Linsley, R.K., M.A. Kohler, and J.L. Paulhus, *Hydrology for Engineers*. 2nd edition, McGraw-Hill, New York, 1975.

McIntosh, J.D., "Electrical Curing of Concrete." *Mag. Conc. Res*., 1(1), pp. 21-28, 1949.

Meinel, A.B. and M.P. Meinel, *Applied Solar Energy: An Introduction.* Addison-Wesley, Reading, Massachusetts, 1976.

Menzel, C.A., *Causes and Prevention of Crack Development in Plastic Concrete*. Portland Cement Association Annual Meeting, pp. 130-136, 1954.

Meyers, S.L., "How Temperature and Moisture Changes May Affect Durability of Concrete." *Rock Products*, Vol. 54, No. 8, pp. 153-162, August 1951 .

Mindess, S. and J.F. Young, *Concrete*. Prentice-Hall, Inc., Englewood Cliffs, New Jersey, 1981.

Murray, F.W., "On the Computation of Saturation Vapor Pressure." *Journal of Applied Meteorology*, Vol. 6, Feb. 1967.

Neville, A.M., *Properties of Concrete*. 4th ed., John Wiley and Sons, New York, 1996.

Nykanen, A., "Hardening of Concrete at Different Temperatures, Especially below the Freezing Point." *Proceedings*, *RILEM Symposium on Winter Concreting*, Danish Institute for Building Research, Copenhagen, Denmark, 1956.

Pane, I. and W. Hansen, "Concrete Hydration and Mechanical Properties under Nonisothermal Conditions." *ACI Materials Journal*, Vol. 99, No. 6, pp. 534-542, 2002.

Parrott, L.J., "Moisture Profiles in Drying Concrete." *Advances in Cement Research*, Vol. 1, No. 3, pp. 164-170, 1988.

Parrot, L.J., "Factors Influencing Relative Humidity in Concrete." *Magazine of Concrete Research*, Vol. 43, No. 154, March 1991.

Penman, H.L., "Natural Evapotranspiration from Open Water." *Bare Soil, and Grass*, Proceedings of the Royal Society of London, Series A, Vol. 193, pp. 120-146, 1948.

Pihlajavaara, S.E., *Introductory Bibliography for Research on Drying of Concrete*. The State Institute for Technical Research, Helsinki, Finland, 1964.

Plowman, J.M., "Maturity and the Strength of Concrete." *Magazine of Concrete Research*, Vol. 8, No. 22, pp. 13, 1956.

Powers, T.C., "A Discussion of Cement Hydration in Relation to the Curing of Concrete." *Proceedings of the Highway Research Board*, 27, Washington, D.C., pp. 178-188, 1947.

Powers, T.C., "Causes and Control of Volume Change." *Journal of the PCA Research and Development Laboratories*, Vol. 1, No. 1, pp. 29-39, 1959.

Powers, T.C., *Chemistry of Cement. Proceedings of the Fourth International Symposium*. Washington 1960 (National bureau of standards [now National Institute of Standards and Techonology] Monograph 43), Vol. 2, pp. 577, 1962.

Powers, T.C., "The Thermodynamics of Volume Change and Creep." *Materials and Structures*, Vol. 1, No. 6, pp. 487-507, 1968.

RILEM Committee on Fracture Mechanics - Test Methods. "Size-Effect Method for Determining Fracture Energy and Process Zone Size of Concrete." Materials and Structures, Vol. 23, No. 138, pp. 461-465, Nov., 1990.

Ruiz, J.M., A.K. Schindler, R.O. Rasmussen, P.K. Nelson, and G.K. Chang, "Concrete Temperature Modeling and Strength Prediction Using Maturity Concepts in the FHWA HIPERPAV Software." *Proceedings, 7th International Conference on Concrete Pavements*, Vol. 1, Orlando, Florida, pp. 97-111, 2001.

Saul, A.G.A., "Principles Underlying the Steam Curing of Concrete at Atmospheric Pressure." *Magazine of Concrete Research*, Vol. 2, No. 6, pp. 127, 1951.

Says, W.M. and M.E. Crawford, *Convective Heat and Mass Transfer*. McGraw-Hill, New York, New York, 1980.

Siegel, R. and J.R. Howell, *Thermal Radiation Heat Transfer*. 2nd Edition, McGraw-Hill, New York, New York, 1981.

Somasundaram, S., N.K. Anand, Y.B. Suh, and W. Aung, "Analysis of Moisture Migration in Two-Dimensional Unsaturated Porous Media with Impermeable Boundaries." *International Journal of Heat and Mass Transfer*, Vol. 32, No. 9, pp. 1733-1739, 1989.

Suh, Y.B., N.K. Anand, W. Aung, and S. Somasundaram, "Steady-State Moisture Profiles in an Unsaturated Porous Medium with Impermeable Boundaries." *International Journal Heat and Mass Transfer*, Vol. 11 No. 12, pp. 2587-2589, 1988.

Taljaston, B., *Temperature Development and Maturity Growth for Ordinary Swedish Portland Cement Type II*. Diploma Work 1987:035, Technical University of Lulea, Stockholm, Sweden, 1987.

Tang, Tianxi, Dan G. Zollinger, and Sanjaya P. Senadheera, "Analysis of Concave Curling in Concrete Slabs," Vol. 119 No. 4, ASCE *Journal of Transportation Engineering*, July/Aug 1993, pp. 618-633.

Taylor, H.F.W., *Cement Chemistry*. Academic Press Limited, London, United Kingdom, 1990.

Tetens, O., Uber Einige Meteorologische Begriffe Z. *Geophysics*, Vol. 6, pp. 297-309, 1930.

Thepchatri, T., C.P. Johnson, and H. Matlock, "Prediction of Temperature and Stresses in Highway Bridges by a Numerical Procedure Using Daily Weather Reports." *Report No. 23-1*, Center for Transportation Research, The University of Texas at Austin, 1977.

Thornthwaite, C.W., "An Approach Toward a Rational Classification of Climate." *Geographical Review*, Vol. 38, pp. 55-94, 1948.

Trinhztfy, H.W., J. Blaauwendraad, and J. Jongendijk, Temperature Development in Concrete Structures Taking Accounting of State Dependent Properties. *Proceedings, RILEM International Conference on Concrete at Early Ages*, Vol. 1, Paris, pp. 211-218, 1982.

Uno, P.J., "Plastic Shrinkage Cracking and Evaporation Formulas." *ACI Materials Journal,* July-August 1998.

Veihmeyer, F.J., *Evapotranspiration*. Handbook of Applied Hydrology, Ven Te Chow, editor, McGraw-Hill, New York, 1964.

Vepakomma, S., J.H. Jeong, and D.G. Zollinger,. "Characterization of Cracking Restraint at Saw-Cut Joints Using the German Cracking Frame." *Transportation Research Record 1813*, National Research Council, pp. 28-35. 2002.

Walker, S. and D.L. Bloem, *Studies of Flexural Strength of Concrete-Part 2: Effects of Curing and Moisture Distribution on Measured Strength of Concrete*. Proceedings, Highway Research Board, Vol. 36, Washington, D.C., pp. 334-346, 1957.

Wang, L. and D.G. Zollinger, "A Mechanistic Design Framework for Spalling Distress." In *Transportation Research Record 1730,* Journal of the Transportation Research Board, TRB, National Research Council, Washington D.C., pp. 18-24, 2000.

Williamson, P.J., "The Estimation of Heat Output for Road Heating Installations." *LR Rep. 77*, Road Research Laboratory, Ministry of Transport, Berkshire, England, 1967.

Wilson, G.W., *Soil Evaporative Fluxes for Geotechnical Engineering Problems*. Ph.D. Thesis, University of Saskatchewan, Saskatoon, Saskatchewan, Canada, 1990.

Wilson, G.W., D.G. Fredlund, and S.L.Barbour, "Coupled Soil-Atmosphere Modeling for Soil Evaporation." *Canadian Geotechnical Journal*, Vol. 31, pp. 151-161, 1994.

Wittmann, F H., "Surface Tension Shrinkage and Strength of Hardened Cement Paste." *Materials and Structures*, Vol. 1, No. 6, pp. 547-552, 1968.

Wittmann, F.H., "Creep and Shrinkage Mechanisms." *Creep and Shrinkage in Concrete Structures*, Bažant, Z.P. and F.H. Wittmann, eds., John Wiley and Sons, New York, pp. 129-161, 1982.

Xin, D., D.G. Zollinger, and G.D. Allen, "An Approach to Determine Diffusivity in Hardening Concrete Based on Measured Humidity Profiles." *Advanced Cement Based Materials*, Vol. 2, pp. 138-144, 1995.

Xin, Dapeng, Dan G. Zollinger, and Allen G.D., "A Method to Determine Moisture Diffusivity in Concrete from Measured Moisture Profiles," *Journal of Advanced Cement Based Materials*, Vol. 2, pp. 1-7, Elsevier Science Inc., 1995.

Yang, S.A., "Temperature Prediction Model in New Concrete Pavement and New Test Method for Concrete Fracture Parameters." *PhD. Dissertation*, Texas A&M University, College Station, 1996.

Zollinger, Dan G., Sanjaya P. Senadheera, and Tianxi Tang, "Spalling of Continuously Reinforced Concrete Pavements," Vol. 120 No.3, ASCE *Journal of Transportation Engineering*, May/June 1994, pp.394-411.

APPENDIX A

RESULTS OF FIELD TEST AT VAN HORN (2003)

INTRODUCTION

A field test program was conducted for the newly placed concrete pavement of Interstate Highway 10 between March 26th and 28th under Project 5-1700-1 (implementation). The test section was located between Van Horn and Sierra Blanca in Hudspeth County approximately 80 miles east of El Paso. The main objective of the test was collecting moisture-related data to validate and calibrate the moisture model of TMAC^2, evaporation model, and moisture-based maturity model developed under Project 0-1700. Final set time and effect of moisture loss on drying shrinkage strain were studied using additional test instrumentation. The following briefly summarizes the test items.

- Weather conditions (ambient temperature, ambient relative humidity, wind speed, and solar radiation)
- Temperature and relative humidity of pavement (1.9, 7.6, and 17.8 cm [0.75, 3, and 7 inch] from surface)
- Curing monitoring (relative humidity of ambient, surface, and concrete at 1.9 cm [0.75 inch] below pavement surface)
- Initial and final set times (penetration resistance test)
- Relationship between drying shrinkage and concrete relative humidity (drying shrinkage test)

CONSTRUCTION AND DATA CATEGORY

A field test program was conducted for the newly placed concrete pavement of Interstate Highway 10 between March 26th and 28th. The test section was located between Van Horn and Sierra Blanca in Hudspeth County approximately 80 miles east of El Paso. The continuously reinforced concrete pavement with 30.5 cm (12 inch) thickness was placed at 10:00 am of March 26th on the existing 7.6 cm (3 inch) of asphalt pavement. During the period of data collection, a weather station was placed near the test section to measure hourly data of ambient temperature, ambient relative humidity, wind speed, and solar radiation. A curing monitoring system measured temperature, ambient relative humidity, and surface and internal concrete relative humidity (1 inch below the concrete surface). Temperature and relative humidity data of the pavement were also collected at 7.6

and 17.8 cm (3 and 7 inch) below the top surface using chilled mirror sensors. Initial and final setting times were found using a penetrometer and maturity data of a mortar specimen. Total strains of shrinkage bar specimens were measured using demac gauges to be correlated to their relative humidity by placing a chilled mirror sensor in another shrinkage bar specimen.

WEATHER CONDITIONS

A weather station was installed near the location where the chilled mirror sensors and curing monitoring system were instrumented before the placement of the concrete. The weather station recorded ambient temperature, ambient relative humidity, wind speed, and solar radiation. It collected data at hourly intervals on a continuous basis. Radiation and convection play a dominant role in transferring heat between the slab surface and its immediate surroundings, while conduction plays a separate role in transferring heat within the concrete slab. Maintaining higher levels of surface humidity is important for better curing quality, which can be achieved by high ambient relative humidity and low wind speed. Moisture variation or diffusion within the concrete slab is due to a difference in humidity between the slab surface and the concrete immediately below the surface.

Over the 3 days after placement of concrete, ambient temperatures ranged from a low of almost 0 ^{o}C in the morning hours to a high in the high 20s ^{o}C in the afternoon as shown in Figure A-1 (a). It is interesting to note the unpredictable change in the daily pattern of ambient temperature. Significantly higher ambient temperature was observed the morning of March 27th. Ambient relative humidity ranged from a low in the low 10 percent in the afternoon to a high around 100 percent in the morning over the same period as shown in Figure A-1 (a). The daily pattern of ambient relative humidity also shows unpredictable changes. Maximum relative humidity of 71, 26, and 100 percent were recorded the mornings of March 26th, 27th, and 28th, respectively.

As shown in Figure A-1 (b), 1.01 kW/m^2 of maximum solar radiation and 25.7 m/s (57.5 mph) of wind speed were recorded over the period. Maximum solar radiation was recorded between 12:00 and 1:00 pm and was zero at night. Any daily pattern could not be found from the wind speed data, while maximum wind speed was recorded at 3:00 am of March 27th.

TEMPERATURE AND MOISTURE OF PAVEMENT

Chilled mirror dew point and dry bulb temperature sensors were positioned in the pavement to measure moisture-related data at key locations. As shown in Figure A-2, two longitudinal bars (5th and 6th from the side of the pavement) were cut before placement of concrete to place a 1.3 cm (0.5 inch) thick PVC cylindrical wall. The PVC cylinder had both a diameter and height of 30.5 cm (12 inch). The dew point sensors were protected from direct contact with the fresh concrete by use of brass casings, which are fixed into the PVC cylinder that was inserted within the pavement to ensure proper positioning of the sensors. The dew point sensors were located at 7.6 and 12.7 cm (3 and 5 inch) below the pavement surface. Several openings in the brass casings allowed the environment inside the casing to equilibrate with the environment inside the concrete. The sensors were sealed inside the casing to prevent contamination from ambient temperature and humidity conditions. Concrete temperature and relative humidity at 1.9 cm (0.75 inch) below the pavement surface was measured by another dew point sensor of the curing monitoring system which will be described in the next section.

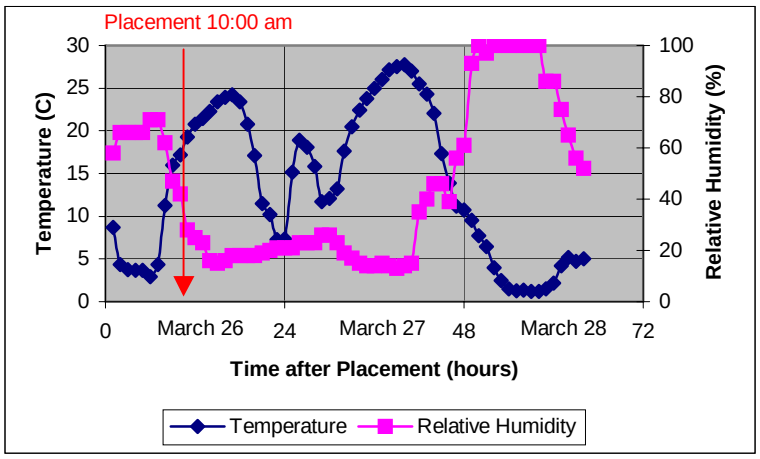

(a)

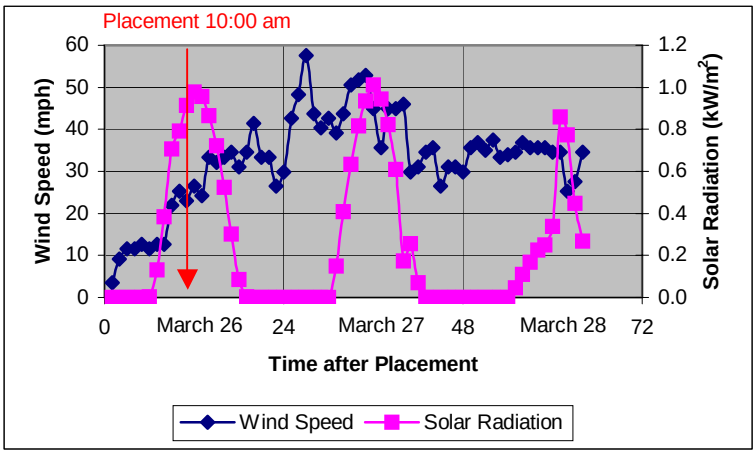

(b)

Figure A-1 Weather Conditions at Van Horn: (a) Ambient Temperature and Relative Humidity; (b) Wind Speed and Solar Radiation.

Heat development during hydration was reduced (and to some extend retarded) due to use of slag in the paving mixture. The accumulation of heat was also retarted due to the low ambient temperature and high wind speed conditions. The concrete temperature steadily decreased until the following morning at each point of measurement due to low heat emission as shown in Figure A-3 (a). Because of the low heat development of concrete, daily maximum peaks of concrete temperature at each point of measurement were almost the same or a little bit higher than the ambient temperature at those times. Concrete temperature measured at 1.9 cm (0.75 inch) below the surface was more affected by the ambient condition and, consequently, had closer values to the ambient temperature than the temperature measured at 7.6 and 17.8 cm (3 and 7 inch). Concrete temperature measured at 7.6 and 17.8 cm (3 and 7 inch) had almost the same values during the period of data collection.

Figure A-2 Rebar Cutting for Instrumentation of Chilled Mirror Sensors.

Concrete relative humidity steadily increased until the following morning and then began to decrease because the rate of evaporation and moisture diffusion of the concrete significantly reduced at that time. Relatively low concrete humidity was maintained at every depth of measurement during the period due to low ambient relative humidity as shown in Figure A-3 (b). However, concrete relative humidity increased again from the afternoon of that day because the ambient relative humidity substantially increased to 100 percent. Concrete relative humidity measured at 1.9 cm (0.75 inch) below the surface was more affected by ambient relative humidity as observed in the concrete temperature trends.

CURING CONDITION AND EVAPORATION

As shown in Figure A-4 (a), a curing monitoring system manufactured by ATEK was installed immediately after placing the concrete to collect data from the pavement when it cured. The ATEK system (Figure A-4 (b)) includes a plastic casing, as noted in Figure A-4 (c), connected to an aluminum stand that supports the weight of the curing monitoring system that is inserted approximately 5.1 cm (2 inch) into the concrete. There are four holes in the casing 1.9 cm (0.75 inch) below the concrete surface to allow the vapor pressure of the concrete to equilibrate inside the casing. The relative humidity inside the concrete was determined from a chilled mirror type sensor, which measures the dry bulb and the dew point temperature from inside the plastic casing. The surface sensor measures the relative humidity from inside a PVC cylinder with an inside diameter and height of 6.4 cm (2.5 inch) and 5.1 cm (2 inch), respectively, as shown in Figure A-4 (b). The cylinder was placed on the pavement surface in an area cleared of the curing membrane such that the sensor will register the relative humidity just below the curing membrane. The third sensor measures the relative humidity just above the curing membrane.

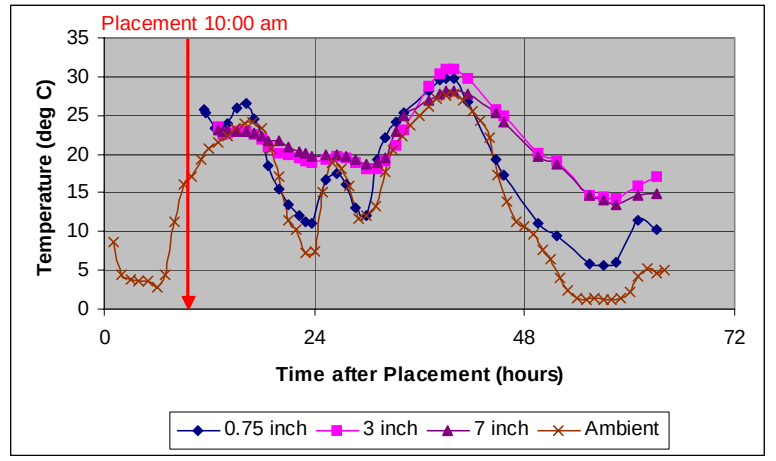

(a)

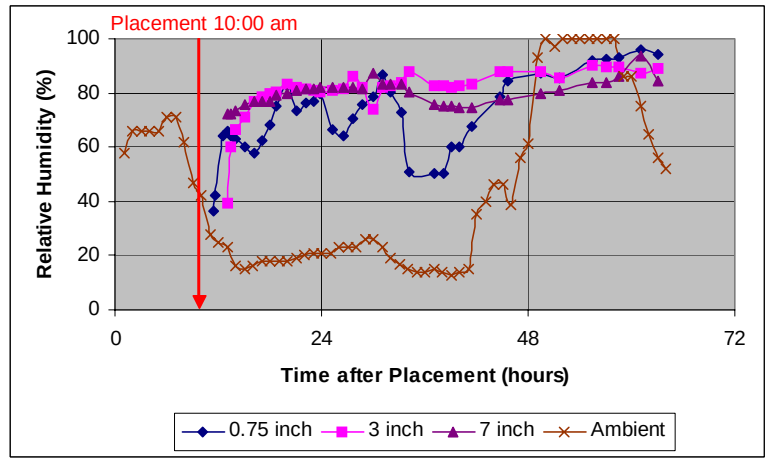

(b)

Figure A-3 Temperature and Relative Humidity at Different Depths of Pavement: (a) Temperature; (b) Relative Humidity.

The ambient relative humidity could not be measured because the sensor was out of order after a few hours of data collection. The ambient relative humidity data collected from the weather station was used in place of the ambient relative humidity of the curing monitoring system. The relative humidity of both surface and inside concrete increased due to bleeding until the next day of construction and was higher than the ambient relative humidity during the period as shown in Figure A-5. However, they decreased from the following morning due to the reduced rate of evaporation and moisture diffusion as described previously.

To quantify the curing effectiveness, we used the effective curing thickness concept originally introduced by Bažant and Najjar (1972).

(a)

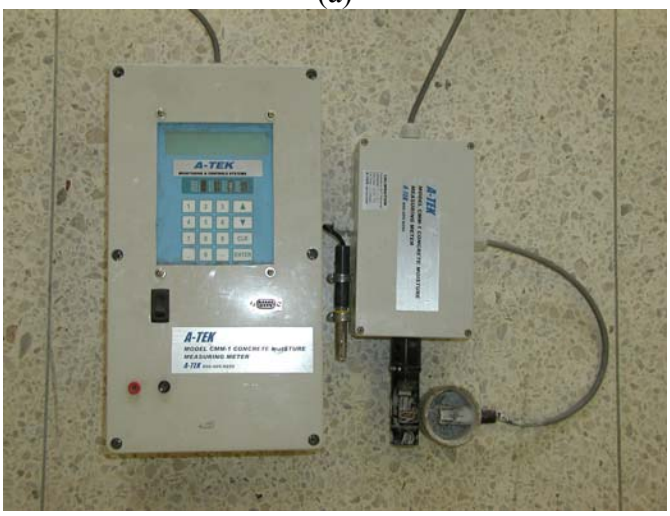

(b)

(c)

Figure A-4 Curing Monitoring System: (a) Instrumentation; (b) Sensors and Reader; (c) Casing.

Effective curing thickness can be described as the equivalent layer of concrete that would provide the same degree of curing as the curing medium. Properly cured concrete has an effective curing thickness in the range of 7.6 to 12.7 cm (3 to 5 inch). In other words, the thicker the effective curing thickness is, the smaller are the humidity variations near the surface (Jeong and Zollinger, 2003).

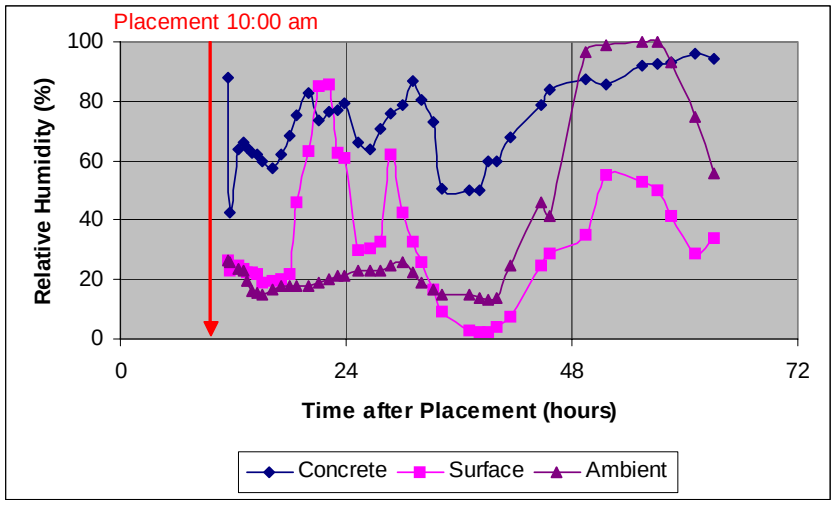

Figure A-5 Relative Humidity of Ambient, and Surface and Inside Concrete.

The trend of effective curing thickness shown in Figure A-6 was similar to those of the surface relative humidity because the effective curing thickness is governed mainly by the surface humidity. The effective curing thickness increased throughout the duration of the bleeding when surface humidity also increased. Both effective curing thickness and the surface humidity decreased simultaneously after bleeding. The calculated maximum value of the effective curing thickness of 3.1 cm (1.2 inch) indicates a poor curing condition was made due to severe weather conditions despite the curing compound application.

Rate of evaporation was calculated using the new evaporation model described in Chapter 4.

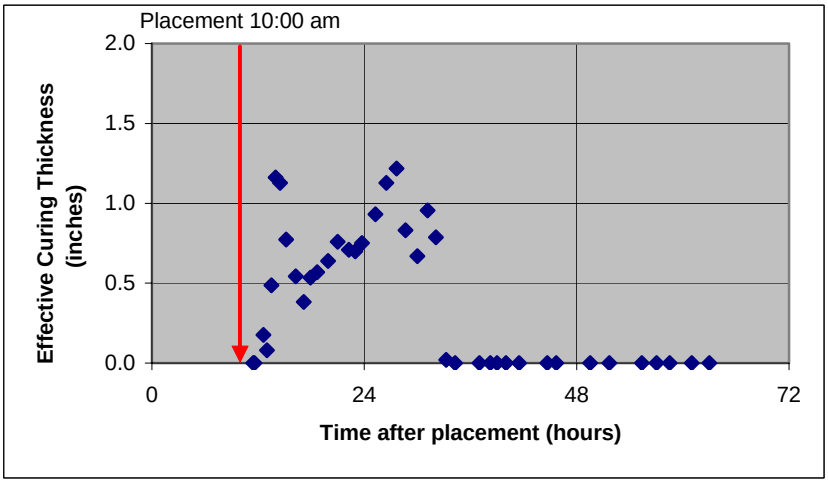

Figure A-6 Effective Curing Thickness of Pavement with Curing Time.

The rates of evaporation computed from the model and test data were clearly affected by weather conditions. High wind speed and solar radiation, and low ambient relative humidity significantly increased the rate of evaporation as shown in Figure A-7. The rate of evaporation increased during bleeding and then decreased to zero.

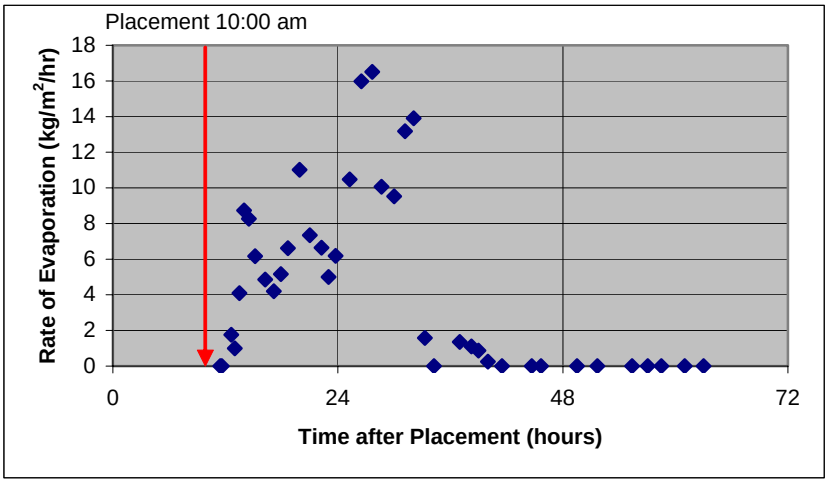

Figure A-7 Calculated Rate of Evaporation with Curing Time.

INITIAL AND FINAL SETTINGS OF PAVEMENT

The maturities of the initial and final setting of the concrete pavement were found using test procedure ASTM C 403 to represent the initiation point of pavement behavior. Previous research indicated that the concrete slab began to behave at the points when the concrete reached final set. Three mortar samples with 15.2 cm (6 inch) diameter and 15.2 cm (6 inch) height were obtained by sieving fresh concrete. A thermocouple was embedded in a sample to measure concrete maturity. At regular time intervals, the resistances of the mortar specimens to penetration of different diameter of standard needles were measured (Figure A-8) for another sample. From a plot of penetration resistance versus elapsed time, the times of initial and final setting were determined.

The maturities of 160 and 240 ^{o}C-hours were correlated with 3.5 MPa (initial setting resistance of 500 psi) and 27.6 MPa (final setting resistance of 4000 psi) of penetration resistances, respectively, as shown in Figure A-9. The initial and final setting times of 2:30 pm and 5:00 pm were determined by correlating the test results to the maturity of the pavement (which were approximately 4.5 and 7 hours after placement of the pavement).

RELATIONSHIP BETWEEN DRYING SHRINKAGE AND MOISTURE LOSS

Figure A-8 Penetration Resistance Test by ASTM C 403.

Relative humidity of concrete has been recognized to have effect on the development of drying shrinkage. However, the relationship between them has not been studied sufficiently because of the troubles in accuracy of moisture measuring devices and instrumentation techniques. Three shrinkage bar specimens were made following the procedure of ASTM C 157. Demac points were placed on the surfaces of two specimens and a chilled mirror sensor was inserted into another specimen by using a brass casing as shown in Figure A-10. Molds of the specimens were not demolded during the measurement period to prevent the drying of the specimens from their sides.

Because the chilled mirror sensor was installed at shallow depth (3.8 cm [1.5 inch]) and the sides of the specimen could be affected by ambient, relative humidity was almost the same as that measured at 1.9 cm (0.75 inch) from the pavement surface as

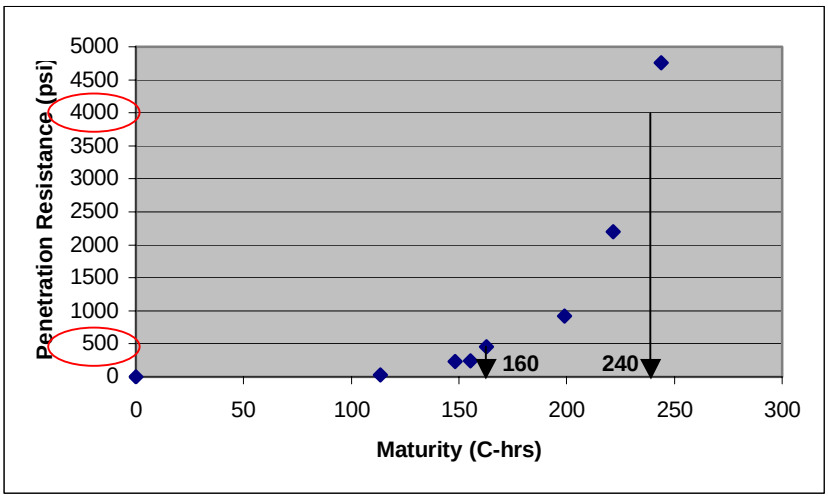

Figure A-9 Maturities at Initial and Final Settings.

shown in Figure A-11(a). Drying shrinkage strains were calculated by subtracting calculated thermal strains from measured total strains as shown in Figure A-11(b). Thermal strains were calculated by multiplying temperature changes and 12 micro-strains/^{o}C of coefficient of thermal expansion of the specimen, which was approximately estimated by experimental experiences. The measurement continued in a laboratory of the Texas Transportation Institute even after coming back from Van Horn. Linear relationship between drying shrinkage and relative humidity of the specimen was observed as shown in Figure A-11(c). It is the same trend observed in another laboratory test previously conducted (Figure A-12). Constant curing temperature and relative humidity of 50 ^{o}C and 10 percent were maintained in the test.

Figure A-10 Drying Shrinkage Test by ASTM C 157.

MOISTURE-BASED MATURITY

Concrete hardens with the increase of hydration products made by the reaction between water and cement. The concrete should be nearly saturated by preventing evaporation from the surface to continue the hydration. Powers (1947) suggested that hydration completely stopped when the relative humidity of the concrete decreased to 80 percent. Because the strength of concrete is significantly influenced by moisture level within the concrete and the moisture level is different with pavement depth (Figure A-13), existing maturity concepts were modified by including a moisture parameter in the maturity model (Chapter 3):

Moisture-based maturity was calculated on the basis of the temperature and moisture data. Relatively higher moisture-based maturity was calculated when the relative humidity of the pavement was high on the third day after placement, while lower moisture-based maturity was calculated during the period of low concrete relative humidity measurement (Figure A-14).

CONCLUSIONS

Field measurements were made for the continuously reinforced concrete pavement to see environmental effects on the pavement. During the period of measurement, severe weather conditions such as high wind speed, rapid and large variations in ambient temperature and relative humidity influenced the pavement, especially at shallower depths. Because

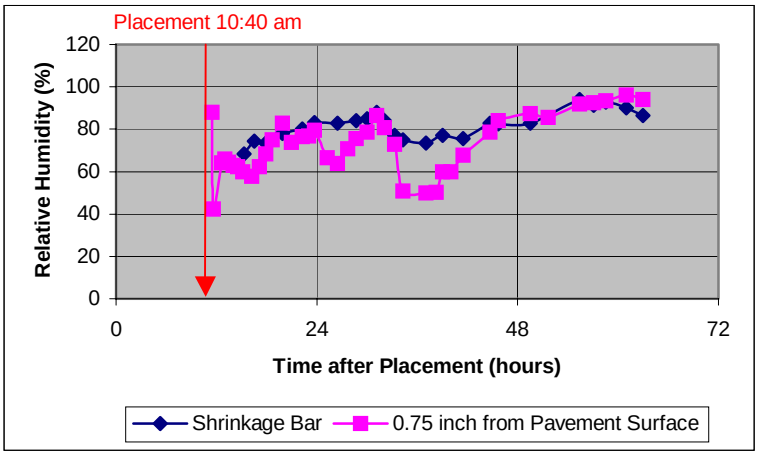

(a)

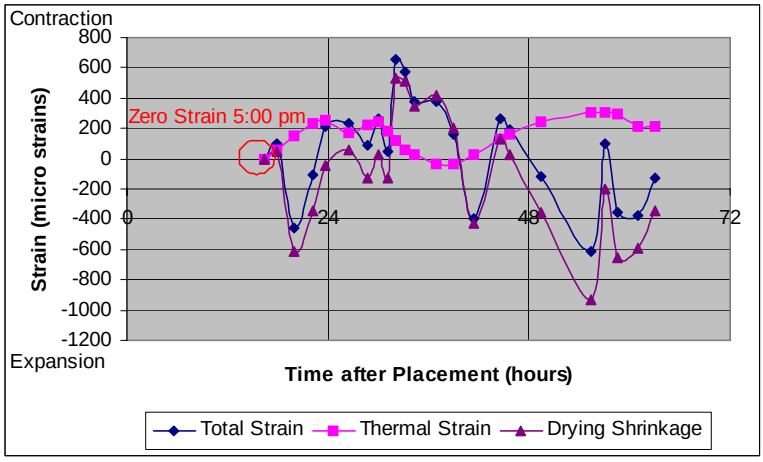

(b)

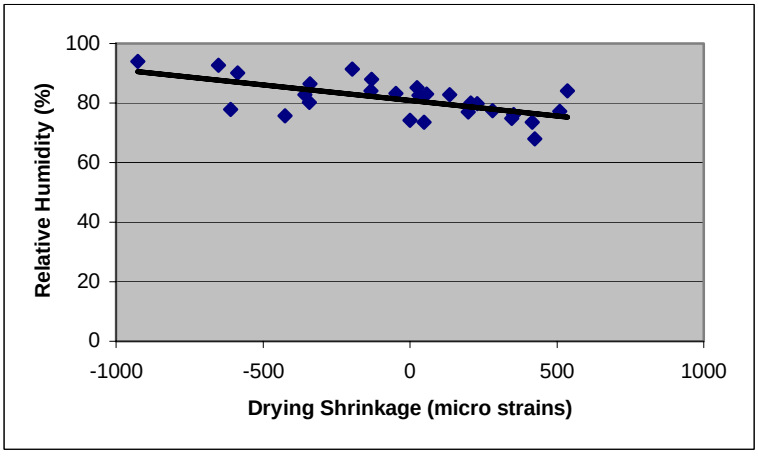

(c)

Figure A-11 Relationship between Drying Shrinkage Strains and Relative Humidity: (a) Relative Humidity with Curing Time; (b) Drying Shrinkage Strains with Curing Time; (c) Drying Shrinkage with Relative Humidity.

heat development by hydration was restrained due to the weather condition and material property of concrete, pavement temperature was not increased so much. Relatively low initial effective curing thickness and high rate of evaporation were calculated due to poor curing conditions caused by the severe weather. The evaporation model may need to be calibrated for the high wind speed because lower levels of wind speeds were used as a parameter to develop the model. Initial and final set times of the pavement were found at 4 hours 30 minutes and 7 hours after placement using the penetration resistance test. The linear relationship between drying shrinkage and relative humidity of concrete was observed by the drying shrinkage test. Although a reasonable trend of moisture-based maturity was calculated using collected temperature and moisture data, a cumulative moisture parameter that utilizes moisture history of concrete needs to be developed to consider the moisture variation due to environmental conditions in field.

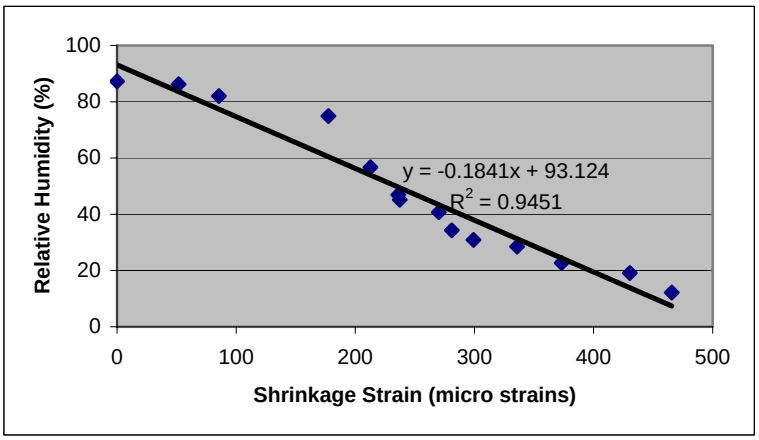

Figure A-12 Another Test's Results of Drying Shrinkage Strains with Relative Humidity.

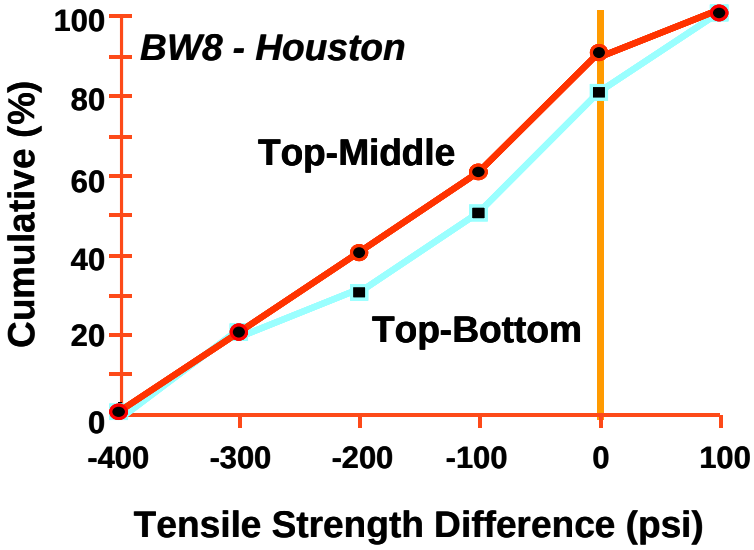

Figure A-13 Strength Differences between Different Depths of Pavement (Houston Test Section).

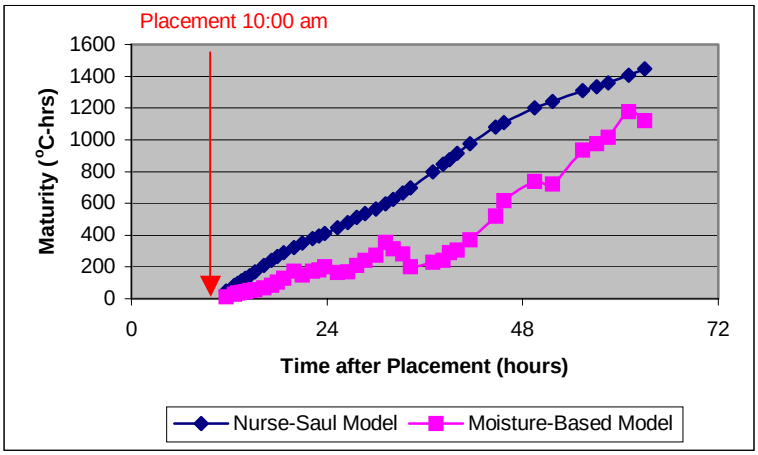

Figure A-14 Moisture-Based Maturity with Curing Time.

APPENDIX B
RESULTS OF FIELD TEST AT BAYTOWN

INTRODUCTION

A field test program was conducted for the newly placed concrete pavement at 330 Spur near Baytown between July 26th, 2003 and July 28th, 2003 under Project 5-1700-1 (implementation). The test section was located on 330 Spur between I-10 (near Baytown) and I-146 in the outskirts of Houston (approx. 25 miles east of Houston). The main objective of the test was collecting moisture-related data to validate and calibrate the moisture model of TMAC^2, the evaporation model, the moisture-based maturity model, and the model for curing effective thickness developed under Project 0-1700.

CONSTRUCTION AND DATA CATEGORY

The continuously reinforced concrete pavement with 30.5 cm (12 inch) thickness was placed at 12:30 pm on July 26th . The following briefly summarizes the test items:

- Weather condition (ambient temperature, ambient relative humidity, wind speed, solar radiation)
- Temperature and relative humidity of pavement at 1.9, 7.6, and 17.8 cm (0.75, 3, and 7 inch) below surface
- Curing monitoring:
  - Relative humidity of ambient, surface, and concrete 1.9 cm (0.75 inch) below surface
  - Prediction of curing effective thickness
  - Prediction of rate of evaporation
  - Moisture-based maturity
- Initial and final setting time (penetration resistance test)
- Relationship between concrete relative humidity and drying shrinkage (drying shrinkage test using ASTM 157 specimen)

Instrumentation and installation of field test equipments was the same as the Van Horn test section.

WEATHER CONDITIONS

Ambient temperature, ambient relative humidity, wind speed, and solar radiation data were recorded at hourly intervals on a continuous basis through a weather station. Over the 3 days after placement of concrete, ambient temperatures ranged from a low of almost 77 °F in the morning hours to a high of 92 °F in the afternoon as shown in Figure B-1 (a). A daily temperature fluctuation (morning to afternoon) of about 15 °F (from 77 to 92 °F) was noticed on the 27th and 28th of July whereas a slightly lower temperature fluctuation of 8 °F (from 79 to 87 °F) was noticed on the 26th of July. Ambient relative humidity ranged from a low of 49 percent in the afternoon to a high around 100 percent in the morning over the same period as shown in Figure B-1 (a). The lowest relative humidity of 66, 52, and 49 percent in the afternoons of July 26th, 27th, and 28th, respectively, and the highest relative humidity of 100 percent in all 3 days were recorded during the morning.

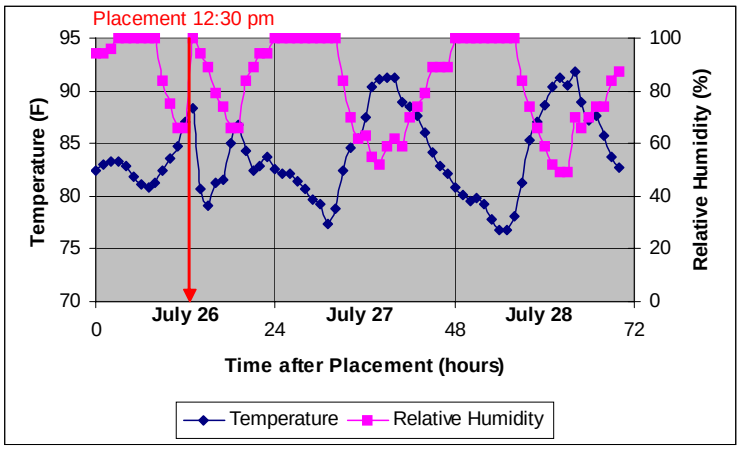

(a)

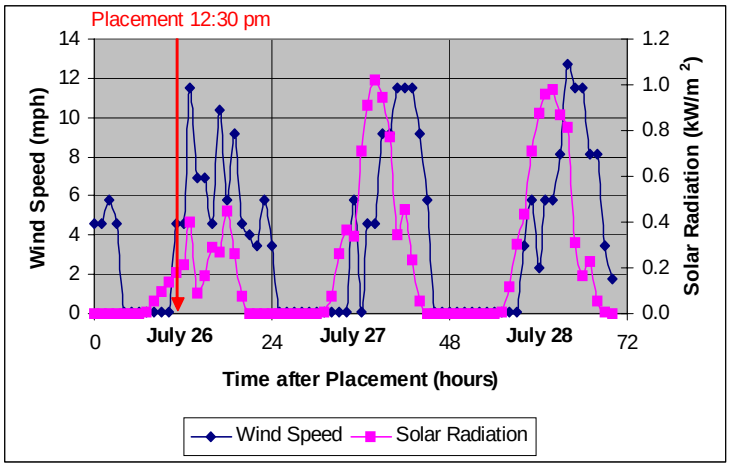

(b)

Figure B-1 Weather Conditions at Baytown: (a) Ambient Temperature and Relative Humidity; (b) Wind Speed and Solar Radiation.

As shown in Figure B-1 (b), 1.019 kW/m^2 of maximum solar radiation and 12.7 mph (5.7 m) of wind speed were recorded over the period. Maximum solar radiation was recorded between 12:00 and 1:00 pm daily. Wind speed shows maximum during late afternoon (slightly later than maximum solar radiation) on 27th and 28th whereas prevalence of relatively higher wind speed throughout the afternoon (12 to 8 pm) was recorded on the 26th.

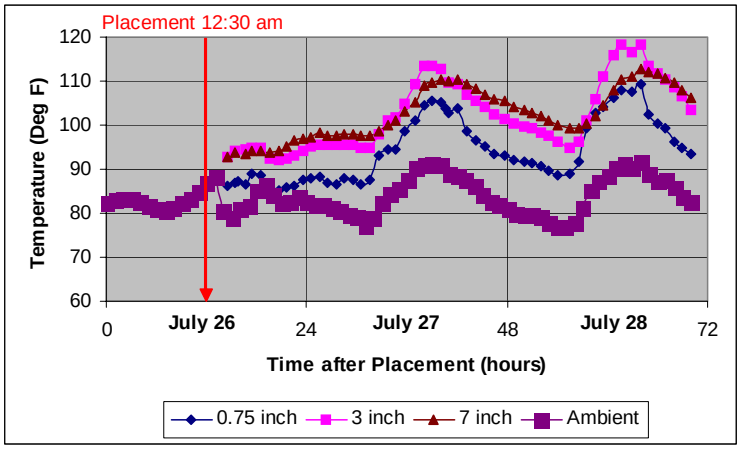

(a)

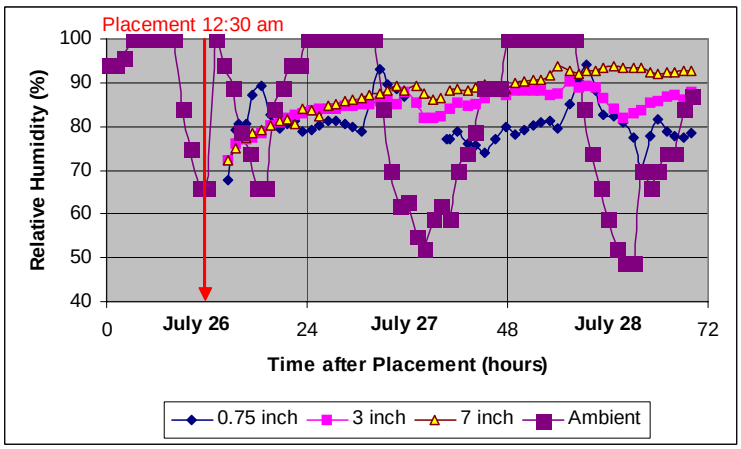

(b)

Figure B-2 Temperature and Relative Humidity at Different Depths of Pavement: (a) Temperature; (b) Relative Humidity.

TEMPERATURE AND MOISTURE OF PAVEMENT

Temperature and relative humidity data at 1.9, 7.6, and 17.8 cm (0.75, 3, and 7 inch) depth were recorded by using chilled mirror dew point and dry bulb temperature sensors. The instrumentation of these sensors was similar to the instrumentation described in Appendix A for Van Horn. The following summarizes the observation on the temperature and moisture situation at different depths.

- Concrete temperature followed a slight increasing trend until the following morning at every depth of measurement in spite of a decreasing trend of ambient temperature as shown in Figure B-2 (a). This increase is caused by heat evolved due to cement hydration in concrete in spite of 30 percent fly ash

replacement. It is interesting to recall that in Van Horn, the temperatures at three depths showed a decreasing trend until the next morning, and this was due to low heat evolution due to a higher amount of slag replacement (50 percent).

- Concrete temperatures at three depths were always higher than ambient temperature although the trend of concrete temperatures at three depths was similar to the trend of ambient temperature. Concrete temperatures at 1.9 cm (0.75 inch) were always lower than these at 7.6 and 17.8 cm (3 and 7 inches). The temperature measured at 7.6 and 17.8 cm (3 and 7 inch) had almost the same values during the period of data collection.
- Daily temperature fluctuation at 1.9 cm (0.75 inch) was higher than that at 7.6 and 17.8 cm (3 and 7 inch). The daily maximum peak temperature at 1.9 cm (0.75 inch) was lower that that at 7.6 and 17.8 cm (3 and 7 inch) in the next afternoon (July 27); however, it reached the temperature similar to 7.6 and 17.8 cm (3 and 7 inch) depth in the second afternoon (July 28). Therefore, concrete temperature at 1.9 cm (0.75 inch) was more affected by ambient temperature condition than that at 7.6 and 17.8 cm (3 and 7 inch) depth.

Following are the observations on concrete relative humidity at different depths in conjunction with ambient relative humidity:

- Concrete relative humidity steadily increased until the following morning at 7.6 and 17.8 cm (3 and 7 inch) depth while at 1.9 cm (0.75 inch) it showed an overall increasing trend with more fluctuation (Figure B-2 (b)).
- The relative humidity at 1.9 cm (0.75 inch) showed more daily variation than that at 7.6 and 17.8 cm (3 and 7 inch) depth. Variation of ambient relative humidity had more influence on relative humidity at 1.9 (0.75 inch) while relative humidity at 17.8 cm (7 inch) depth was practically unaffected by ambient relative humidity. Relative humidity at 7.6 cm (3 inch) depth was slightly affected by ambient relative humidity after 33 to 36 hours.
- Relative humidity at 1.9 cm (0.75 inch) showed an increasing trend when ambient relative humidity was in a decreasing trend while it was at a more or less constant level (around 80 percent) when ambient relative humidity was in

an increasing trend until 32 to 34 hours. This moisture behavior at 1.9 cm (0.75 inch) is due to a combination of high evaporation and bleeding. After around 33 hours, the trend of relative humidity at 1.9 cm (0.75 inch) was controlled by the trend of ambient relative humidity. Therefore, the concrete relative humidity measured at 1.9 cm (0.75 inch) below the surface was more affected by ambient relative humidity as observed in the concrete temperature trends.

CURING CONDITION AND EVAPORATION

Installation and instrumentation of the ATEK curing monitoring system was followed the way it is described in Appendix A for the Van Horn test section. Temperature and relative humidity data at 1.9 cm (0.75 inch) depth, surface, and ambient were recorded at hourly intervals on a continuous basis. The following briefly summarizes the observations on concrete moisture at 2.54 cm (1 inch) and surface moisture with respect to ambient relative humidity:

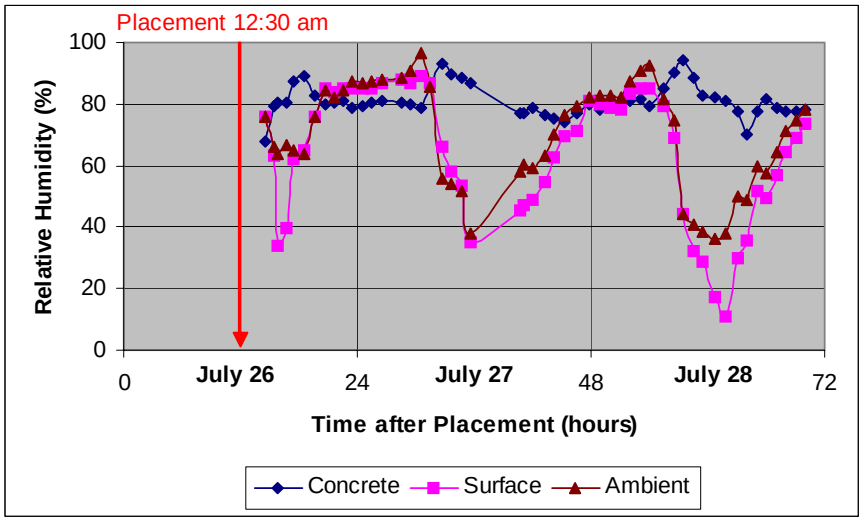

Figure B-3 Relative Humidity of Ambient, Surface, and Inside Concrete at 0.75 Inch Below.

- Both surface and concrete relative humidity were influenced by ambient relative humidity, however, the influence was more intense on the surface rather than concrete at 1.9 cm (0.75 inch) as shown in Figure B-3.
- Relative humidity at 1.9 cm (0.75 inch) showed an increasing trend when ambient relative humidity was in a decreasing trend while it was at a more or less constant level (around 80 percent) when ambient relative humidity was in

an increasing trend until 32 to 34 hours. This moisture behavior at 1.9 cm (0.75 inch) is due to a combination of high evaporation and bleeding.

- The weather was cloudy with low variation of temperature, relative humidity, and solar radiation in the first day. These conditions caused less evaporation during the first day after placement. This is possibly the reason for slightly higher surface and ambient relative humidity than that at concrete during evening to morning.
- Relative humidity of both surface and inside concrete increased due to bleeding until the next day of construction as shown in Figure B-3. However, they decreased thereafter due to a reduced rate of evaporation and moisture diffusion as described previously.
- Overall relative humidity variation at 1.9 cm (0.75 inch) was lower than that at Van Horn.

The effective curing thickness and rate of evaporation were calculated based on the approach described in Appendix A and presented in Figures B-4 and B-5. Low effective curing thickness along with low evaporation was manifested within 24 hours.

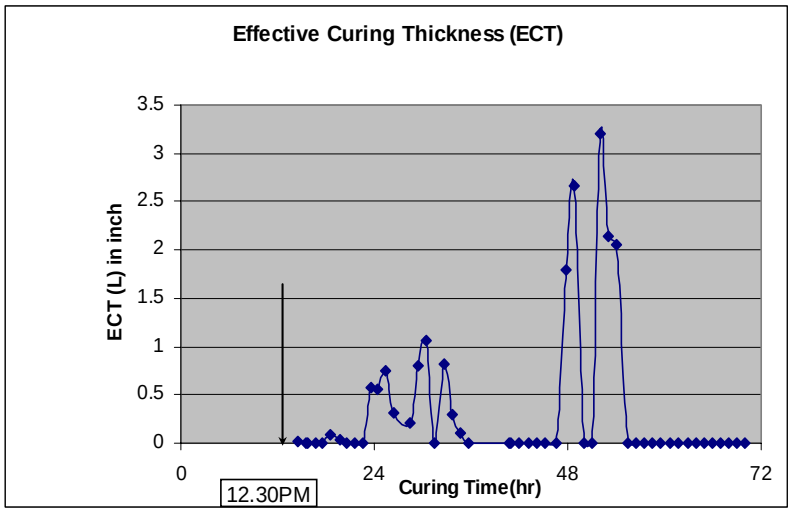

Figure B-4 Effective Curing Thickness of Pavement with Curing Time.

INITIAL AND FINAL SETTINGS OF PAVEMENT

The initial and final setting times were measured using the ASTM C 403 test method. The instrumentation and test procedure was followed the way it is described in Appendix A for the Van Horn test section. Initial and final settings were determined from a plot of penetration resistance versus elapsed time, which were approximately 8 and 9 hours after placement of concrete in the pavement. The maturities of 350 and 405 °C-hours were correlated with 3.5 MPa (initial setting resistance of 500 psi) and 27.6 MPa

(final setting resistance of 4000 psi) of penetration resistances, respectively, as shown in Figure B-6.

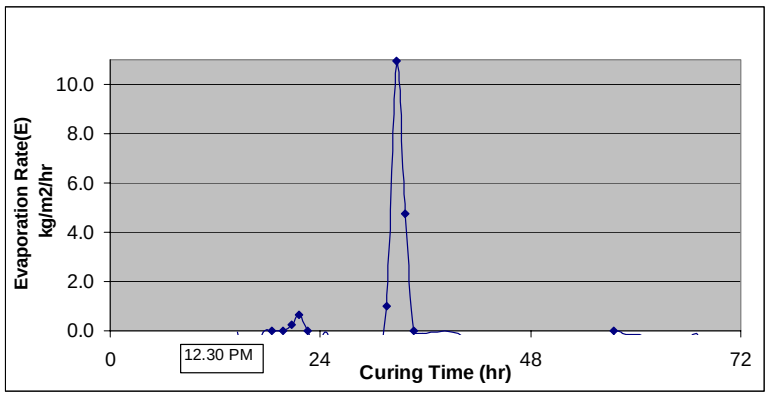

Figure B-5 Calculated Evaporation Rate with Curing Time.

RELATIONSHIP BETWEEN DRYING SHRINKAGE AND MOISTURE LOSS

An attempt had been made to find the relationship between drying shrinkage strain and relative humidity based on the method described in Appendix A for the Van Horn test section. Drying shrinkage strains were calculated by subtracting calculated thermal strains from measured total strains. Thermal strains were calculated by multiplying temperature changes and 9 micro-strains/°C of coefficient of thermal expansion of the specimen, which was approximately estimated by experimental experiences. The linear relationship between drying shrinkage and relative humidity of the specimen was observed as shown in Figure B-7.

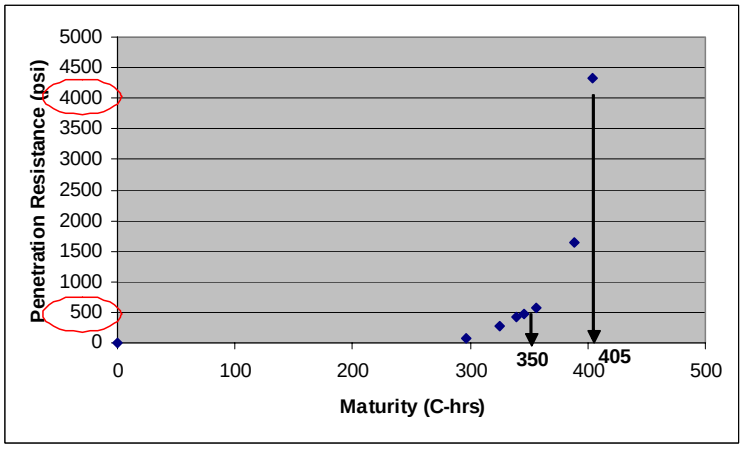

Figure B-6 Maturities at Initial and Final Settings.

MOISTURE-BASED MATURITY

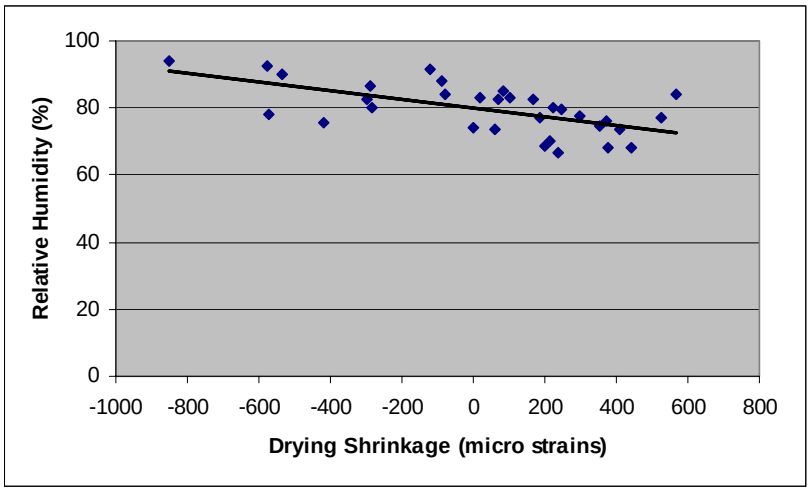

Figure B-7 Drying Shrinkage versus Relative Humidity.

Existing maturity concepts were modified by including a moisture parameter in the maturity model (see details in Appendix A), and moisture-based maturity was calculated using this modified model. Both conventional and moisture-based maturity are compared and presented in Figure B-8. A perusal of Figure B-8 shows that moisture-based maturity is always lower than conventional temperature-based maturity at all ages until 72 hours.

CONCLUSIONS

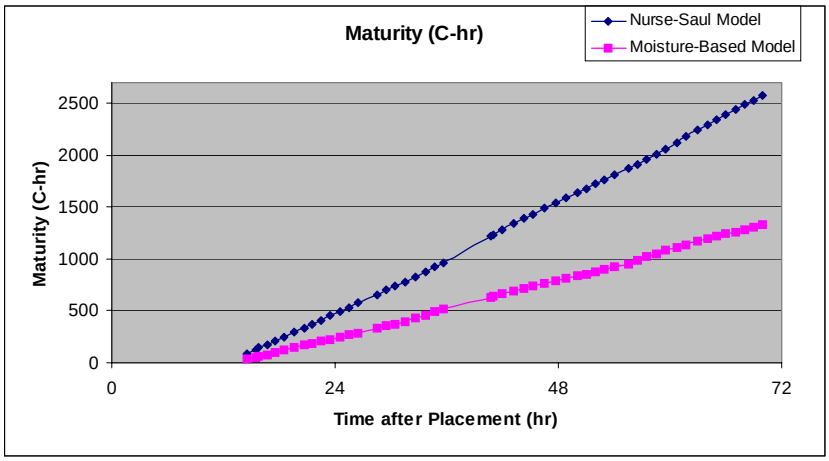

Figure B-8 Moisture-Based Maturity versus Conventional Time-Temperature Maturity as a Function of Curing Time.

Effect of environmental parameters on the performance of continuously reinforced concrete pavement were studied using field measurements at Baytown. The following conclusions can be drawn from the test results:

- The daily variation of temperature and relative humidity was low. The absolute solar radiation was high but wind speed was in normal range.
- Concrete temperature at 1.9 cm (0.75 inch) below surface was more affected by ambient temperature than that at 7.6 and 17.8 cm (3 and 7 inch) below surface. Daily temperature fluctuation at 1.9 cm (0.75 inch) below surface was higher than that 7.6 and 17.8 cm (3 and 7 inch) below surface.

- Concrete temperatures at three depths were always higher than ambient temperature. Concrete temperatures at shallow levels 1.9 cm ([0.75 inch] below surface) were lower than those at deeper levels 7.6 and 17.8 cm ([3 and 7 inch] below surface) during the 72 hour data collection period.
- Relative humidity at 1.9 cm (0.75 inch) showed more daily variation than that at 7.6 and 17.8 cm (3 and 7 inch) below surface. Relative humidity at 17.8 cm (0.7 inch) depth showed a steep increase at the beginning (up to 6-7 hours), and this is due to a combination of high evaporation and bleeding. Concrete relative humidity at 1.9 cm (0.75 inch) was more affected by ambient relative humidity.
- Initial and final set times of the pavement were found 8 and 9 hours after placement of concrete in the pavement using the penetration resistance test.
- Linear relationship between drying shrinkage and relative humidity of concrete was observed using the drying shrinkage test.

APPENDIX C
RESULTS OF FIELD TEST AT US 59, CLEVELAND

INTRODUCTION

A field test program was conducted for the newly placed concrete pavement at US 59 near Cleveland between July 20th, 2004, and July 24th, 2004, under Project 0-1700 (research) and Project 5-1700-3 (implementation). The site for testing is in the Houston district described as Federal Aid Project No. NH2001 (93) in Montgomery County, south of Cleveland, Texas. The project is 3.668 miles long and extends from FM 2090 south to approximately Fosteria Road. The main objective of the test was collecting moisture-related data to validate and calibrate the moisture model of TMAC^2, the evaporation model, the moisture-based maturity model, and the model for curing effective thickness developed under Project 0-1700.

CONSTRUCTION AND DATA CATEGORY

The continuously reinforced concrete pavement with 13 inch thickness was placed at 7:30 am on July 20th on the existing 2.54 cm (1 inch) of asphalt bond breaker. The following parameters were monitored by using different test methods:

- Weather condition (ambient temperature, ambient relative humidity, wind speed, solar radiation)
- Temperature and relative humidity of pavement at 1.9, 7.6, and 17.8 cm (0.75, 3, and 7 inch) below the surface
- Curing monitoring
- Relative humidity of ambient, surface, and concrete 1.9 cm (0.75 inch) below surface
- Prediction of curing effective thickness
- Prediction of rate of evaporation
- Moisture-based maturity
- Initial and final setting time (Penetrometer test)

- Relationship between moisture and drying shrinkage (vibrating wire gauge at [1 inch] below surface and demac gauge on the surface)

WEATHER CONDITIONS

Ambient temperature, ambient relative humidity, wind speed, and solar radiation data were recorded at hourly intervals on a continuous basis through a weather station. Over the 3 days after placement of concrete, ambient temperatures ranged from a low of almost 71 °F in the morning hours and to a high of 119 °F in the afternoon as shown in Figure C-1 (a). A daily temperature fluctuation (morning to afternoon) of about 48 °F (from 71 to 119 °F) was noticed on the 21st and 22nd of July, whereas a slightly lower temperature fluctuation of 39 °F (from 77 to 116 °F) was noticed on July 20th. Ambient

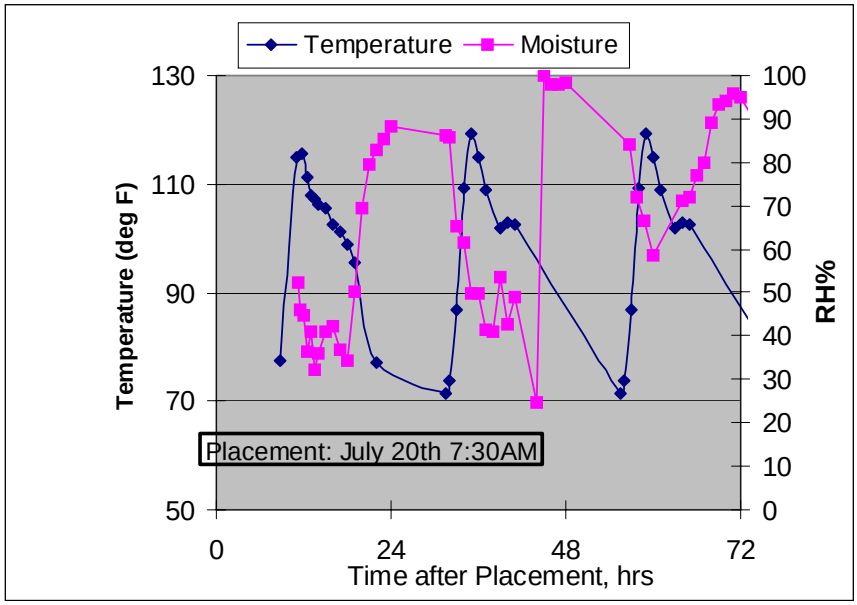

(a)

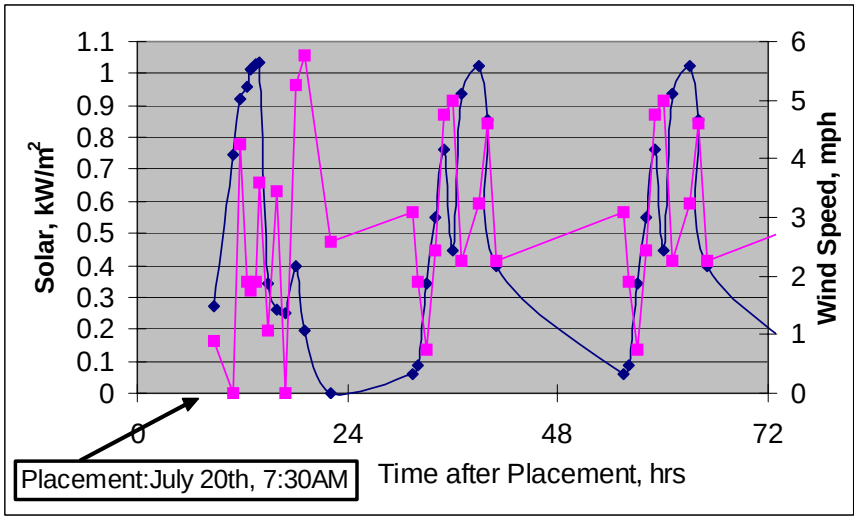

(b)

Figure C-1 Weather Conditions at Cleveland, US 59: (a) Ambient Temperature and Relative Humidity; (b) Wind Speed and Solar Radiation.

relative humidity ranged from as low as 25 percent in the afternoon to as high as 98 percent in the morning over the same period as shown in Figure C-1 (a). The lowest relative humidity of 32.4, 25, and 58.7 percent were recorded in the afternoon of July 20th, 21st, and 22nd, respectively. There was rainfall in the afternoon of both the 21st and 22nd that caused low relative humidity fluctuation (100 to 58.7 to 96) from the 21st evening to the 22nd afternoon.

As shown in Figure C-1 (b), 1.033 kW/m^2 of maximum solar radiation and 5.76 mph (2.6 m) of wind speed were recorded over the period. Maximum solar radiation was recorded between 12:00 and 1:00 pm daily. In general, the wind speed was low throughout the data collection period of 3 days. Maximum solar radiation during the afternoon coincided with relatively higher wind speed (5 to 6 mph) in general.

TEMPERATURE AND MOISTURE OF PAVEMENT

Temperature and relative humidity data at 1.9, 7.6, and 17.8 cm (0.75, 3, and 7 inch) depth were recorded by using chilled mirror dew point and dry bulb temperature sensors. The instrumentation of these sensors was similar to the instrumentation described in Appendix A for Van Horn.

- High placement temperature due to high ambient temperature along with high heat of hydration (faster hydration reaction due to high temperature) had caused high temperature rise until the afternoon of July 20th (Figure C-2 (a)). It seems that high fly ash replacement (more than 30 percent) is necessary in order to reduce this high temperature rise. It is interesting to recall that in Van Horn, the temperatures at three depths showed a decreasing trend until the next morning due to low heat evolution caused by a higher amount of slag replacement (50 percent).
- Concrete temperatures at 7.6 and 17.8 cm (3 and 7 inch) were always higher than both concrete temperature at 2.54 cm (1 inch) depth and ambient temperature (Figure C-2 (a)). The temperature measured at 7.6 and 17.8 cm (3 and 7 inch) had almost the same values during the period of data collection except the night of the 21st and the morning of the 22nd when the temperature at the 3 inch position was lower than the temperature at the 17.8 cm (7 inch) position. Higher concrete temperature at 2.54 cm (1 inch) depth than ambient temperature was valid during

night to morning time whereas during afternoon time concrete at 2.54 cm (1 inch) reached a temperature similar to ambient temperature. Therefore, concrete temperature at 2.54 cm (1 inch) was more affected by the ambient temperature condition than that at 7.6 and 17.8 cm (3 and 7 inch) depth.

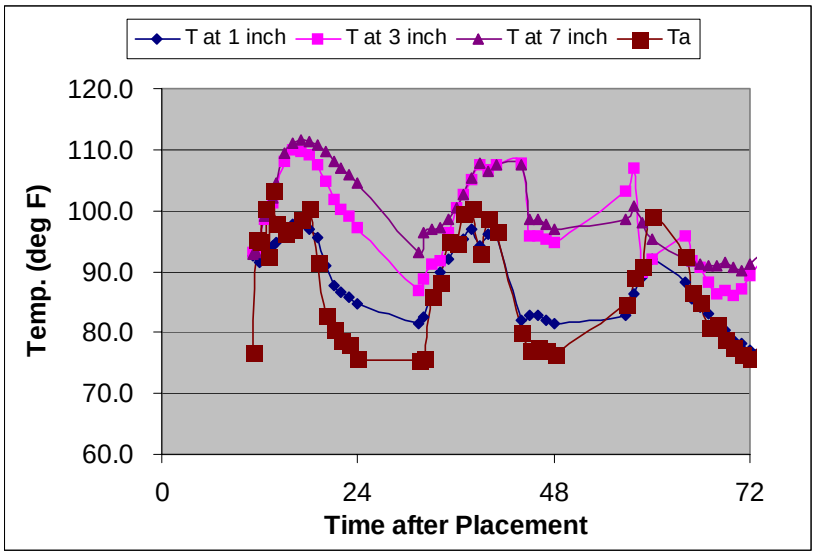

(a)

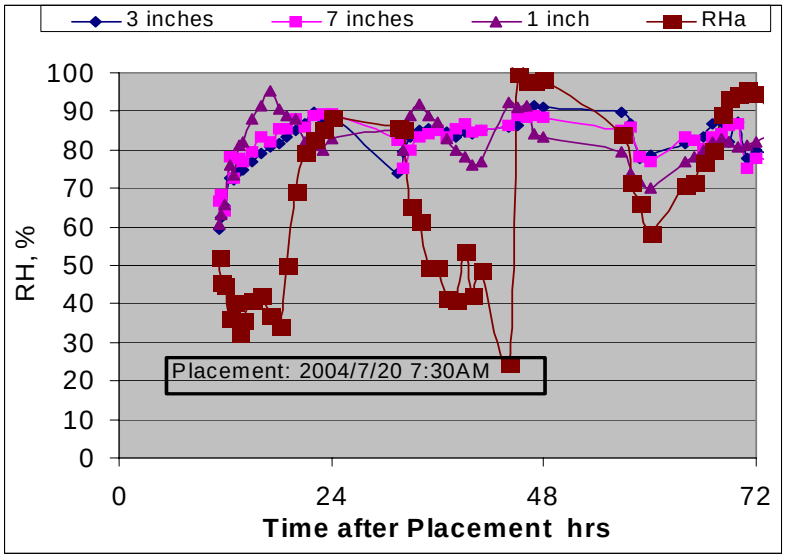

(b)

Figure C-2 Temperature and Relative Humidity at Different Depths of Pavement, Cleveland: (a) Temperature; (b) Relative Humidity.

- Considerable temperature fluctuation at all depths until 52 to 54 hours was common and showed a similar trend with the ambient temperature variation. This fluctuation indicates that ambient temperature can influence the temperature signature of concrete at a relatively deeper level (until 17.8 cm [7 inch]) if the placement temperature is high due to high ambient temperature.

Following are the observations on concrete relative humidity at different depths in conjunction with ambient relative humidity:

- Concrete relative humidity steadily increased until the night (9-10 pm) of the placement day at 7.6 and 17.8 cm (3 and 7 inch) depth. Relative humidity at 2.54 cm (1 inch) showed an overall increasing trend with more fluctuation (Figure C-2 (b)).
- Daily variation of relative humidity at 2.54 cm (1 inch) was higher than that at 7.6 and 17.8 cm (3 and 7 inch) depth.
- The higher relative humidity at the deeper level is clearly manifested after 42 hours of concrete placement.
- Increasing trend of relative humidity at 2.54 cm (1 inch) coincided with a decreasing trend of ambient relative humidity periodically until around 36 hours. This moisture behavior at 2.54 cm (1 inch) is due to a combination of high evaporation and bleeding due to high ambient temperature and relative humidity fluctuation. After around 36 hours, the trend of relative humidity at 2.54 cm (1 inch) was similar to the trend of ambient relative humidity. Therefore, concrete relative humidity measured at 2.54 cm (1 inch) below the surface was more affected by ambient relative humidity as observed in concrete temperature trends.

CURING CONDITION AND EVAPORATION

ATEK curing monitoring system was installed by following the procedure described in Appendix A for the Van Horn test section. Temperature and relative humidity data at 1.9 cm (0.75 inch) depth, surface, and ambient were recorded at hourly intervals on a continuous basis. Following are the important observations on curing:

- The similar trend of variation of surface relative humidity and ambient relative humidity suggests pronounced influence of ambient relative humidity on surface relative humidity as compared to the concrete relative humidity at 1.9 cm (0.75 inch) (Figure C-3).
- Relative humidity of both surface and inside concrete increased due to bleeding until the next day of construction as shown in Figure C-3. However, beginning the

next morning they decreased due to the reduced rate of evaporation and moisture diffusion as described previously.

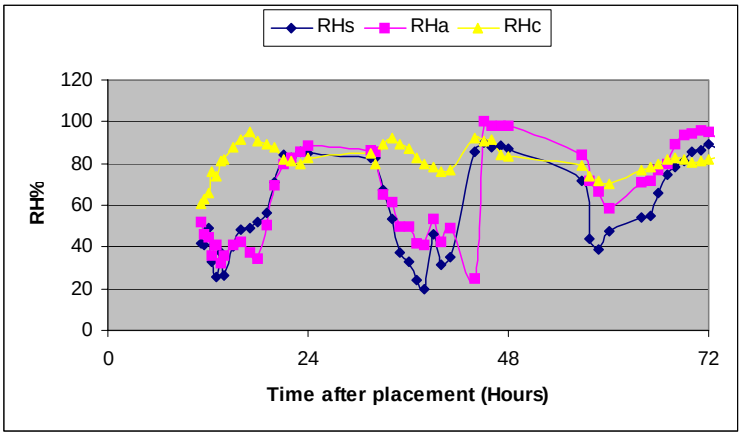

Figure C-3 Relative Humidity of Ambient, Surface, and Inside Concrete at 0.75 Inch Below.

- Increasing trend of relative humidity at 2.54 cm (1 inch) coincided with a decreasing trend of ambient relative humidity periodically until around 36 hours. This moisture behavior at 2.54 cm (1 inch) is due to a combination of high evaporation and bleeding due to high ambient temperature and relative humidity fluctuation.
- Overall relative humidity variation at 1.9 cm (0.75 inch) is similar to 1.9 (0.75 inch) relative humidity at Baytown but considerably lower than 1.9 cm (0.75 inch) at Van Horn.

INITIAL AND FINAL SETTINGS OF PAVEMENT

The initial and final setting times were measured using the ASTM C 403 test method. The instrumentation and test procedure was followed the way it is described in Appendix A for the Van Horn test section. Initial and final settings were determined from a plot of penetration resistance versus elapsed time, which were approximately 4.64 and 6.07 hours after placement of concrete in the pavement. The maturities of 237 and 303 °C-hours were correlated with 3.5 MPa (initial setting resistance of 500 psi) and 27.6 MPa (final setting resistance of 4000 psi) of penetration resistances, respectively, as shown in Figure C-4.

DRYING SHRINKAGE

Free drying shrinkage strain as a function of time was measured by vibrating wire gauge (VWG). Two shrinkage bars according to ASTM 157 were cast. One VWG was placed at the surface of one bar and another VWG was placed at 2.54 cm (1-inch) below the surface in another bar in order to measure free shrinkage at the surface and at 2.54 cm (1 inch) below the surface. The results are presented in Figure C-5. A perusal of Figure C-5 shows that shrinkage strain of the surface was higher than that at 2.54 cm (1 inch) depth.

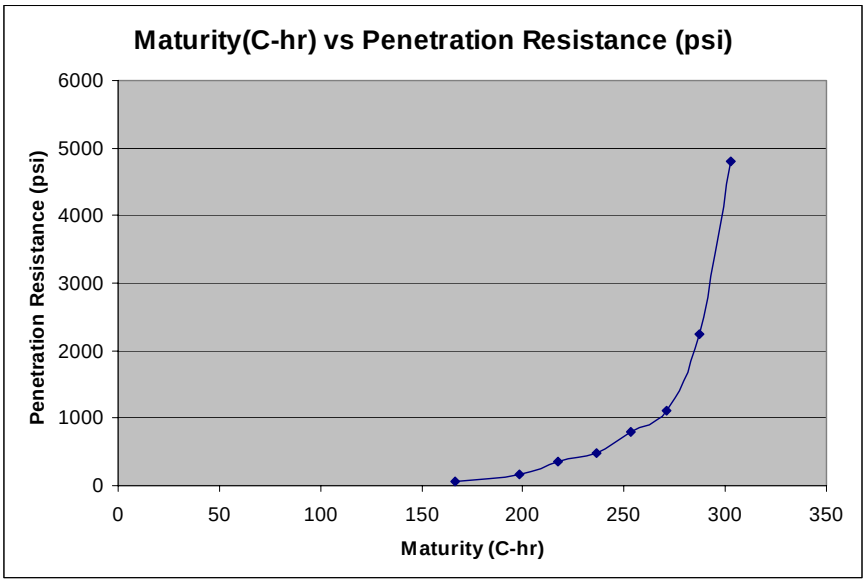

Figure C-4 Maturities at Initial and Final Settings.

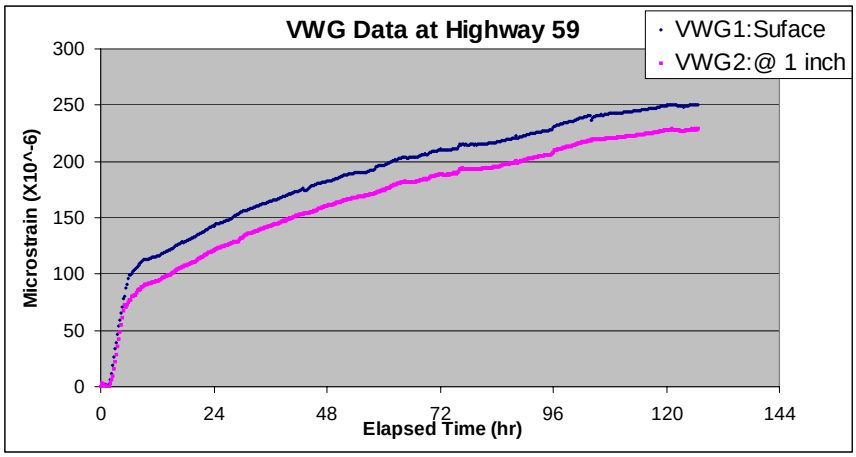

Figure C-5 Vibrating Wire Gauge Free Shrinkage at 1.54 cm (1 Inch) Depth and on the Surface of the ASTM 157 Bar as a Function of Time after Placement.

MOISTURE-BASED MATURITY

Existing maturity concepts were modified by including a moisture parameter in the maturity model (see details in Appendix A), and moisture-based maturity was calculated using this modified model. Both conventional and moisture-based maturity at 1.9 cm (0.75 inch) depth are compared and

presented in Figure C-6. A perusal of Figure C-6 shows that moisture-based maturity is always lower than conventional temperature-based maturity at all ages until 72 hours. The rate of increase of moisture-modified maturity changes with time after placement depending on moisture situation at 1.9 cm (0.75 inch). Therefore, moisture-based maturity is sensitive to reflect any loss of maturity due to loss of moisture in the top part of the concrete.

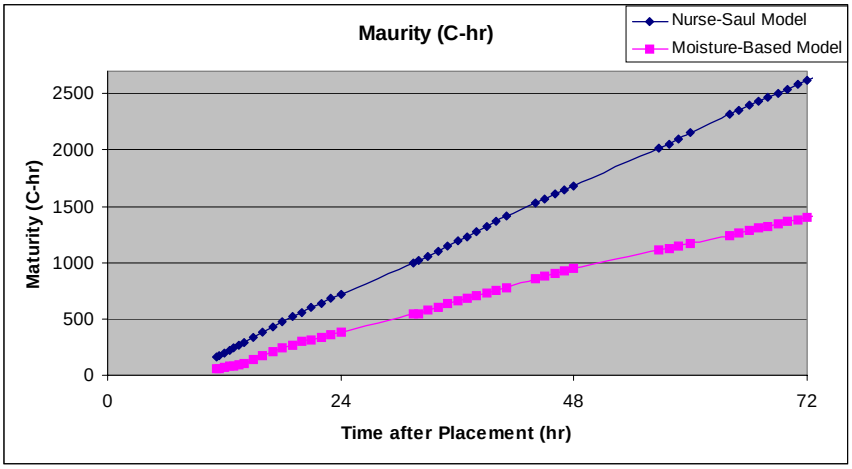

Figure C-6 Moisture-Based Maturity versus Conventional Time-Temperature Maturity as a Function of Curing Time.

CONCLUSIONS

Effects of environmental parameters on the performance of continuously reinforced concrete pavement were studied by field measurement at Cleveland, US 59. The following conclusions can be drawn from the test results:

- The daily variation of temperature and relative humidity was high. The absolute solar radiation was high but wind speed was low.
- Concrete temperatures at 7.6 and 17.8 cm (3 and 7 inches) below surface were higher than both concrete temperature at 1 inch below and ambient temperature for the period of 72 hours. Concrete temperature at 1 inch below was most affected by the ambient temperature than that at 7.6 and 17.8 cm (3 and 7 inch) below. However, influence of ambient temperature on the temperature of concrete at a relatively deeper level was observed because of high ambient temperature during placement.
- Concrete relative humidity measured at 1.9 cm (0.75 inch) below surface was more affected by ambient relative humidity as observed in concrete temperature trends.
- Overall variation of relative humidity at 1.9 cm (0.75 inch is similar to 1.9 cm (0.75 inch) relative humidity at Baytown but considerably lower than 1.9 cm (0.75 inch) relative humidity at Van Horn.

- Initial and final set times of the pavement were found 4.64 and 6.07 hours after placement of concrete in the pavement using penetration resistance test.

APPENDIX D

AGGREGATE GRADATION EFFECTS ON BOND STRENGTH

INTRODUCTION

Gap-graded aggregates have a lower dry rodded unit weight (DRUW) and larger total volume of voids to be filled with cement mortar than concrete with dense-graded aggregates. Because of the higher mortar content (cement + water + sand) in the mixture, the concrete with gap-graded aggregates may undergo larger volumetric strain due to shrinkage. On the other hand, dense-graded aggregates have larger DRUW and more extensive surface area to make contact with the mortar. Accordingly, strength of dense-graded concrete should exceed the strength of gap-graded concrete. In this context, this appendix reports preliminary results of measured effects of the aggregate gradation on the cracking-related performance of pavement concrete.

THE GERMAN CRACKING FRAME

A procedure to monitor gradation effects on the cracking-related strength and strain over time relative to shrinkage strain was conducted in the laboratory using the German cracking frame. The cracking frame (Figure D-1) accommodates a 1 m (3.28 ft) long concrete specimen. The ends of the specimen are configured by dovetails in two steel crossheads. These crossheads are connected with two steel bars to restrain longitudinal change in the distance between the crossheads. Small longitudinal deformations or strains in the steel bars are calibrated to load in order to determine the longitudinal stress applied to the frame (Figure D-2). The concrete

Figure D-1 Cracking Frame.

specimen cross section at the center portion is 12.8 × 14.6 cm (5.05 × 5.75 inch) and at the ends of the dovetails is 12.0 × 32.9 (5.05 × 12.95 inch). It is anticipated that the cracking sensitivity of concrete can be examined within a limited geometric range by comparing test results between different concrete mixtures using the cracking frame. The cracking frame has the added advantage of providing a sufficiently large test specimen to allow for a crack inducer and instrumentation to be inserted in the concrete. The use of the crack inducer ensures that the crack will indeed be controlled in the center in the specimen.

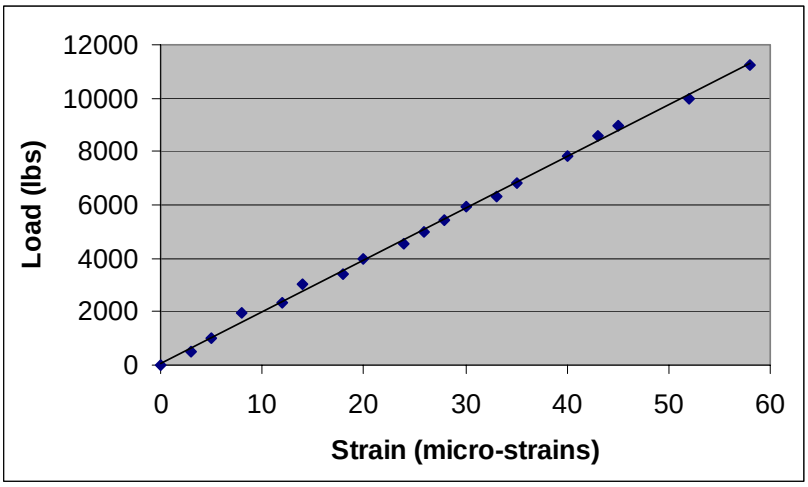

Figure D-2 Cracking Frame Force versus Load Cell Strain.

Laboratory Test Program

Cracking-related displacements with respect to shrinkage and creep strains were compared by using gap-graded and dense-graded aggregates in concrete mixtures as shown in Table D-1. The concrete mixture consisted of crushed limestone as the coarse aggregate,

Table D-1 Mixture Proportions in 1 m^3 (35.3 ft^3) of Cracking Frame Concrete.

Materials	Proportions	
	Gap-Gradation	**Dense-Gradation**
Cement	251 kg (533 lb)	251 kg (533 lb)
Fly Ash	84 kg (184 lb)	84 kg (184 lb)
Coarse Aggregate	1102 kg (2,428 lb)	708 kg (1,561 lb)
Intermediate Aggregate	-	424 kg (935 lb)
Fine Aggregate	530 kg (1,168 lb)	514 kg (1,132 lb)
Water	216 kg (476 lb)	216 kg (476 lb)
Air-Entraining Admixture	236 ml (8.1 oz)	236 ml (8.1 oz)
w/c Ratio	0.42	0.42
CAF	0.70	0.45
IAF	-	0.25
CF	6.0	6.0
Concrete Unit Weight	2183 kg/m^3 (136 lb/ft^3)	2197 kg/m^3 (137 lb/ft^3)

pea gravel as intermediate aggregate, and sand as the fine aggregate. The coarse aggregate factor (CAF) and intermediate aggregate factor (IAF), the main parameters in this project, were 0.70 and zero, and 0.45 and 0.25, respectively, while they had the same cement factor (CF) of 6.0. A water-cement ratio of 0.42 was used and the unit weights for gap-gradation and dense-gradation concrete were found to be 2183 kg/m^3 (136 lb/ft^3) and 2197 kg/m^3 (137 lb/ft^3), respectively.

The cracking frame was instrumented to collect the following data during the hardening process:

- free shrinkage strain (ASTM C-157),
- strain of steel rods,
- concrete strain in the cracking frame,
- concrete temperature (top and bottom),
- concrete compressive strength (1, 3, and 7 days),
- concrete split tensile strength (Modified ASTM C 496),
- concrete slump (ASTM C 143), and
- number of drops (a German DIN 1048 test standard).

Demac points were installed on the top surface of ASTM C 157 specimens. The specimens were subjected to one-dimensional drying to be representative of the drying shrinkage the frame concrete is subjected to. The cracking frame strain resulted from restraint of the free shrinkage strain and was measured by the load cells installed on the steel frame separating the bulkheads. Concrete strain was measured by vibrating wire strain gauges embedded into the cracking frame concrete. Two thermocouples were also embedded to measure the concrete temperature at 2.54 cm (1 inch) from the top and bottom surfaces. Concrete compressive strength ($f_c^{'}$) was measured by 15.2 × 30.5 cm (4 × 8 inch) standard cylinder specimens to monitor strength gain over time and to provide a basis for determining the degree of hydration and the modulus of elasticity. Concrete split tensile strength was also measured following the modified ASTM C 496 procedure. Workability of concrete was measured by the slump test and characterized by the German DIN 1048 drop test method.

Concrete Workability

Slump test and drop test were conducted immediately upon mixing the concrete. The drop test (DIN 1048) is a German test standard that perhaps measures to some extent the mobility of concrete mixture with a slump less than 50 mm (2 inch) to serve as an indicator of whether workability is sufficient during placement of the concrete. The test is a simple measure of the number of drops taken to cause a concrete mixture in a slump cone to bulge laterally outward to a given diameter in a consistent and flowable manner. The measured slump and number of drops for each mixture are shown in Table D-2. The number of drops of the concrete mixed with dense-graded aggregates is greater than that of open-graded aggregates although they had the same slump. The concrete mixed with dense-graded aggregates showed greater resistance to lateral movements. Apparently, the higher adhesion between aggregates and cement mortar of dense-gradation concrete hindered the concrete from bulging laterally outward.

Table D-2 Slump and Drop Test Results.

	Gap-Gradation	**Dense-Gradation**
Slump	40 mm (1.6 inch)	40 mm (1.6 inch)
Drop	6 Drops	12 Drops

SHRINKAGE AND CREEP STRAINS

During the cracking test, the concrete free shrinkage (ASTM C157) was monitored with time (Figure D-3) along with the strain in the concrete and the steel frame. These trends are shown in Figures D-4 and D-5, respectively. The strain measured by the concrete gauge represents the net effect of shrinkage and elastic strain due to the restraint imposed by the cracking frame, and if the strain in the steel frame was zero, the strain measured by this gauge would represent

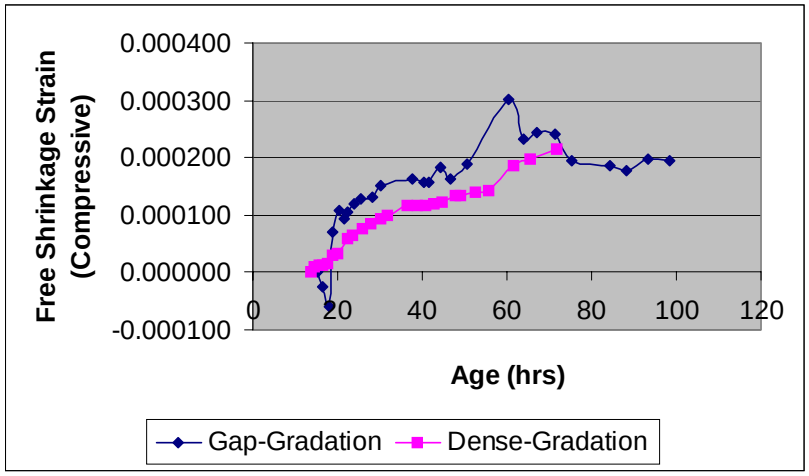

Figure D-3 Free Shrinkage Strain.

the creep strain in the concrete. Otherwise, the difference between the strain measured by the gauge in the concrete and strain measured by the gauge on the steel represents the creep strain in the concrete. It is noted that the initial portion of the strain shown in Figure D-4 should not exceed the amount of free shrinkage measured from the ASTM C 157 specimen, but since it was we consequently ignored this portion in the creep strain calculation shown in Figures D-6 and D-7.

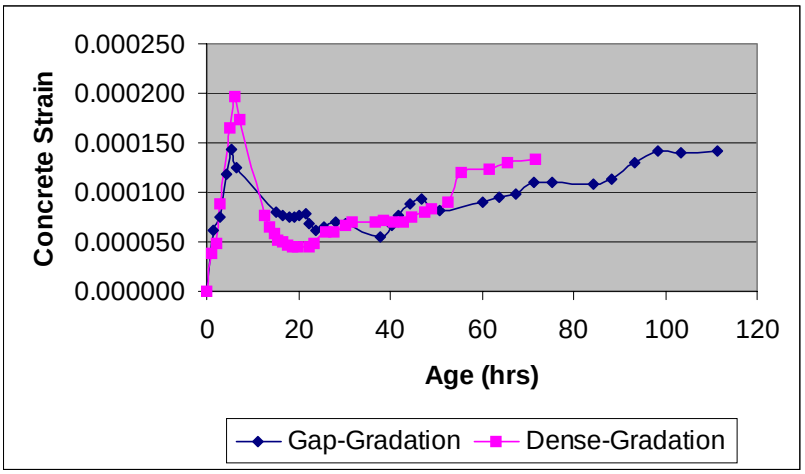

Figure D-4 Concrete Strain.

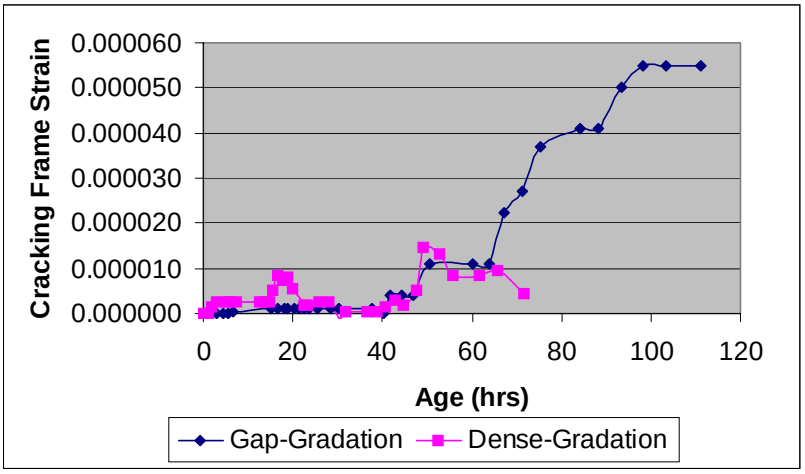

Figure D-5 Cracking Frame Strain.

As previously noted, the cracking frame strain (Figure D-5) was measured in the laboratory during the testing sequence, but the load on the concrete (F_s) due to the drying shrinkage was determined using a calibration curve (Figure D-2) developed from the load cell reading correlated to the strain gauge readings. Shrinkage strain (Figure D-3) was found from ASTM C 157 specimen data as was previously described. The shrinkage strain and the frame strain varied with time, as did the force in concrete. The frame strain was nearly zero until around 40 hours of concrete age. So, a significant amount of creep strain took place over 40 hours.

Analysis of the restraint provided in the cracking frame suggests that the creep strain can be found from the following relation:

$$\varepsilon_{crp} = \varepsilon_v - \varepsilon_e - \left(\frac{F_s}{E_c A_c}\right) = \varepsilon_{conc} - \varepsilon_e \qquad \text{(A-1)}$$

where

ε_{crp} = creep strain
ε_v = shrinkage strain (ASTM C 157)
ε_e = frame strain
F_s = force in concrete (F)
E_c = modulus of elasticity of concrete (F/L^{-2})
A_c = specimen cross-sectional area (L^2)

The accumulative creep curves determined by equation (A-1) are shown in Figure D-6. The total creep strain of concrete mixed with gap-graded aggregates appears to be larger than the dense-gradation concrete. The accumulative creep curves determined by the net difference between concrete strain and cracking frame strain with time are shown in Figure D-7.

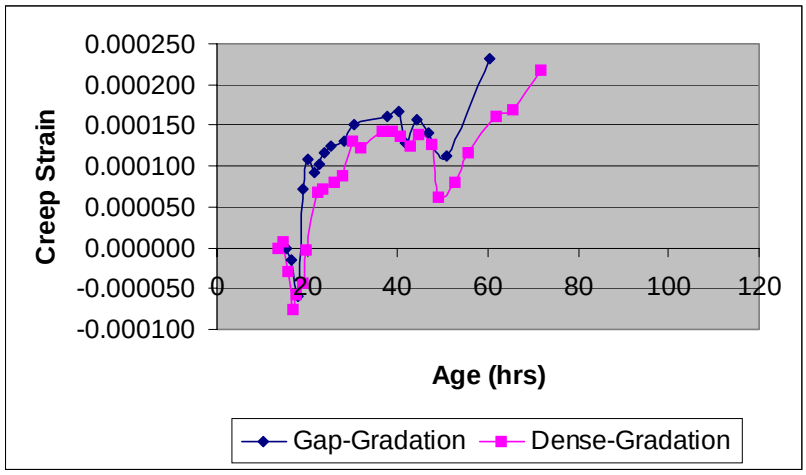

Figure D-6 Creep Strain Calculated by Equation (A-1).

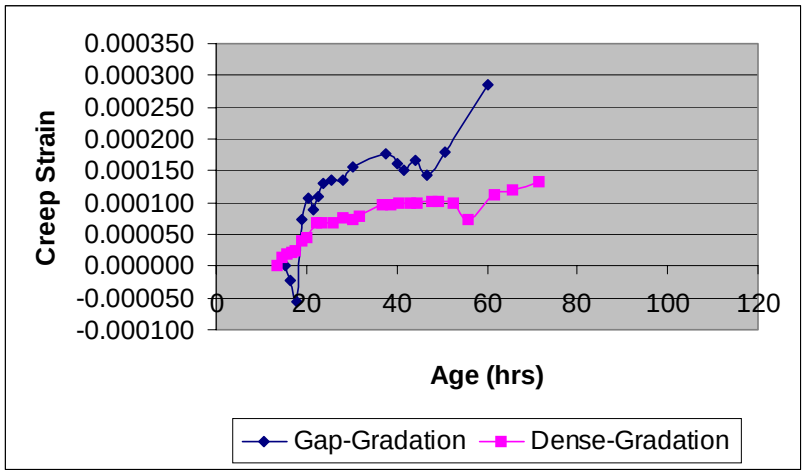

Figure D-7 Net Difference between Concrete Strain and Cracking Frame Strain.

Cracking at the Notch

The time of crack formation in the

cracking frame concrete mixed with gap-graded aggregates was not accurately observed while the crack formed in the dense-gradation concrete at 69 hours. The time of cracking was estimated between 55 and 65 hours. The cracks run through the full depth of the test specimen. The laboratory strength gain with time for both gradations can be seen from Figure D-8.

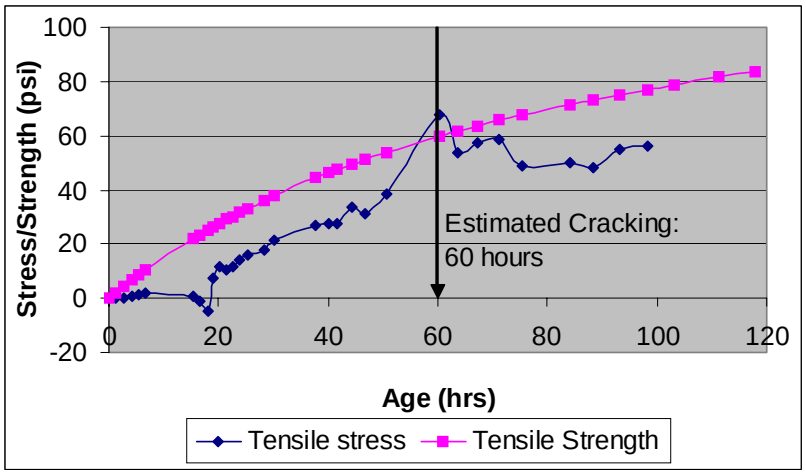

(a) Gap-Gradation

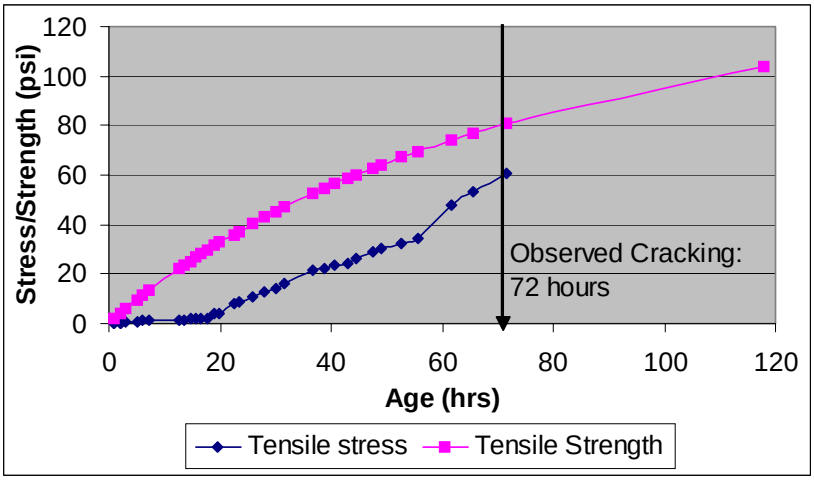

(b) Dense-Gradation

Figure D-8 Stress and Strength Development.

To determine the strength development of the concrete over time, compressive strength tests were conducted at an age of 1, 3, and 7 days. Using specially prepared fracture specimens following a modified ASTM C 496 procedure, the fracture parameters (K_{If} and c_f) of the concrete were found and used to determine the cracking strength over time based on the use of fracture mechanics. The tensile strength (f_t) at the tip of the notch was determined using equation:

$$f_t = \frac{K_{If} c_n}{\sqrt{g'(\alpha) c_f + g(\alpha) h}} \qquad \text{(A-2)}$$

where

$g'(\alpha)$ and $g(\alpha)$ are slab geometry factors

K_{If} = stress intensity factor ($F/L^{-2}\ L^{-1/2}$)
c_f = process zone length (L)
c_n = arbitrarily defined constant
h = slab thickness (L)

Tensile stress of the concrete was calculated based on the restraint of shrinkage and thermal strains. Compared to gap-gradation concrete, higher tensile strength and lower tensile stress were developed in the concrete specimen mixed with dense-graded aggregates as shown in Figure D-8. The estimated time of cracking of gap-gradation concrete coincides with the calculated cracking time as shown in Figure D-8 (a). However, the calculated tensile stress of dense-gradation concrete did not exceed the concrete strength at the time of the observed cracking. The results shown in this report indicate the shrinkage measurement methodology needs to be improved because of the differences in the readings between the demac and the vibrating wire gauges previously noted.

CONCLUSIONS

Cracking-related displacements of concrete with respect to aggregate gradation effects are under investigation in the laboratory using the German cracking frame. The concrete mixed with gap-grade aggregates had 0.7 of CAF, while the concrete with dense-graded aggregate had 0.45 of CAF and 0.25 of IAF. The gap-graded concrete has indicated larger shrinkage and creep strains than dense-gradation concrete perhaps because of its higher volume content of cement mortars in the mixture. Because of the larger shrinkage strain, higher restraint tensile stress was developed in the gap-gradation concrete. Lower level of tensile strength of gap-gradation concrete was developed due to its higher cement content and more extensive surface area of aggregates to be contacted to the mortar. As a result, crack was formed in the concrete mixed with gap-graded aggregates earlier than the concrete mixed with dense-graded aggregates.

APPENDIX E
ITEM 360 SPECIAL PROVISION

360.11. Curing.
(1) General. All concrete pavement shall be *monitored for curing quality* for a period of not less than *24* hours from the beginning of curing operations. All exposed surfaces, including vertical surfaces of the placed concrete, shall be cured immediately after finishing operations have been completed, in accordance with the requirements specified herein. *The effectiveness of the concrete curing shall be determined according to Tex Test Method "ccc" and meet the following minimum effective thicknesses over the monitoring period when the ambient relative humidity is less than 80%*:

Wind Speed	**1 Day Coarse Aggregate Fracture Toughness ($psi \cdot \sqrt{in}$)**		
	<350	**>350 but <700**	**>700**
<10 mph	2.0 in	1.5 in	1.0 in
>10 mph	2.5 in	2.0 in	1.5 in

Monitoring will be conducted at 500 foot or 1500 sy intervals of paving.

(2) Membrane Curing. After final finishing and immediately after the free surface moisture has disappeared, the concrete surface shall be sprayed uniformly with a curing compound in accordance with Article 526.5. If the *effectiveness* of the membrane *falls below the prescribed value listed above or if the evaporation rate exceeds 2.0 kg/m^2/hr* before the expiration of *24* hours after original application, then additional *applications of the* compound *shall be applied to improve the effectiveness of the curing*.

Special care shall be taken to insure that the sides of the tining grooves are coated with the curing compound.